NASA Technical Paper 2594

October 1986

Steady and Unsteady Transonic Pressure Measurements on a Clipped Delta Wing for Pitching and Control-Surface Oscillations

Robert W. Hess,
F. W. Cazier, Jr.,
and Eleanor C. Wynne

NASA

NASA Technical Paper 2594

1986

Steady and Unsteady Transonic Pressure Measurements on a Clipped Delta Wing for Pitching and Control-Surface Oscillations

Robert W. Hess,
F. W. Cazier, Jr.,
and Eleanor C. Wynne

Langley Research Center
Hampton, Virginia

National Aeronautics
and Space Administration

Scientific and Technical Information Branch

Summary

Steady and unsteady pressures were measured on a clipped delta wing with a 6-percent circular-arc airfoil section in the Langley Transonic Dynamics Tunnel. The model was oscillated in pitch about 65.2 percent of the root chord and had an oscillating trailing-edge control surface. Measurements were concentrated over a Mach number range from 0.88 to 0.94; less extensive measurements were made at Mach numbers of 0.40, 0.96, and 1.12. The Reynolds number based on mean chord was approximately 10×10^6. Static-pressure distributions were obtained for ranges of Mach number, wing pitch angle, and control-surface deflection. Unsteady pressures were measured as functions of Mach number, mean angle of attack, pitch amplitude and frequency, and control-surface amplitude and frequency.

Introduction

In the past, the primary tools in the study of aeroelastic instabilities at transonic speeds have been experimental methods. Developing computer technology and computer codes are gradually making meaningful analysis possible in this complex mixed-flow speed range. Concurrent with analytical advances, a data base of unsteady pressure measurements (e.g., refs. 1 through 6) has been growing and will provide a source for comparison with the new codes.

This paper gives results of steady and unsteady pressure measurements made on a clipped-tip delta wing (fig. 1), primarily in the transonic speed range, at a Reynolds number based on mean chord of approximately 10×10^6 in the Langley Transonic Dynamics Tunnel (TDT). The test was conducted using a Freon[1] test medium and focused on the transonic speed range between Mach numbers of 0.88 and 0.94. Less complete measurements were also made at Mach numbers of 0.40, 0.96, and 1.12. The measurements were made for the wing oscillating in pitch at $\pm 0.25°$ and at $\pm 0.50°$ about mean angles of attack ranging from 0° to 3° and for control-surface oscillations ($\pm 2°$, $\pm 4°$, and $\pm 6°$) about a control-surface mean angle of attack of 0° over a range of wing pitch angles. Static and dynamic data are presented in the form of cross plots of the variables. The static pressure distributions are given in the form of $C_{p,u}$, the coefficient of the upper-surface pressure, and ΔC_p, the coefficient of the pressure difference between the upper and lower surfaces. The dynamic data are given in the form of the pressure coefficient modulus normalized by motion amplitude (deg) and phase for both $|C_{p,u}|$ and $|\Delta C_p|$. Pressure modulus coefficients were chosen instead of real and imaginary coefficients, because the dynamic-pressure distributions are closely related to the static-pressure distributions, and meaningful comparisons can be made between the two. Because of the bulk of the data, only the test conditions for each data point are listed. The tabulated data are available in the microfiche enclosed with this paper and on magnetic tape upon request.

Steady pressure distributions are compared with computed pressure distributions obtained from a small disturbance code (ref. 7) and with the linear code of reference 8. Comparisons of unsteady pressure distributions are also made with reference 8.

The appendix is a discussion of vortex formation, development, and influence shown by the pressure distributions. An analysis using the SOUSSA (ref. 9) surface panel method is compared with the experimental data in the angle-of-attack range, where the vortex effects are small.

The authors wish to acknowledge the contribution of Herbert J. Cunningham of the Unsteady Aerodynamics Branch for the linear-theory calculations that were used in comparison with experiment in this report.

Symbols

A_c	control-surface area, in^2
a_n	Fourier coefficient
b_n	Fourier coefficient
C_h	static control-surface hinge-moment coefficient, $\frac{\text{hinge moment}}{qA_c\bar{c}}$, positive for trailing edge down
C_p	pressure coefficient
$C_{p,\ell}$	lower-surface steady pressure coefficient (CPL in table V and in computer-generated supplements)
$C_{p,u}$	upper-surface steady pressure coefficient (CPU in table V and in computer-generated supplements)
$\|C_p\|$	modulus of oscillating-pressure coefficient
$\|C_{p,\ell}\|$	modulus of oscillating pressure on lower surface
$\|C_{p,u}\|$	modulus of oscillating pressure on upper surface

[1] Freon: Registered trademark of E. I. du Pont de Nemours & Co., Inc.

ΔC_p pressure differential coefficient (DEL CP in table V and in computer-generated supplements), $\frac{p_l - p_u}{q}$

$|\Delta C_p|$ modulus of oscillating-pressure coefficient differential, $\frac{|p_l - p_u|}{q}$

c local chord length in streamwise direction, in.

c wing mean chord length, in.

c_c control-surface mean chord length, in.

Exp. experiment

f frequency (FREQ. in table V and in computer-generated supplements), Hz

H.L. hinge line

k reduced frequency (K in table V and in computer-generated supplements), $\frac{\bar{c}\omega}{2V}$

L.E. leading edge

M Mach number (MACH in table V and in computer-generated supplements)

N number of samples in integer number of cycles

n multiple of oscillating frequency

PSD power spectral density

p_l pressure at lower-surface orifice, psf

p_t stagnation pressure (H in table V and in computer-generated supplements), psf

p_u pressure at upper-surface orifice, psf

q dynamic pressure (Q in table V and in computer-generated supplements), psf

R Reynolds number based on mean chord length (RN in table V and in computer-generated supplements)

r radius, in.

S span, in.

T_o stagnation temperature (TO in table V and in computer-generated supplements), °R

t/c thickness ratio

V free-stream velocity, ft/sec

x streamwise coordinate measured from local leading edge, in.

x/c local chordwise position referenced to local chord length

y spanwise coordinate, in.

α dynamic peak amplitude in pitch, positive for trailing edge down (ALPHA in table V and in computer-generated supplements), deg

$\bar{\alpha}$ steady or mean dynamic amplitude in pitch, positive for trailing edge down (ALPHA BAR in table V and in computer-generated supplements), deg

δ dynamic control-surface peak amplitude, positive for trailing edge down (DELTA in table V and in computer-generated supplements), deg

$\bar{\delta}$ steady or mean control-surface deflection, positive for trailing edge down, deg

ϕ phase angle between oscillatory pressure and oscillating wing pitch angle or control-surface position, deg

$\Delta\phi$ phase angle between upper and lower surface (D PHAS in table V and in computer-generated supplements), deg

ϕ_ℓ lower-surface phase angle (PHAS L in table V and in computer-generated supplements), deg

ϕ_u upper-surface phase angle (PHAS U in table V and in computer-generated supplements), deg

ω frequency, rad/sec

Model and Apparatus

Model

The model planform geometry is shown in figure 1. The model had a leading-edge sweep angle of 50.4°, a span of 45.08 in., a root chord of

63.55 in., a tip chord of 9.03 in., and a 6-percent-thick circular-arc airfoil section. The model was constructed of stainless-steel ribs and spars (fig. 2) covered by Du Pont Kevlar epoxy panels. Wing stiffness was not measured, but the structure was extremely stiff, as indicated in the section "Pitch-Oscillation Node Lines." An integral shaft at 65.22-percent root chord connected the wing to the driving mechanism. A fence was built-in at the root (fig. 3(a)) to seal the wing-splitter plate juncture. Leading- and trailing-edge control surfaces were located between 56.6-percent span and 82.9-percent span. The hinge line of the leading-edge control was at 15-percent chord, and the hinge line of the trailing-edge control was at 80-percent chord. The control-surface spars, ribs, and skin were made of graphite-epoxy and had stepped steel shafts which were pinned to hydraulic actuators. The hinge line was sealed on both control surfaces. The leading-edge control surface was pinned and faired along the streamwise edges and was not utilized for the tests described in this report. The hinge-line cove was not faired.

There was a misalignment of the trailing-edge control surface on the order of 2°, so the inboard trailing edge was lower than the outboard trailing edge. For these tests, the control surface was positioned to give equal deflection, positive and negative, on each edge.

A boundary-layer transition strip with a width of 0.1 in. was applied to both the upper and lower wing surfaces at 8-percent chord. Number 70 grit was used from root to midspan, and number 90 grit was used from midspan to tip.

Figure 3(a) shows the wing mounted on the sidewall of the TDT. The supporting shaft projects through a bearing plate to the oscillating drive mechanism mounted on the sidewall inside the tunnel plenum. The splitter plate was constructed in two sections. The outer section was made of aluminum-sheathed aircraft plywood and was supported by 5-in. supports to bring the splitter plate outside the tunnel-wall boundary layer. The inner (center) section was fabricated from 0.125-in. sheet aluminum and served as a movable, compliant seal between the splitter plate and the wing fence. This section, with a slot to accommodate the wing, was remotely controlled in pitch to adjust the angle of the slot as the wing mean angle was changed. A Teflon[2] strip on the outer edge of the slot served as a bearing surface and seal between the splitter plate and the wing fence.

[2] Teflon: Registered trademark of E. I. du Pont de Nemours & Co., Inc.

Oscillating Mechanisms

Wing pitch. The model was designed to operate as a spring-mass system at resonance in pitch and roll using separate spring systems. The spring systems were driven by a hydraulic actuator (2700 psi; 1-in^2 bore) that was controlled by a servo feedback system for each mode. For the present test, the roll system was removed. The pitch springs (fig. 3(b)) had a combined stiffness of 667 lb per degree and were attached to arms on each side of the shaft by a system of cables and pulleys. The model was driven in pitch by the hydraulic actuator, which was coupled by an arm to the wing shaft by a rod-end bearing. The mean angle of attack was independent of the oscillating system and was driven through a worm gear by a direct-current motor. In practice, it was necessary to operate the system in a preloaded condition of $-1°$ to eliminate load reversal. The preloading eliminated the development of free play in the bearings of the system.

Control surface. The rotary vanes of the miniaturized hydraulic control-surface actuators were pinned to the control-surface shaft adjacent to and inboard of the control surfaces. These actuators were similar to those described in reference 10.

Pitch-Oscillation Node Lines

The wind-off node lines for forced oscillations in pitch were determined by using the model pitch-oscillation system and accelerometers. Node lines were determined for test frequencies of 4 Hz, 8 Hz, 16 Hz, and 22 Hz. The first natural frequency was 28 Hz. The deflections were measured with six accelerometers evenly spaced along each of six chords. Linear and second-order least-squares curve fits were applied to the data of each of the six chords. The resulting node lines are shown in figure 4. The chordwise deflections were linear in the streamwise direction, and the small variations of the node lines with frequency are considered to be an indication of the stiffness of the model.

Instrumentation

General Configuration

Each transducer was paired with a static-pressure orifice which, in addition to being used for static-pressure measurements, was also used as the transducer static-pressure reference. The static and unsteady pressure orifices were located on five chords. The chords are designated as chords A through E and are located at 33.7, 54.6, 59.0, 69.8, and 85.6 percent span. The 61 transducers on the upper surface

were considered the primary instrumentation, and the orifice locations for steady and unsteady pressure measurements are given in tables I and II. A smaller number of transducers on the lower surfaces of chords A and D were used to establish the geometric position for zero angle of attack relative to the tunnel airstream. The static orifices were adjacent to the unsteady transducer orifices, to minimize the static-pressure differential on the transducers, and were connected to the reference tube of the transducer by 35 ft of 0.020-in. tubing to damp out unsteady pressures from the reference orifice. A "T" in the line connected the tube to a scanning valve for static-pressure measurements.

The symmetry of the airfoil permitted the upper-surface transducers to be used to measure both upper and lower steady and unsteady pressure distributions. The "lower-surface" pressure distributions were determined by measuring the pressure distribution on the upper surface for the wing at a negative value of $\bar{\alpha}$ that was equal to the positive value of $\bar{\alpha}$ used to determine the upper-surface pressure distribution. The unsteady values of ΔC_p were obtained by vector subtraction of the upper-surface measurement from the lower-surface measurement. The control-surface hinge moments were determined from the output of a strain-gage bridge mounted in the control-surface shaft.

Unsteady Pressure Transducers

Figure 5 shows the two types of miniature pressure transducers and installations used. Flat pressure transducers, shown at the top of the figure, were used to measure wing pressures, and cylindrical transducers were used to measure pressures on the control surface. Both types had a sensitivity of approximately 15 mV/psi for a supply voltage of 15 V. The temperature-compensation modules for each transducer were outside the wing in the plenum chamber of the tunnel. With nine exceptions, the flat transducers were mounted under a flat aluminum plate in individual cavities in the wing to maintain the contour of the wing. Nine of the transducers were mounted flush with the wing surface where the surface was too thin for cavity mounting. The cylindrical control-surface transducers were mounted in a receptacle below a fitted access plate serving each row of transducers.

The transducers were calibrated statically, before and during the test, by using the reference tube. However, because each transducer involved a cavity, it was considered important to obtain a measure of the dynamic sensitivity of each gage when installed in the wing. Figure 6 shows an unsteady transducer calibrator, described in reference 11, which was constructed to make static and dynamic in situ sensitivity measurements. The calibrator consists of hydraulically driven bellows, which generate a reference unsteady pressure of variable frequency and amplitude. The unsteady pressure was applied via tubing to a calibration head which could be positioned manually over each wing pressure orifice. The calibration head contained a reference pressure transducer, and comparison of the reference and wing transducer signals provided the dynamic calibrations. As described in reference 11, proper operation of the calibration apparatus was verified by using a flush-mounted pressure transducer on a calibration plate. Essentially identical unsteady pressures were observed between the calibration head and the flush-mounted transducer. The dynamic sensitivities were measured at pressures of 0.5 to 2 psi and at frequencies of 4 Hz to 30 Hz. The results of the calibration measurement are shown in figure 7 in the form of the distribution of the ratio of static to dynamic sensitivities. All the transducers have pressure sensitivity ratios between 0.95 and 1.06. The corrected dynamic sensitivities were used in the final compilation and plotting of the data.

Test Procedures

Static calibrations of the pressure transducers were made prior to and during the test by applying vacuum and positive pressures to the reference orifice tubes.

A wind-on zero angle of attack of the wing was established prior to taking measurements. Preliminary measurements at transonic Mach numbers (0.88 to 0.96) were made at test Reynolds numbers over a range of angle of attack, and the pressures in the matching transducers on the upper and lower surface on chords A and D were compared. The angle-of-attack setting of $\Delta C_p = 0$ defined $\bar{\alpha} = 0°$ at $\bar{\delta} = 0°$ for the remainder of the test.

A preliminary survey was then made, varying Mach number and $\bar{\alpha}$, to establish the Mach number range for the initial occurrence of critical flow conditions and for the Mach number at which the shock was located on the control surface. A standard sequence of steady and unsteady pressure measurements were taken at each test-condition sequence. First, steady pressures were measured for the range of steady control-surface deflection $\bar{\delta}$ under investigation. Then, the unsteady pressures resulting from oscillations of the wing in pitch and of the control surface were measured at several frequencies. With these tests completed, M or $\bar{\alpha}$ was incremented, and the sequence was repeated. The nominal wing test frequencies were 4 Hz, 8 Hz, and 16 Hz for the wing

in pitch ($k \approx 0.08$, 0.16, and 0.32) and 8 Hz, 16 Hz, and 22 Hz ($k \approx 0.16$, 0.32, and 0.44) for the control-surface oscillations. The tunnel parameters and wing steady and unsteady configurations were shown in the control-room digital display. However, the model was controlled using the model control console digital display, which was independent of the facility computer. A software problem prevented computer recording of the static control-surface deflection, and the values used are those recorded from the control console display. Similar problems prevented measurement of the dynamic hinge moments.

Data Acquisition and Reduction

The data were acquired and processed using the TDT data acquisition system described in reference 12. The filtered time histories of the signals from the system's 50 amplifiers were converted to digital output by sample-and-hold, analog-to-digital subsystems. To obtain the 120 channels of data required for the test, the instrumentation was divided into 3 blocks of 50 channels. Unsteady data for each block were obtained in sequence, and ten common channels were recorded with each block to provide correlation. The analog signals from the 50 amplifiers were sampled simultaneously at the rate of approximately 940 samples per second per channel. Data-block switching, gains, and offsets were under computer program control. Depending on the frequency, 10 to 30 seconds of data were recorded at each data point. The number of samples analyzed per cycle was controlled by using nth-point sampling. Figures 8(a) and 8(b) are schematics of the data acquisition and reduction process used during the test.

The steady data were converted to engineering units on-line, and the pressures were displayed as chordwise distributions at the control-room computer console. The time required to calculate the Fourier coefficients in the dynamic analysis for each channel precluded routine on-line analysis of the unsteady pressures. The Fourier coefficients were obtained from an array of 1000 digitized samples truncated to an integer number of periods of oscillation containing N samples. The mean value of the array was then subtracted from each value before computing the coefficients. The relations used to resolve the amplitude and phase are

$$a_n = \frac{2}{N} \sum_{L=1}^{N} X_L \cos(2\pi n f \Delta t) \tag{1}$$

$$b_n = \frac{2}{N} \sum_{L=1}^{N} X_L \sin(2\pi n f \Delta t) \tag{2}$$

$$|A_n| = \sqrt{a_n^2 + b_n^2} \tag{3}$$

$$\phi_n = \tan^{-1}\left(\frac{b_n}{a_n}\right) \tag{4}$$

where

X_L = Lth digital sample of channel X

n = 1,2,3

Δt = sample time increment

f = frequency of surface oscillation

The tabulated phase is the value of the phase at each transducer subtracted from the phase of the oscillating surface determined in equation (4).

The coefficient of the pressure difference between the upper and lower surface ΔC_p was obtained by the vector subtraction of the upper-surface pressure coefficients $C_{p,u}$ from the lower-surface pressure coefficient $C_{p,\ell}$.

Results and Discussion

The results are divided into two sets of data—steady and unsteady pressure distributions. These distributions are presented in tabular form in a separate microfiche and in cross plots of selected pressure distributions as a function of the primary variables. Each set begins with a comparison of experimental- and linear-theory results.

The static and unsteady test conditions are given in tables III and IV, respectively. The left-hand column in each table gives the identifying code used to distinguish the data set. For example, 0.40-S-05 identifies the fifth static data point obtained at $M = 0.40$ and 0.90-D-10 identifies the tenth unsteady data point at $M = 0.90$. The computer data file is tabulated on the microfiche contained in this report. A sample data point for the wing oscillating in pitch is given in table V. As shown, each dynamic data point gives the tunnel conditions, mean angle of attack, oscillation amplitude, upper- and lower-surface pressures, and differential pressure at each orifice in terms of magnitude and phase.

Tables VI and VII are indexes of the steady and unsteady data figures. For the steady data, $C_{p,u}$ and ΔC_p are given for each chord. The unsteady data are presented in the plots only for chord D in the form of the coefficient of the normalized modulus of the pressures, $|C_{p,u}|$/deg and $|\Delta C_p|$/deg, and phase angle relative to the dynamic position of the wing or the control surface. The modulus of the lower-surface pressure coefficients $|C_{p,\ell}|$ are not given in the cross plots, but they may be found in the tables on the microfiche. Occasionally, some data were lost in the

digitizing process and could not be recovered. When $C_{p,u}$ was lost, the whole data set, $C_{p,u}$ and $C_{p,\ell}$, was deleted. When a $C_{p,\ell}$ was lost, $C_{p,\ell}$ is shown as a zero in the table at each orifice location. These points are indicated with an asterisk in the microfiche tables. Occasionally, an orifice is temporarily lost because of an electronic malfunction in which case the point is deleted from the cross-plot figure and is shown as an absolute zero in the microfiche tables.

Steady Pressures

The large sweep angle (50.40°) and the sharp leading edge result in the formation of a leading-edge vortex which begins to affect the forwardmost pressure transducers at an angle of attack of approximately 3°. (See appendix.) The presence of this vortex obscures the comparison with linear theory, especially on the outboard chords. The first comparisons, for chord D, are made with linear-theory results calculated using the RHOIV code (ref. 8) in figures 9 and 10. Figure 9 shows ΔC_p on chord D for $\bar{\alpha} = 3°$ at $M = 0.40$, 0.88, and 0.90. For these Mach numbers, the experimental ΔC_p is greater at the leading edge ($x/c = 0.0675$) because of the leading-edge vortex. However, at $M = 0.40$, the experimental and calculated ΔC_p are in good agreement from $x/c = 0.125$ to the trailing edge. As the Mach number is increased to 0.88, transonic aerodynamic effects are apparent, as evidenced by the usual increase in boundary-layer thickness on the aft portion of the wing, and the formation of the shock wave is evident at $M = 0.90$. Here and in succeeding figures, a decrease in ΔC_p in the neighborhood of $x/c = 0.2$ indicates the rear edge of the vortex separation bubble. Comparisons as a function of angle of attack are also made in the appendix between experimental data and SOUSSA calculations (ref. 9) for two positions in chord E ($x/c = 0.21$ and 0.26) at $M = 0.40$. These comparisons show the range of applicability of linear theory in the presence of a developing vortex at these two locations.

Figure 10 shows similar comparisons with measured data for $\bar{\delta} = 6°$ and $\bar{\alpha} = 0.05°$ at $M = 0.40$, 0.88, and 0.90. Again, the agreement between linear theory and experiment is good at $M = 0.40$. The transonic effects at $M = 0.88$ and 0.90 are evidenced by the decreasing value of ΔC_p when compared with linear analysis. Note the difference between the experimental and calculated pressure peaks near the hinge line for $M = 0.90$, where the experimental pressure peak is broader and lower than that predicted by linear theory. The following experimental results demonstrate that the pressure distribution in the region of the hinge line may be severely altered by shock position.

A second set of comparisons is shown between experimental data and the transonic small-disturbance code of reference 7. These comparisons are from a more complete set in reference 13. This code has options for a viscous boundary layer and the Murman bump, an empirical method for modeling the shock boundary-layer interaction. The boundary-layer and bump options gave essentially the same pressure distributions and shock location. The inviscid option, which was used in the calculations that follow, gave the best comparison with experiment, in that the shock location was farther aft and in better agreement with experiment. The calculated pressure distributions for the deflected control surface were made by dividing the wing into three spanwise panels and changing the local airfoil coordinates at the control-surface location for each deflection angle.

Figure 11 shows the upper-surface pressure distribution from the small-disturbance code for the wing at $M = 0.92$ for $\bar{\alpha} = 2°$ and $\bar{\delta} = 0°$. The changes in the chordwise pressure distribution with span are evident and are seen in the steady and unsteady results which follow. The experimental and calculated variation of ΔC_p with $\bar{\alpha}$ for $M = 0.90$ and $\bar{\delta} = 0°$ is shown in figure 12. There is good overall agreement between experiment and analysis up to $\bar{\alpha} = 3°$, where the formation of the leading-edge vortex becomes evident. The location of the shock wave is reasonably predicted by analysis up to $\bar{\alpha} = 4°$.

Figure 13 shows a similar comparison of experimental and calculated ΔC_p pressure distributions for $\bar{\delta} = \pm 2°$ or $\pm 6°$, $\bar{\alpha} = 2°$, and $M = 0.90$. Because of the lack of resolution of the pressure distributions caused by the finite spacing of the transducers, only a limited comparison of the experimental and calculated results can be made. However, it appears that the calculated results have larger pressures than those measured in the neighborhood of 80-percent chord; these larger pressures result in larger values of ΔC_p for the inboard chords. The pressure distributions on chord E are in surprisingly good general agreement, except that the calculated shock position for $\bar{\delta} = 6°$ is farther aft than was measured.

Pitch deflection. Figures 14 through 19 give experimental $C_{p,u}$ distributions for the five span stations for variations in M and $\bar{\alpha}$. The variation of $C_{p,u}$ with Mach number at a nominal value of $\bar{\alpha} = 0$ is shown in figure 14. Transonic compressibility effects are apparent in the increase in negative $C_{p,u}$ distribution from $M = 0.40$ to $M = 0.88$. The effects

of compressibility, as evidenced by the increasing pressure gradient at the shock, increase from chord A to chord E.

In figures 15 through 19, the variation of $C_{p,u}$ with $\bar{\alpha}$ is presented for $M = 0.40$, 0.88, 0.90, 0.92, and 0.94. The leading-edge vortex, apparent in the large values of negative $C_{p,u}$ at the leading edge, is first visible on chord D at $x/c = 0.0675$ for $\bar{\alpha} < 3°$. The vortex strength grows as $\bar{\alpha}$ increases (fig. 15) and encompasses 70 percent of chord E at $\bar{\alpha} = 5.5°$. At $M = 0.88$ (fig. 16), the evolution of the vortex is more uniform than at $M = 0.40$, in that the development is more uniform with increasing $\bar{\alpha}$. Aft of 70-percent chord, the pressure distribution is independent of $\bar{\alpha}$. The pressure distribution on chord E is significantly different than the inboard chords at higher angles of attack, because the vortex suction operates over a greater fraction of the chord. As Mach number was increased from 0.88 to 0.94 (figs. 16 through 19), the primary changes were the formation of the shock wave and an associated increase in pressure gradient as the shock wave increased in strength and moved rearward. For the range of Mach number and angle of attack shown in these figures, shock position is primarily a function of Mach number. Both $C_{p,u}$ and ΔC_p are shown for $M = 0.94$ in figures 19(a) and 19(b). The distribution of ΔC_p at $M = 0.94$ shows the influence of the vortex increasing with span until, at $\bar{\alpha} = 4.5°$, 70 percent of chord E is subject to vortex suction. With the exception of the area under the leading-edge vortex, the increase in lifting pressure is linear as $\bar{\alpha}$ increases to 4°.

Control-surface deflection. The control-surface data are examined in two groups. The primary variable in the first group (figs. 20 and 21) is Mach number, and the pressures are shown as $C_{p,u}$ and ΔC_p distributions. The primary variable for the second group (figs. 22 and 23) is control-surface deflection $\bar{\delta}$, and the pressure data are presented as ΔC_p distributions. The influence of the static control-surface deflection on the wing pressure increases with increasing span and is most apparent in the ΔC_p distributions. The loss of the control-surface influence on the wing pressure distribution is conspicuous at the higher Mach numbers as the shock wave becomes stronger and moves towards the trailing edge of the wing.

The steady pressure distributions, $C_{p,u}$ and ΔC_p, as a function of Mach number for $\bar{\delta} = \pm 6°$ and 0° at $\bar{\alpha} = 1°$ are given in figure 20 and for $\bar{\alpha} = 3°$ in figure 21. The Mach numbers are 0.88, 0.90, 0.92, and 0.94. The effect of Mach number for a positive deflection of 6° on the upper-surface pressure distribution is greatest on chord E near the tip in figure 20(a). When figure 20(a) ($\bar{\delta} = 6°$) is compared with the results in figure 20(b) ($\bar{\delta} = 0°$), it is apparent that the effect of positive deflection on the upper-surface pressure is to increase the shock strength at the lower Mach numbers ($M = 0.88$ and 0.90). In comparison, decreasing $\bar{\delta}$ to −6°, (fig. 20(c)) has the opposite effect of decreasing the shock strength at the lower Mach numbers. When the same parameters are examined for the ΔC_p distribution, the magnitude of the pressure peaks at the hinge line increases with increasing Mach number (figs. 20(d), 20(e), and 20(f)) for $\bar{\delta} = 6°$ and −6° from 0.88 to 0.92. At $M = 0.94$, the magnitude of the peaks decreases at the hinge line as the shock wave moves aft.

The sequence of pressure distributions in figure 20 is repeated in figure 21 with $\bar{\alpha} = 3°$. The comments in the preceding paragraph for the case of $\bar{\alpha} = 1°$ in figure 20 also apply to the $\bar{\alpha} = 3°$ data of figure 21, except that the shock wave has moved farther aft, and the effect of Mach number on the pressure distribution is most noticeable on chord E. The presence of the vortex is apparent on chords C and D, and the suction pressure is essentially independent of Mach number over the range from 0.88 to 0.94.

The steady pressure distributions ΔC_p as affected by positive and negative control-surface deflections of 0°, 2°, 4°, and 6° are compared in figures 22 and 23 for $\bar{\alpha} = 3°$. As in previous results, the influence of the control-surface deflection increases from root to tip.

At $M = 0.88$, the changes in the pressure distribution are linear, with incremental changes in control-surface deflection for positive and negative control deflections (figs. 22(a) and 23(a)). As Mach number is increased to 0.94, the change in pressure with control-surface deflection becomes erratic as the shock wave interacts with the pressure peak at the control-surface hinge line. At $M = 0.94$ (figs. 22(d) and 23(d)), the change in ΔC_p with $\bar{\delta}$ over the surface is minimal on the inboard chords A and B and is only apparent on the last 25 percent of chords D and E.

Static hinge moments. Control-surface static hinge moments as a function of $\bar{\delta}$ and $\bar{\alpha}$ at Mach numbers from 0.88 to 0.94 are given in terms of hinge-moment coefficient C_h in figure 24. The hinge-moment coefficient is positive for the moment forcing the trailing edge down. The variation of hinge moment with deflection displays the usual nonlinear response, with $dC_h/d\delta$ increasing as $\bar{\delta}$ increases. As Mach number is increased from 0.88 to 0.94, the shock wave moves aft, and the hinge moment increases by a factor of two.

The data at $M = 0.88$ (fig. 24(a)) have a zero offset that is not apparent at the other Mach numbers. With the exception of the $M = 0.90$ data (fig. 24(b)),

the hinge moments follow a trend of increasing C_h with increasing $\bar{\alpha}$ for negative $\bar{\delta}$. For positive values of $\bar{\delta}$, the maximum value of C_h occurred at $\bar{\alpha} = 0°$.

Oscillating Pressures

Unsteady pressures due to wing oscillation in pitch were measured at nominal pitching amplitudes of 0.25° and 0.50° and at frequencies of 4 Hz, 8 Hz, and 16 Hz ($k \approx 0.08$, 0.16, and 0.32). Unsteady pressures due to control-surface oscillation were measured at nominal peak amplitudes of 2°, 4°, and 6° at frequencies of 8 Hz, 16 Hz, and 22 Hz ($k \approx 0.16$, 0.32, and 0.44). The oscillating pressures are given in terms of modulus, normalized by amplitude in degrees, and phase. The comparisons to be shown are restricted, because of the volume of data, to chord D, which contains the control surface. (The data for the other chords are included in the microfiche.) The spanwise variation of unsteady pressures is similar to that of steady pressures, in that incremental changes in $\bar{\alpha}$ and $\bar{\delta}$ generate larger pressure changes on the outboard chords. The three mechanisms that were predominant in the static-pressure distribution—vortex, shock, and hinge-line pressure peak—are, of course, evident in the unsteady data, and comparisons between the steady and unsteady pressure signatures are made in the sections which follow. The oscillating pressure results are grouped according to the type of oscillation. The discussion of each group is initiated by comparisons with linear theory.

The phase angles from the data analysis are in the range of −180° to 180°, which results in discontinuous jumps in phase angle over the length of the chord. To get a smooth distribution of phase angle 360°, and occasionally 720°, was subtracted from the angle at the phase jump.

Wing oscillation in pitch. Comparisons of experimental $|C_{p,u}|$ and phase with linear-theory calculations (ref. 8, the same code used for the steady pressure comparisons of figs. 9 and 10) are given in figures 25 through 27. Figure 25 is for a Mach number of 0.40 ($M = 0.40$ comparisons are also made in ref. 14) at frequencies of 4 Hz, 8 Hz, and 16 Hz. The comparison is fair for all frequencies except 16 Hz (fig. 25(c)) near the leading edge. As the frequency is increased from 4 Hz to 16 Hz, the phase of the loading at the trailing edge approaches 0° (fig. 25(c)). This phase delay increases from −100° forward along the chord to a value of −200° at the leading edge.

When Mach number is increased to 0.885 (fig. 26), transonic effects are apparent. The results at $f =$ 8 Hz show an increase in experiment over linear theory for $|C_{p,u}|$ between $x/c = 0.2$ and 0.7, as does the static distribution in figures 9 and 14. This increase in $|C_{p,u}|$ is preliminary to the formation of a distinct shock wave. The experimental phase angle at the trailing edge is −50°, compared with the linear-theory angle of −125°. The two sets of phase angles become coincident at $x/c = 0.6$. The final comparison is made at $M = 0.90$ (fig. 27) for frequencies of 8 Hz and 16 Hz at $\bar{\alpha} = 0°$ and $\alpha = 0.46°$. The increase in Mach number from 0.885 to 0.90 results in the formation of a strong shock wave in which the $|C_{p,u}|$ and phase distributions are dependent on frequency. At $f = 8$ Hz (fig. 27(a)), the increased level of $|C_{p,u}|$ is similar to that in figure 26, with the addition of a shock wave at $x/c \approx 0.65$. The experimental and linear-theory phase angles are in reasonable agreement from the leading edge to 65-percent chord. At this point, the experimental phase angle decreases rapidly through the shock, and, at 95-percent chord, the difference between experiment and linear theory is approximately 150°. When the frequency is increased to 16 Hz at the same tunnel conditions (fig. 27(b)), there are substantial changes in the pressure and phase distribution. The details of the phase distribution are significantly altered over the aft half of the chord. The levels of $|C_{p,u}|$ are now closer to linear theory from the leading edge to the shock wave. The shock wave has moved aft to approximately 70-percent chord and has become stronger. The experimental phase angle deviates from linear theory from 45-percent chord to 95-percent chord with a large change through the shock. The change in $|C_{p,u}|$ and phase in this narrow Mach number region 0.885 to 0.90 (figs. 26 and 27) was the most abrupt in the transonic range.

Figures 28 through 33 give experimental results for chord D in terms of pressure moduli $|C_{p,u}|$/deg and $|\Delta C_p|$/deg and the associated phase angles. In these figures, the control-surface deflection $\bar{\delta}$ is maintained at 0° and $\bar{\alpha}$, α, M, and f are varied. The symbols are replaced with coded straight lines connected to the data points in these figures to reduce the clutter which occurs when multiple variations are shown in the same figure.

Figures 28(a) and 28(b) give results for $M = 0.40$. Figure 28(a) is for $f = 4$ Hz at $\bar{\alpha} = 0°$ and 3°. The leading-edge suction due to the vortex is evident at $\bar{\alpha} = 3°$. The influence of the vortex in phase is local and is confined to the region of the vortex. Figure 28(b) presents the effects of frequency, (4 Hz, 8 Hz, and 16 Hz) at $\bar{\alpha} = 3°$. The dynamic response increases with frequency, especially from 8 Hz to 16 Hz.

Data for $M = 0.90$ are shown in figures 29 and 30. The dynamic response as a function of $\bar{\alpha}$ is shown

for $f = 4$ Hz and 16 Hz in figures 29(a) and 29(b). The difference in the two sets of data again indicates a large increase in response due to vortex and shock mechanisms as the frequency is increased from 4 Hz to 16 Hz. There is some change in the dynamic response due to the shock wave with $\bar{\alpha}$, but this change is clearly secondary to the effects of frequency. The phase shift through the shock of 180° is more abrupt at 4 Hz than at 16 Hz. Figure 30 shows the unsteady pressure and phase distribution for 4 Hz, 8 Hz, and 16 Hz at $M = 0.90$ and $\bar{\alpha} = 3°$. The pressure amplitudes increase with frequency, and the greatest increase occurs from 8 Hz to 16 Hz. The increasing unsteady pressure amplitude associated with the shock wave with increasing frequency (figs. 27, 29, and 30) suggests a resonance condition. Because of the limitations imposed by the first natural frequency of the model, it was not possible to define a resonance-condition possibility at higher frequencies. The effects of amplitude are examined in figure 31 for $\bar{\alpha} = 3°$ and $f = 8$ Hz. Over the range of $\alpha = 0.25°$ to 0.50°, the effects of dynamic pitch angle on the pressure distribution on a per-degree basis are not large but are greater for the smaller angle.

Figure 32 is a comparison of the unsteady responses at $\bar{\alpha} = 3°$ of 3 Mach numbers (0.40, 0.88, 0.90) at frequencies of 4 Hz and 16 Hz. The pressure-magnitude data at 4 Hz (fig. 32(a)) indicate that, at this frequency, a shock is apparent only at $M = 0.90$, but examination of the phase distribution indicates the presence of a shock at $M = 0.88$. The vortex suction is approximately three times greater at $M = 0.90$ than that at 0.40. There is a loss of signal at the leading edge at $M = 0.88$. When the frequency is increased to 16 Hz (fig. 32(b)), the presence of a shock at $M = 0.88$ is now evident in the pressure-magnitude distribution and in the phase distribution.

Figure 33 shows the pressure moduli, $|C_{p,u}|$/deg and $|\Delta C_p|$/deg, and phase on all 5 chords over the Mach number range from 0.40 to 0.94 for a pitch-oscillation frequency of 16 Hz and $\bar{\alpha} = 3°$. This figure illustrates the spanwise variation in pressure and phase and indicates the distribution of pressure modulus and phase on chord D relative to the other four chords. The change in modulus at the transonic Mach numbers increases with increasing span position. The phase-angle distribution is similar on all five chords.

Control-surface oscillation. This section gives some representative unsteady pressures on chord D that result from control-surface oscillation. The effect of the interaction of the shock and the pressure peak at the control-surface hinge line is illustrated. Comparisons of experimental upper-surface pressure with linear theory are shown in figures 34 through 36.

Figures 34(a) and 34(b) compare the experimental and linear-theory (ref. 10) results at $M = 0.40$ and at $\bar{\alpha} = 0.05°$ for oscillating frequencies of 8 Hz and 16 Hz. The comparison is good in both cases, except at the leading edge and at the hinge line. Near the hinge line, the theory characteristically overpredicts the pressure amplitude, and the phase angle is greater at the leading edge. At $M = 0.879$, $\delta = 5.89°$, $\bar{\alpha} = 0.05°$, and $f = 7.8$ Hz (fig. 35), the peak pressure is again overpredicted, and the experimental phase shift increases at a faster rate from trailing edge to leading edge than the linear-theory phase angle. There is no indication of a strong shock-wave. When the Mach number is increased to 0.899 at $\delta = 1.98°$ and $\bar{\alpha} = 0.05°$ (fig. 36), the change in the pressure distribution ahead of the pressure peak is similar to that in figure 26 at $M = 0.885$. The presence of the shock is readily observed in the phase-angle distribution, where there is an abrupt change in phase ahead of the hinge line. The experimental pressure distribution is now dominated by the shock wave ahead of the hinge line, and the experimental peak pressure is at 70-percent chord. An increase in the control-surface deflection from 1.98° to 3.48° (fig. 36(b)), at the same frequency (7.8 Hz), results in a substantial change in both the experimental pressure and phase distributions. The experimental results shown in the comparisons with linear theory in figures 36(a) through 36(c) indicate that increasing the control-surface amplitude δ increases the shock strength and decreases unsteady pressure over the chord. Behind the shock, the results are consistent with shock-induced separation. When δ is increased from 1.98° to 3.48° (figs. 36(a) and 36(b)), there is a large decrease in the unsteady pressure over the control surface. A further increase to 5.90° (fig. 36(c)) results in an additional decrease in oscillatory pressure on the control surface. Ahead of the shock, the signal is reduced by the diminished oscillating pressure generated by the control-surface deflection and by the increasing resistance to upstream propagation of the signal by increased shock strength.

The data in the preceding figures are intended to illustrate the sensitivity of the pressure distribution to control-surface deflection δ and Mach number near and above the critical Mach number. Although the finite spacing of the transducers nullifies any attempt to be precise in comparison of amplitudes at the hinge line, it is evident that a shock wave ahead of the control surface significantly affects the pressure distribution generated by control-surface deflection. Also, because of the complex interaction with the

shock, the effectiveness of the control surface is not necessarily increased with increased δ.

Figures 37 and 38 compare the unsteady pressures due to control-surface deflection at Mach numbers from 0.88 to 0.94 for $\delta = 6°$. The pressure distributions at $f = 8$ Hz and 22 Hz for $\bar{\alpha} = 1°$ are shown in figures 37(a) and 37(b), respectively. At both frequencies, the unsteady pressure, $|C_{p,u}|$/deg and $|\Delta C_p|$/deg, peaks at $M = 0.92$ and then decreases at $M = 0.94$. An increase in $\bar{\alpha}$ to 3° at $f = 8$ Hz and $M = 0.94$ results in a reduction in the unsteady pressure, $|C_{p,u}|$/deg, as indicated by the comparison of the results in figure 38 with those of figure 37(a).

The effects of frequency are examined in figure 39 for $\bar{\alpha} = 3°$ and $\delta = 6°$ at $M = 0.90$, 0.92, and 0.94. The pressure magnitude, $|C_{p,u}|$/deg, shows the largest change in peak amplitude with Mach number. At $M = 0.90$, the shock appears to be ahead of the hinge line. When Mach number is increased to 0.92 (fig. 39(b)), the shock moves to the hinge line, and there is an increase in unsteady pressure. A further increase in Mach number to 0.94 results in a large decrease in unsteady pressure modulus as the shock moves onto the control surface.

The effects of amplitude δ at $M = 0.90$, 0.92, and 0.94 are shown in figure 40 for $\bar{\alpha} = 3°$ and $f = 16$ Hz. At $M = 0.90$ (fig. 40(a)), there are differences in pressure modulus due to control-surface amplitude at $M = 0.90$ which do not exist at $M = 0.92$ and 0.94 (figs. 40(b) and 40(c)). The major influences are Mach number and shock position, rather than amplitude of motion.

The final figure in this series (fig. 41) gives the unsteady pressure distribution on all five chords at $\bar{\alpha} = 3°$ and $M = 0.90$. The figure shows chordwise distribution for nominal control-surface deflections of 2.2°, 4.3°, and 6.6° at frequencies of 8 Hz and 22 Hz. As anticipated, the change in chordwise pressure distribution with span station is more pronounced for control-surface oscillation than for the pitch-oscillation results in figure 32. The difference between the amplitudes on chord B and chord E indicates that the alteration in the flow generated by the control surface on chord D propagates more readily in the outboard direction. The phase difference $\phi(\Delta C_p)$ as a function of span is greater at an oscillation frequency of 22 Hz, where the phase angle varies from 720° at the leading edge of chord A to less than 500° at chord E.

Concluding Remarks

Static and oscillatory pressure distributions were measured on a biconvex clipped delta wing at a Reynolds number of approximately 10×10^6 based on mean chord. Most of the measurements were made over a Mach number range from 0.88 to 0.94. Static and mean pitch angle varied from 0° to 5.5°, and control-surface deflections varied from −6° to 6°. The pitch-oscillation data were measured at 4 Hz, 8 Hz, and 16 Hz at amplitudes of ±0.25° and ±0.5°. The oscillating control-surface data were measured at 8 Hz, 16 Hz, and 22 Hz at amplitudes of ±2°, ±4°, and ±6°.

The interaction of wing or control-surface deflection with the formation of shock waves and a leading-edge vortex generated complex pressure distributions that were sensitive to small changes in Mach number and frequency.

A leading-edge vortex became evident in the present data at a pitch angle of less than 3°. Static pressures were nearly independent of pitch angle behind the shock and varied linearly with pitch angles up to 4° between the point of vortex reattachment and the shock. The pressure varied smoothly in the spanwise direction and increased from root to tip.

The static-pressure distribution caused by control-surface deflection varied with shock strength, shock position, and control-surface deflection. The resultant local pressure differential coefficient ΔC_p appears to vary systematically until the pitch angle is increased at Mach 0.90, where the shock strength, as evidenced by the pressure gradient, and shock position affect the linearity of the system. As the Mach number increases to 0.92, the shock moves to the hinge line, where there is a sharp rise in ΔC_p. Further rearward movement of the shock (Mach 0.94) results in positive and negative ΔC_p peaks. The spanwise propagation of pressure due to control-surface deflection was greatest in the direction of the wing tip and was negligible at the inboard chord.

Experimental static-pressure measurements at Mach 0.90 and calculations with a transonic small-disturbance code show good agreement for angles of attack up to 3°. At 4° angle of attack, the calculated shock position is farther aft than the experimental results. The leading-edge vortex prevents a meaningful comparison at the leading edge for higher angles of attack. The spacing of the control-surface static orifices precludes a detailed comparison of pressure loading due to control-surface deflection, but the calculated values of ΔC_p appear to be larger for all but the outboard chord. Steady and unsteady pressure comparisons were also made with linear theory which were especially instructive near the critical Mach number before the formation of a defined shock wave. At Mach 0.40, there was generally good agreement between measured and linear-theory results.

The moduli of the oscillating pressures, $|C_{p,u}|$/deg and $|\Delta C_p|$/deg, show the same trends as the

static-pressure distributions. The largest pressure moduli due to oscillation in pitch were generated by the leading-edge vortex and shock motion. The pressure modulus at the shock wave increased as the frequency increased from 4 Hz to 16 Hz. There were changes in the modulus caused by mean angle of attack, but they were secondary to those caused by frequency. The modulus was dependent on span position and increased from inboard to outboard.

The unsteady pressures generated by the oscillating control surface are primarily a function of the position of the static shock wave. As the shock wave moves aft with increasing Mach number, the pressure modulus increases until the shock wave is on the hinge line. As the shock moves farther aft onto the control surface, the effect of the control-surface oscillation on the wing pressure modulus decreases rapidly. The pressure modulus outboard of the control surface was significantly more affected by the control-surface oscillation than inboard of the control surface.

NASA Langley Research Center
Hampton, VA 23665-5225
July 1, 1986

Appendix

Effect of Vortex Flow on Steady-State Pressures

E. Carson Yates, Jr.
NASA Langley Research Center
Hampton, Virginia

On a sharp-edged, untwisted, uncambered wing with a moderately to highly swept leading edge, such as the wing of this study, vortex-like flow separation from the leading edge occurs as soon as the angle of attack is changed from 0°. As angle of attack is increased, the vortex increases in size and strength, and its development and influence can be traced in the measured surface pressures. Figure A1 shows upper-surface pressure coefficient as a function of angle of attack for two points on the upper surface of the clipped delta wing at Mach 0.40. Pressures are shown for points at the 85-percent semispan station at 21 percent and 26 percent of the local chord. Five distinct regions of pressure variation are evident, and each is characterized by the effect of the leading-edge-separation vortex as shown schematically at the bottom of the figure. These sketches do not represent two-dimensional flow, but they may be considered as sections normal to the leading edge and passing through the pressure-measuring point represented by the "blip" on the upper surfaces. Thus, the flow reattachment line, where the flow impinges on the surface downstream of the vortex, is not a stagnation line but is the location of maximum pressure.

The five regions of pressure variation are characterized as follows. First, in the range $-2° < \bar{\alpha} < 2°$, the vortex is weak and small, and there is no evidence of vortex effect at the two pressure-measuring points. The pressure variation is linear with angle of attack and is in very good agreement with values calculated by the SOUSSA surface-panel method. (See refs. 9 and 15.) Second, as angle of attack decreases from $-2°$, the vortex on the lower surface becomes stronger and induces flow from the upper surface around the leading edge. Pressures at the measuring points ($x/c = 0.21$ and 0.26) are reduced slightly from values they would assume in the absence of the vortex, and the C_p curve deviates upward from the straight line. Third, as angle of attack increases from 2° to about 3.5° for the forward point ($x/c = 0.21$), the vortex on the upper surface becomes larger, and the reattachment line approaches the measuring points. The approach of this relatively high-pressure region causes the surface pressure to actually increase slightly, even though angle of attack is increasing. Fourth, as the reattachment line moves downstream from the points ($\alpha > 3.5°$), the separation vortex itself is becoming larger and stronger and is approaching the points. The combination of receding high pressure and approaching very low pressure under the vortex causes the measured pressure to decrease rapidly with increasing angle of attack. Fifth, as the vortex passes over the point ($\alpha \approx 6°$ for $x/c = 0.21$), surface pressure reaches a minimum and increases again with increasing angle of attack as the vortex moves farther downstream.

For $x/c = 0.26$, the same behavior is observed but is delayed to slightly higher angle of attack. The same behavior is also observed for points farther inboard and closer to the leading edge. Similar variations of pressure are evident in cross plots of the data given in reference 16 for an arrow-wing supersonic-cruise configuration.

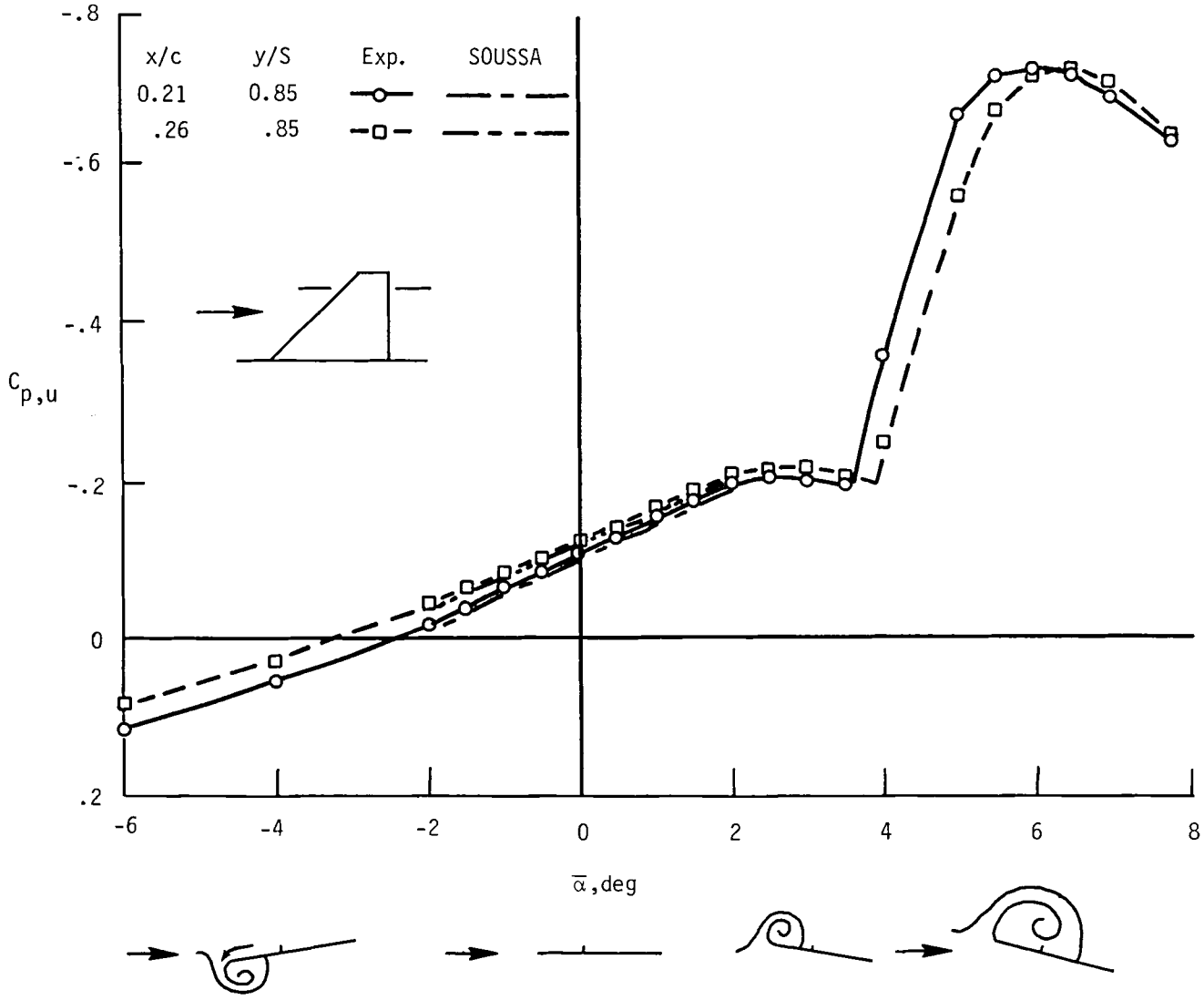

Figure A1. Steady pressures as a function of angle of attack for two orifice locations on chord E at $M = 0.40$ and $R = 2 \times 10^6$.

References

1. Tijdeman, H.: *Investigation of the Transonic Flow Around Oscillating Airfoils.* Rep. NLR TR-77090 U, Nat. Luchtvaartlab. (Amsterdam), 1977. (Available from DTIC as AD B027 633.)
2. Davis, Sanford S.; and Malcolm, Gerald N.: *Experimental Unsteady Aerodynamics of Conventional and Supercritical Airfoils.* NASA TM-81221, 1980.
3. Sandford, Maynard C.; and Ricketts, Rodney H.: *Steady- and Unsteady-Pressure Measurements on a Supercritical-Wing Model With Oscillating Control Surfaces at Subsonic and Transonic Speeds.* NASA TM-84543, 1983.
4. Ricketts, Rodney H.; Sandford, Maynard C.; Watson, Judith J.; and Seidel, David A.: *Subsonic and Transonic Unsteady- and Steady-Pressure Measurements on a Rectangular Supercritical Wing Oscillated in Pitch.* NASA TM-85765, 1984.
5. Horsten, J. J.; Den Boer, R. G.; and Zwaan, R. J.: *Unsteady Transonic Pressure Measurements on a Semi-Span Wind-Tunnel Model of a Transport-Type Supercritical Wing (LANN Model). Part II: Pressure Distributions (Plotted) and Plots of the Vibration Modes.* AFWAL-TR-83-3039, Pt. II, U.S. Air Force, Mar. 1983. (Available from DTIC as AD A130 488.)
6. *Compendium of Unsteady Aerodynamic Measurements.* AGARD-R-702, Aug. 1982.
7. Mason, William H.; MacKenzie, Donald; Stern, Mark; Ballhaus, William F.; and Frick, Juanita: *An Automated Procedure for Computing the Three-Dimensional Transonic Flow Over Wing-Body Combinations, Including Viscous Effects. Volume I—Description of Analysis Methods and Applications.* AFFDL-TR-77-122, Vol. I, Feb. 1978. (Available from DTIC as AD A055 899.)
8. Rowe, W. S.; Sebastian, J. D.; and Petrarca, J. R.: *Reduction of Computer Usage Costs in Predicting Unsteady Aerodynamic Loadings Caused by Control Surface Motions—Analysis and Results.* NASA CR-3009, 1979.
9. Morino, Luigi: *Steady, Oscillatory, and Unsteady Subsonic and Supersonic Aerodynamics—Production Version (SOUSSA-P 1.1). Volume I—Theoretical Manual.* NASA CR-159130, 1980.
10. Borgmann, Gerald E.; and Sevart, Francis D.: Design and Evaluation of Miniature Control Surface Actuation Systems for Aeroelastic Models. *J. Aircr.*, vol. 12, no. 3, Mar. 1975, pp. 129–134.
11. Bolt, Pamela A.; Hess, Robert W.; and Davis, William T.: *Portable Dynamic Pressure Generator for Static and Dynamic Calibration of In Situ Pressure Transducers.* NASA TM-85687, 1983.
12. Cole, Patricia H.: *Wind Tunnel Real-Time Data Acquisition System.* NASA TM-80081, 1979.
13. Hess, R. W.; Wynne, E. C.; and Cazier, F. W., Jr.: *Static and Unsteady Pressure Measurements on a 50 Degree Clipped Delta Wing at $M = 0.9$.* NASA TM-83297, 1982.
14. Yates, E. Carson, Jr.; Cunningham, Herbert J.; Desmarais, Robert N.; Silva, Walter A.; and Drobenko, Bohdan: *Subsonic Aerodynamic and Flutter Characteristics of Several Wings Calculated by the SOUSSA P1.1 Panel Method.* NASA TM-84485, 1982.
15. Smolka, Scott A.; Preuss, Robert D.; Tseng, Kadin; and Morino, Luigi: *Steady, Oscillatory, and Unsteady Subsonic and Supersonic Aerodynamics—Production Version 1.1 (SOUSSA-P 1.1). Volume II—User/Programmer Manual.* NASA CR-159131, 1980.
16. Manro, Marjorie E.; Moulijn, Johan P.; and Knittel, James D.: *Pressure Distributions on a Delta Wing-Horizontal Stabilizer Combination at Mach Numbers from 0.3 to 2.9.—Volume 6, Wing Chordwise Pressure Distribution—Nacelles Off.* FAA-SS-72-30-6, July 1972.

TABLE I. STEADY ORIFICE LOCATIONS FOR UPPER SURFACE

Chord	A	B	C	D	E
y/S	0.332	0.541	0.587	0.694	0.851
y, in.	14.99	24.39	26.45	31.27	38.38
c, in.	45.42	34.05	31.55	25.73	17.13
Orifice number	x/c				
1	0.0778	0.0687	0.0818	0.0675	0.2070
2	.1264	.1282	.1318	.1151	.2559
3	.2020	.2529	.2099	.1980	.3016
4	.2523	.3041	.7875	.2559	.3537
5	.3023	.3531	.8522	.3041	.4583
6	.3519	.4530	.9017	.3545	.5562
7	.4510	.5036	.9514	.4537	.6074
8	.5523	.5534		.5025	.6577
9	.6025	.6040		.5527	.7071
10	.6515	.6528		.6038	.7975
11	.6991	.7030		.6538	
12	.7813	.7694		.7025	
13	.8505	.8967		.7754	
14	.9001	.9512		.8553	
15	.9596			.9037	
16				.9526	

TABLE II. UNSTEADY ORIFICE LOCATIONS FOR UPPER SURFACE

Chord	A	B	C	D	E
y/S	0.337	0.546	0.590	0.698	0.856
y, in.	15.19	24.59	26.60	31.48	38.57
c, in.	45.17	33.81	31.38	25.47	16.90
Orifice number	x/c				
1	0.0731	0.0681	0.0767	0.0754	0.1955
2	.1120	.1217	.1271	.1237	.2458
3	.1974	.2485	.1993	.1980	.2915
4	.2478	.3004	.7802	.2502	.3454
5	.2987	.3481	.8514	.3001	.4519
6	.3486	.4487	.9016	.3476	.5497
7	.4477	.4997	.9511	.4495	.6025
8	.5506	.5500		.4974	.6545
9	.6009	.6014		.5484	.7049
10	.6459	.6494		.6007	.7808
11	.6979	.6995		.6514	
12	.7805	.7747		.7000	
13	.8500	.8964		.7795	
14	.8996			.8547	
15	.9495			.9033	
16				.9522	

TABLE III. STATIC PRESSURE TEST CONDITIONS

M = 0.40

Code[1]	M	q, psf	T_0, R	p_t, psf	$\bar{\alpha}$, deg	$\bar{\delta}$, deg	R
0.40-S-01	0.399	82.7	547.5	1004.2	0.05	0	9.35×10^6
.40-S-02	.405	85.2	547.6	1004.8	.05	2	9.49
.40-S-03	.406	85.3	548.0	1004.7	.05	4	9.50
.40-S-04	.405	85.0	547.9	1004.6	.05	6	9.52
.40-S-05	.401	76.6	520.1	917.1	.54	0	9.24
.40-S-06	.400	76.4	520.7	917.9	1.03	0	9.21
.40-S-07	.402	77.1	521.0	919.2	1.51	0	9.25
.40-S-08	.401	76.6	521.8	919.7	2.01	0	9.21
.40-S-09	.404	78.1	525.2	925.7	2.52	0	9.24
.40-S-10	.403	78.0	525.5	926.2	2.79	0	9.23
.40-S-11	.404	78.4	525.7	926.7	3.04	0	9.25
.40-S-12	.404	78.9	527.8	932.4	3.55	0	9.32
.40-S-13	.408	80.2	525.5	932.2	4.05	0	9.27
.40-S-14	.403	79.2	532.5	941.6	4.54	0	9.17
.40-S-15	.403	78.3	527.8	932.6	5.04	0	9.22
.40-S-16	.401	78.3	532.4	940.4	5.54	0	9.16
.40-S-17	.405	74.7	512.5	877.9	.05	0	9.11
.40-S-18	.404	78.7	527.8	931.8	3.30	0	9.24
.40-S-19	.404	78.6	525.7	929.5	3.80	0	9.28
.40-S-20	.402	79.3	536.2	947.2	4.29	0	9.15
.40-S-21	.402	79.2	536.4	946.5	4.77	0	9.14
.40-S-22	.402	78.6	531.7	939.7	5.29	0	9.18
.40-S-23	.404	80.2	537.9	950.1	-.22	0	9.20

[1]Codes are defined in section "Results and Discussion."

TABLE III. Continued

M = 0.88

Code[1]	M	q, psf	T_0, R	p_t, psf	$\bar{\alpha}$, deg	$\bar{\delta}$, deg	R
0.88-S-1	0.883	185.0	557.9	664.7	0.05	0	9.79×10^6
.88-S-2	.881	181.0	548.2	631.4	.05	2	9.84
.88-S-3	.886	183.4	547.9	635.3	.05	4	9.95
.88-S-4	.884	182.4	549.0	634.0	.05	6	9.86
.88-S-5	.880	184.2	556.9	643.9	.54	0	9.80
.88-S-6	.881	184.8	530.5	645.3	1.03	0	9.81
.88-S-7	.882	185.1	529.9	645.7	1.03	2	9.83
.88-S-8	.880	184.8	559.5	645.9	1.03	4	9.85
.88-S-9	.885	186.4	557.0	647.7	1.03	6	9.87
.88-S-10	.884	186.4	559.0	648.0	1.03	-2	9.82
.88-S-11	.885	186.4	558.9	647.9	1.03	-4	9.83
.88-S-12	.881	185.0	558.5	646.4	1.03	-6	9.80
.88-S-13	.887	188.0	561.0	651.7	1.51	0	9.83
.88-S-14	.884	187.2	561.2	651.5	2.02	0	9.82
.88-S-15	.881	186.0	561.2	649.7	2.02	2	9.78
.88-S-16	.882	186.4	561.4	650.5	2.02	4	9.79
.88-S-17	.884	187.3	561.3	651.5	2.02	6	9.80
.88-S-18	.882	186.4	561.2	650.6	2.02	-2	9.79
.88-S-19	.878	185.5	561.7	650.5	2.02	-4	9.77
.88-S-20	.882	186.8	561.5	651.9	2.02	-6	9.81
.88-S-21	.882	187.5	560.2	653.8	2.50	0	9.87
.88-S-22	.880	186.8	560.7	653.6	3.04	0	9.80
.88-S-23	.888	189.8	562.2	657.1	3.04	2	9.87
.88-S-24	.877	186.1	560.7	653.9	3.04	4	9.80
.88-S-25	.882	187.5	562.6	653.9	3.04	6	9.81
.88-S-26	.884	188.6	560.4	656.3	3.04	-2	9.83
.88-S-27	.882	187.7	562.5	654.8	3.04	-4	9.82
.88-S-28	.885	189.0	562.1	656.8	3.04	-6	9.87
.88-S-29	.884	189.2	561.8	658.1	3.55	0	9.90
.88-S-30	.885	189.4	563.3	658.5	4.05	0	9.87
.88-S-31	.881	188.1	561.2	657.4	4.55	0	9.87

[1]Codes are defined in section "Results and Discussion."

TABLE III. Continued

M = 0.90

Code[1]	M	q, psf	T_o, R	p_t, psf	$\bar{\alpha}$, deg	$\bar{\delta}$, deg	R
0.90-S-1	0.899	191.2	565.3	651.8	0.05	0	9.77×10^6
.90-S-2	.898	190.8	562.9	651.9	.05	2	9.83
.90-S-3	.896	190.4	563.0	652.0	.05	4	9.82
.90-S-4	.898	190.9	565.1	652.0	.04	6	9.78
.90-S-5	.909	199.7	565.7	673.5	.99	0	10.11
.90-S-6	.902	197.3	564.7	671.4	.99	2	10.08
.90-S-7	.901	197.1	564.1	671.0	.99	4	10.09
.90-S-8	.901	197.0	563.7	670.3	.99	6	10.08
.90-S-9	.905	198.3	563.7	671.6	.99	-2	10.12
.90-S-10	.902	197.2	563.3	670.6	.99	-4	10.10
.90-S-11	.904	197.9	563.0	670.9	.99	-6	10.13
.90-S-12	.898	187.2	551.3	639.1	1.97	0	9.91
.90-S-13	.906	190.2	552.2	642.8	1.97	2	9.97
.90-S-14	.902	189.5	553.2	643.3	1.97	4	9.94
.90-S-15	.903	189.7	554.7	643.3	1.97	6	9.90
.90-S-16	.902	189.8	555.4	644.4	1.97	-2	9.90
.90-S-17	.903	190.0	556.5	645.0	1.97	-4	9.88
.90-S-18	.904	190.6	554.4	646.0	1.97	-6	9.96
.90-S-19	.900	192.7	566.2	656.8	2.99	0	9.80
.90-S-20	.902	193.3	566.8	657.7	2.99	2	9.81
.90-S-21	.901	193.1	566.3	657.4	2.99	4	9.81
.90-S-22	.902	193.5	566.5	658.0	2.99	6	9.86
.90-S-23	.902	193.6	567.1	658.6	2.99	-2	9.81
.90-S-24	.896	192.1	566.6	657.8	2.99	-4	9.80
.90-S-25	.906	195.0	566.9	659.7	2.99	-6	9.87
.90-S-26	.903	193.5	557.6	657.3	4.00	0	10.05
.90-S-27	.901	194.1	562.3	661.0	3.99	2	9.99
.90-S-28	.902	194.4	561.6	661.4	3.99	4	10.02
.90-S-29	.909	196.8	562.3	664.0	3.99	6	10.09
.90-S-30	.903	195.8	562.8	664.7	3.99	-2	10.04
.90-S-31	.903	195.5	564.1	663.7	3.99	-4	10.00
.90-S-32	.903	195.6	563.4	664.3	3.99	-6	10.02
.90-S-33	.905	188.6	549.3	637.6	1.46	0	9.96
.90-S-34	.902	193.5	565.6	657.9	2.45	0	9.85
.90-S-35	.903	192.0	553.6	651.2	3.25	0	10.08
.90-S-36	.896	190.5	552.5	652.2	3.49	0	10.06
.90-S-37	.903	192.8	556.8	654.6	3.75	0	10.05
.90-S-38	.901	193.1	556.7	657.2	4.24	0	10.08
.90-S-39	.902	193.7	559.7	658.6	4.49	0	10.03

[1]Codes are defined in section "Results and Discussion."

TABLE III. Continued

M = 0.92

Code[1]	M	q, psf	T_o, R	p_t, psf	$\bar{\alpha}$, deg	$\bar{\delta}$, deg	R
0.92-S-1	0.921	193.8	541.7	643.0	0.05	0	10.35 × 10^6
.92-S-2	.919	194.0	546.1	645.7	.05	2	10.26
.92-S-3	.921	195.8	547.2	650.0	.05	4	10.30
.92-S-4	.921	196.1	550.6	651.0	.05	6	10.21
.92-S-5	.921	200.0	558.1	663.4	.54	0	10.22
.92-S-6	.921	200.0	557.0	664.0	1.04	0	10.26
.92-S-7	.923	200.4	559.2	664.4	1.04	2	10.21
.92-S-8	.923	200.5	559.5	664.7	1.04	4	10.21
.92-S-9	.921	200.2	558.7	664.7	1.04	6	10.22
.92-S-10	.922	200.5	558.9	664.8	1.04	-2	10.22
.92-S-11	.927	202.6	557.9	667.7	1.04	-4	10.31
.92-S-12	.300	201.0	558.7	665.6	1.04	-6	10.24
.92-S-13	.923	202.4	559.9	670.6	1.51	0	10.28
.92-S-14	.923	202.2	562.3	670.4	2.02	0	10.22
.92-S-15	.923	203.3	562.6	672.4	2.02	2	10.25
.92-S-16	.923	202.4	560.1	670.6	2.02	4	10.28
.92-S-17	.922	202.2	561.0	671.0	2.02	6	10.26
.92-S-18	.922	202.1	562.0	670.6	2.02	-2	10.22
.92-S-19	.922	202.0	562.4	670.4	2.02	-4	10.24
.92-S-20	.922	202.0	562.4	670.6	2.02	-6	10.21
.92-S-21	.920	202.8	561.7	674.2	2.51	0	10.28
.92-S-22	.921	203.3	532.1	675.4	2.78	0	10.23
.92-S-23	.921	203.2	563.3	674.8	3.04	0	10.25
.92-S-24	.919	202.8	564.5	675.5	3.03	2	10.21
.92-S-25	.918	202.7	562.0	675.4	3.03	4	10.28
.92-S-26	.920	203.2	564.5	676.2	3.03	6	10.23
.92-S-27	.919	203.0	564.5	675.8	3.03	-2	10.22
.92-S-28	.919	203.1	561.8	675.9	3.03	-4	10.30
.92-S-29	.920	203.1	564.0	675.6	3.03	-6	10.24
.92-S-30	.922	204.3	563.2	678.0	3.28	0	10.30
.92-S-31	.921	204.0	562.4	677.5	3.54	0	10.31
.92-S-32	.922	204.1	564.4	677.7	3.80	0	10.26
.92-S-33	.923	205.0	564.0	679.7	4.04	0	10.30

[1]Codes are defined in section "Results and Discussion."

TABLE III. Continued

M = 0.94

Code[1]	M	q, psf	T_o, R	p_t, psf	$\bar{\alpha}$, deg	$\bar{\delta}$, deg	R
0.94-S-1	0.944	203.7	562.5	658.6	0.05	0	10.07×10^6
.94-S-2	.946	204.0	563.5	658.8	.05	2	10.05
.94-S-3	.944	203.7	562.1	658.9	.05	4	10.09
.94-S-4	.946	204.1	561.1	658.8	.05	6	10.07
.94-S-5	.944	200.0	557.3	646.8	.49	0	10.00
.94-S-6	.943	199.9	557.1	647.4	.97	0	10.04
.94-S-7	.943	199.6	557.6	646.2	.97	2	10.01
.94-S-8	.944	200.3	557.8	647.4	.97	4	10.01
.94-S-9	.944	200.4	558.4	648.2	.97	6	10.02
.94-S-10	.943	200.4	559.6	649.1	.97	-2	10.00
.94-S-11	.942	199.8	558.0	647.8	.97	-4	10.03
.94-S-12	.944	200.5	557.3	648.3	.97	-6	10.05
.94-S-13	.943	201.7	562.3	653.3	1.46	0	9.99
.94-S-14	.940	201.0	562.7	653.3	1.96	0	9.97
.94-S-15	.944	202.6	562.7	655.4	1.96	2	10.02
.94-S-16	.940	201.4	563.6	654.8	1.96	4	9.97
.94-S-17	.944	202.8	563.2	655.7	1.96	6	10.01
.94-S-18	.947	203.9	563.2	657.8	1.96	-2	10.05
.94-S-19	.941	202.2	556.6	656.2	1.96	-4	9.99
.94-S-20	.948	204.6	558.3	658.5	1.96	-6	10.03
.94-S-21	.942	199.2	558.1	645.4	2.52	0	9.99
.94-S-22	.940	199.3	556.6	646.9	2.79	0	10.04
.94-S-23	.943	200.5	558.3	648.8	3.05	0	9.99
.94-S-24	.944	200.8	558.1	649.7	3.05	2	10.01
.94-S-25	.942	200.2	557.5	648.6	3.05	4	10.05
.94-S-26	.948	202.1	559.4	650.5	3.05	6	10.05
.94-S-27	.943	200.5	559.8	649.5	3.05	-2	10.00
.94-S-28	.944	201.2	558.6	650.7	3.05	-4	10.05
.94-S-29	.943	201.0	560.0	650.6	3.05	-6	10.01
.94-S-30	.940	200.9	560.3	653.3	3.30	0	10.04
.94-S-31	.941	201.5	561.2	654.3	3.54	0	9.98
.94-S-32	.942	201.7	562.6	654.2	3.80	0	10.00
.94-S-33	.943	202.8	561.5	656.4	4.05	0	10.03
.94-S-34	.942	202.1	561.8	654.9	4.05	2	10.03
.94-S-35	.944	203.0	562.4	656.5	4.05	4	10.04
.94-S-36	.943	202.3	562.5	655.5	4.05	6	10.02
.94-S-37	.946	203.8	563.6	657.9	4.05	-2	10.03
.94-S-38	.940	201.8	563.2	656.1	4.05	-4	10.00
.94-S-39	.948	204.3	563.5	658.0	4.05	-6	10.04
.94-S-40	.940	201.3	561.3	654.1	4.29	0	10.07
.94-S-41	.943	202.2	562.4	654.8	4.59	0	10.01

[1]Codes are defined in section "Results and Discussion."

TABLE III. Concluded

M = 0.96

Code[1]	M	q, psf	T_o, R	p_t, psf	$\bar{\alpha}$, deg	$\bar{\delta}$, deg	R
0.96-S-1	0.965	197.1	551.9	622.7	0.00	0	9.81×10^6
.96-S-2	.964	197.1	555.5	623.5	0.00	2	9.73
.96-S-3	.962	196.6	555.7	623.2	0.00	4	9.72
.96-S-4	.961	196.6	555.5	624.2	0.00	6	9.73
.96-S-5	.960	199.5	566.4	634.0	.53	0	9.63
.96-S-6	.961	199.8	566.2	634.8	1.02	0	9.62

M = 1.12

Code[1]	M	q, psf	T_o, R	p_t, psf	$\bar{\alpha}$, deg	$\bar{\delta}$, deg	R
1.12-S-1	1.120	230.4	572.5	641.3	0.00	0	9.68×10^6
1.12-S-2	1.120	230.6	532.7	642.2	0.00	2	9.59
1.12-S-3	1.120	231.1	575.9	642.5	0.00	4	9.61
1.12-S-4	1.120	230.6	575.4	641.5	0.00	6	9.61
1.12-S-5	1.120	230.9	570.5	641.5	.50	0	9.66
1.12-S-6	1.120	231.7	573.2	643.0	.99	0	9.70

[1]Codes are defined in section "Results and Discussion."

TABLE IV. UNSTEADY PRESSURE TEST CONDITIONS

M = 0.40

Code[1]	M	q, psf	T_0, R	p_t, psf	$\bar{\alpha}$, deg	α, deg	δ, deg	R	f, Hz	k
0.40-D-01	0.406	76.6	515.2	898.0	0.05	0.24	0.00	9.24×10^6	16.00	0.7710
.40-D-02	.404	76.9	515.7	910.9	.05	.47	0.00	9.37	16.00	.7740
.40-D-03	.403	77.1	517.3	913.4	.05	.24	0.00	9.32	7.97	.3850
.40-D-04	.404	77.3	518.2	914.5	.05	.26	0.00	9.31	4.00	.1930
.40-D-05	.403	76.9	518.7	915.1	.05	.47	0.00	9.28	4.00	.1940
.40-D-06	.403	77.1	517.9	916.1	.05	.46	0.00	9.32	7.99	.3890
.40-D-07	.400	76.5	522.4	920.6	2.01	.23	0.00	9.19	16.01	.7750
.40-D-08	.403	77.5	522.8	921.6	2.01	.46	0.00	9.24	15.99	.7720
.40-D-09	.403	77.7	521.9	922.2	2.01	.23	0.00	9.28	7.97	.3830
.40-D-10	.403	77.6	521.8	922.8	2.01	.47	0.00	9.24	7.96	.3830
.40-D-11	.402	77.5	523.1	924.2	2.01	.25	0.00	9.25	4.00	.1910
.40-D-12	.402	77.5	523.5	924.7	2.01	.51	0.00	9.25	4.00	.1920
.40-D-13	.404	78.6	524.4	927.5	3.04	.23	0.00	9.29	16.00	.7680
.40-D-14	.404	78.5	526.7	928.3	3.04	.46	0.00	9.28	16.01	.7670
.40-D-15	.403	78.3	527.2	929.3	3.04	.23	0.00	9.22	7.99	.3830
.40-D-16	.403	78.3	527.5	929.8	3.04	.46	0.00	9.22	7.99	.3830
.40-D-17	.400	77.2	527.8	929.9	3.05	.24	0.00	9.18	4.00	.1920
.40-D-18	.404	78.7	527.5	931.2	3.04	.50	0.00	9.25	4.00	.1920
.40-D-19	.401	77.8	527.9	933.9	5.03	.23	0.00	9.20	7.99	.3830
.40-D-20	.407	80.3	529.9	937.3	5.01	.47	0.00	9.31	7.98	.3820
.40-D-21	.403	78.8	530.5	936.4	5.03	.23	0.00	9.20	16.01	.7650
.40-D-22	.404	79.0	531.0	937.4	5.01	.47	0.00	9.21	16.00	.7620
.40-D-23	.408	81.0	531.7	941.1	5.04	.24	0.00	9.32	4.00	.1920
.40-D-24	.403	78.8	532.0	939.0	5.02	.50	0.00	9.18	4.00	.1890
.40-D-25	.403	79.1	533.6	942.1	4.52	.24	0.00	9.21	16.01	.7640
.40-D-26	.403	79.3	532.3	943.1	4.51	.46	0.00	9.22	16.03	.7650
.40-D-27	.401	78.6	534.8	943.8	4.53	.24	0.00	9.13	7.99	.3810
.40-D-28	.402	79.1	534.9	944.3	4.51	.48	0.00	9.15	7.98	.3820
.40-D-29	.399	77.8	535.4	944.7	4.51	.25	0.00	9.07	4.00	.1910
.40-D-30	.402	79.3	535.7	945.9	4.51	.51	0.00	9.18	4.00	.1910
.40-D-31	.405	85.2	545.8	1004.5	.05	0.00	1.95	9.52	7.99	.3750
.40-D-32	.405	84.9	547.8	1004.3	.05	0.00	3.90	9.46	7.99	.3760
.40-D-33	.405	84.9	546.8	1002.9	.05	0.00	5.86	9.48	7.99	.3760
.40-D-34	.405	84.7	544.6	1002.9	.05	0.00	1.94	9.53	16.00	.7530
.40-D-35	.405	84.9	544.6	1002.9	.05	0.00	3.90	9.53	15.98	.7470
.40-D-36	.404	84.6	546.6	1002.6	.05	0.00	5.77	9.47	15.98	.7540
.40-D-37	.409	86.5	546.7	1004.6	.05	0.00	1.92	9.58	21.96	1.0350
.40-D-38	.404	73.7	512.6	870.9	.05	0.00	3.88	9.01	22.01	1.0700
.40-D-39	.404	73.8	513.4	871.9	.05	0.00	5.76	9.01	21.99	1.0650

[1]Codes are defined in section "Results and Discussion."

TABLE IV. Continued

M = 0.88

Code[1]	M	q, psf	T_o, R	p_t, psf	$\bar{\alpha}$ deg	α, deg	δ, deg	R	f, Hz	k
0.88-D-1	.877	182.0	556.5	641.9	.05	.24	0.00	9.77×10^6	4.00	.0880
.88-D-2	.885	8.0	555.6	643.3	.05	.24	0.00	9.84	7.99	.1740
.88-D-3	.885	185.1	555.5	642.1	.05	.24	0.00	9.83	16.00	.3470
.88-D-4	.884	184.8	556.1	644.9	.05	.51	0.00	9.85	4.00	.0860
.88-D-5	.885	185.5	556.6	644.0	.05	.48	0.00	9.83	7.98	.1730
.88-D-7	.876	184.6	560.9	648.6	1.00	.25	0.00	9.76	4.03	.0870
.88-D-8	.878	184.7	560.8	648.2	1.03	.24	0.00	9.76	7.96	.1740
.88-D-9	.880	185.5	559.6	648.4	1.03	.23	0.00	9.80	16.01	.3480
.88-D-10	.878	184.9	561.0	648.8	1.03	.46	0.00	9.76	4.03	.0870
.88-D-11	.879	185.5	560.7	649.3	1.03	.48	0.00	9.78	7.96	.1740
.88-D-12	.880	185.5	559.3	648.8	1.03	.47	0.00	9.81	16.00	.3480
.88-D-13	.883	187.5	560.4	653.2	2.01	.24	0.00	9.86	7.98	.1730
.88-D-14	.877	185.6	561.9	651.3	2.01	.23	0.00	9.78	15.98	.3480
.88-D-15	.882	187.9	562.6	654.9	2.01	.46	0.00	9.82	4.00	.0860
.88-D-16	.880	186.6	561.9	652.5	2.01	.48	0.00	9.80	7.99	.1730
.88-D-17	.882	187.3	561.8	653.5	2.01	.46	0.00	9.77	16.00	.3460
.88-D-18	.880	187.7	562.2	656.3	3.04	.26	0.00	9.85	4.00	.0870
.88-D-19	.884	188.7	561.2	656.4	3.04	.23	0.00	9.93	7.98	.1730
.88-D-20	.884	189.0	563.5	658.0	3.04	.23	0.00	9.85	16.00	.3450
.88-D-21	.881	188.0	563.1	656.3	3.04	.51	0.00	9.83	4.00	.0870
.88-D-22	.879	187.3	563.6	655.8	3.04	.48	0.00	9.80	7.99	.1730
.88-D-23	.886	189.8	561.1	658.8	3.04	.47	0.00	9.93	16.01	.3450
.88-D-24	.883	188.7	562.9	657.7	4.03	.24	0.00	9.89	4.00	.0860
.88-D-25	.879	187.7	563.4	657.4	4.04	.23	0.00	9.83	7.99	.1730
.88-D-26	.883	188.7	562.4	657.5	4.03	.24	0.00	9.87	16.00	.3460
.88-D-27	.885	189.9	563.2	659.8	4.03	.49	0.00	9.87	4.00	.0860
.88-D-28	.884	189.5	563.3	659.0	4.03	.48	0.00	9.87	7.99	.1720
.88-D-29	.887	187.0	563.2	656.5	4.03	.47	0.00	9.81	16.00	.3480
.88-D-30	.884	183.7	552.3	638.2	.05	0.00	1.97	9.84	7.99	.1740
.88-D-31	.883	183.2	552.9	638.0	.05	0.00	3.90	9.82	7.99	.1740
.88-D-32	.879	182.0	553.3	636.8	.05	0.00	5.89	9.80	7.99	.1750
.88-D-33	.879	182.5	552.0	639.0	.05	0.00	1.96	9.85	16.01	.3510
.88-D-34	.878	182.1	554.5	638.1	.05	0.00	3.88	9.77	16.00	.3500
.88-D-35	.879	182.4	554.4	638.3	.05	0.00	5.84	9.80	16.00	.3500
.88-D-36	.880	182.9	552.4	639.2	.05	0.00	1.97	9.85	21.99	.4810
.88-D-37	.884	184.1	554.7	640.4	.05	0.00	3.86	9.81	21.99	.4780
.88-D-38	.881	183.5	553.7	640.5	.05	0.00	5.77	9.84	21.99	.4800
.88-D-39	.879	184.6	559.5	646.7	1.03	0.00	1.98	9.77	7.99	.1740
.88-D-40	.881	185.2	559.7	646.9	1.03	0.00	3.93	9.84	8.00	.1740
.88-D-41	.882	185.7	559.2	647.6	1.03	0.00	5.90	9.81	7.99	.1740
.88-D-42	.877	184.1	558.0	646.7	1.03	0.00	1.96	9.80	15.99	.3500
.88-D-43	.883	186.3	559.7	648.7	1.03	0.00	3.87	9.83	16.01	.3470
.88-D-44	.880	185.0	559.2	647.3	1.03	0.00	5.79	9.80	16.01	.3480
.88-D-45	.883	186.4	559.1	649.4	1.03	0.00	1.93	9.84	21.99	.4770
.88-D-46	.885	186.9	559.4	649.6	1.03	0.00	3.88	9.84	21.96	.4760
.88-D-47	.881	185.5	560.4	648.0	1.03	0.00	5.83	9.78	21.99	.4780
.88-D-48	.879	185.6	561.6	650.5	2.02	0.00	3.92	9.78	7.99	.1740
.88-D-49	.883	186.9	561.5	651.3	2.02	0.00	6.01	9.81	7.98	.1730

[1]Codes are defined in section "Results and Discussion."

TABLE IV. Continued

M = 0.88

Code[1]	M	q, psf	T_o, psf	p_t, psf	$\bar{\alpha}$ deg	α, deg	δ, deg	R	f, Hz	k
0.88-D-50	.881	186.5	561.9	651.4	2.02	0.00	1.96	9.79×10^6	16.00	.3470
.88-D-51	.882	186.9	561.5	652.4	2.02	0.00	3.89	9.82	16.00	.3470
.88-D-52	.881	186.5	561.8	651.4	2.02	0.00	5.84	9.83	15.99	.3460
.88-D-53	.886	188.4	562.2	653.9	2.02	0.00	1.96	9.84	21.97	.4740
.88-D-54	.882	186.7	561.8	651.4	2.02	0.00	3.88	9.80	21.99	.4760
.88-D-55	.882	186.9	561.6	651.9	2.02	0.00	5.76	9.81	21.97	.4760
.88-D-56	.885	189.3	563.1	657.5	3.04	0.00	1.97	9.86	7.95	.1720
.88-D-57	.882	188.2	563.3	656.7	3.04	0.00	3.91	9.83	7.96	.1730
.88-D-58	.876	186.1	560.9	654.3	3.04	0.00	5.88	9.84	7.96	.1740
.88-D-59	.882	187.9	563.2	655.7	3.04	0.00	1.97	9.82	16.00	.3460
.88-D-60	.883	188.6	563.3	656.9	3.04	0.00	3.90	9.84	16.00	.3450
.88-D-61	.880	187.1	562.2	654.8	3.04	0.00	6.14	9.82	15.99	.3470
.88-D-62	.878	186.9	563.1	655.4	3.04	0.00	1.99	9.80	21.97	.4770
.88-D-63	.877	186.6	563.1	654.8	3.04	0.00	3.85	9.79	21.96	.4780
.88-D-64	.882	187.9	563.0	655.5	3.04	0.00	5.82	9.82	21.96	.4750

[1]Codes are defined in section "Results and Discussion."

TABLE IV. Continued

M = 0.90

Code[1]	M	q, psf	T_0, R	p_t, psf	$\bar{\alpha}$, deg	α, deg	δ, deg	R	f, Hz	k
0.90-D-1	0.905	201.4	567.3	682.3	0.00	0.25	0.00	10.15 x 10^6	4.01	0.084
.90-D-2	.905	200.6	565.2	679.3	0.00	.24	0.00	10.16	7.99	.168
.90-D-3	.902	199.3	564.4	677.9	0.00	.23	0.00	10.15	16.01	.337
.90-D-4	.904	200.7	566.0	680.9	0.00	.50	0.00	10.16	4.01	.084
.90-D-5	.904	200.3	566.2	679.5	0.00	.46	0.00	10.13	7.99	.167
.90-D-6	.909	202.0	564.7	680.6	0.00	.46	0.00	10.21	16.01	.335
.90-D-7	.904	191.1	556.9	647.7	.99	.23	0.00	9.94	4.01	.085
.90-D-8	.908	192.0	555.6	647.8	.99	.23	0.00	9.99	7.99	.170
.90-D-9	.902	189.7	552.7	644.7	.99	.23	0.00	10.00	15.99	.340
.90-D-10	.906	192.3	555.5	650.2	.98	.51	0.00	10.02	4.01	.085
.90-D-11	.904	190.6	553.6	646.4	.98	.47	0.00	10.01	8.00	.170
.90-D-12	.904	190.4	554.4	645.2	.99	.46	0.00	9.97	16.01	.342
.90-D-13	.902	192.8	564.8	655.0	1.97	.24	0.00	9.83	3.99	.084
.90-D-14	.902	192.6	564.9	654.9	1.97	.23	0.00	9.81	7.98	.168
.90-D-15	.903	192.5	564.0	653.5	1.96	.23	0.00	9.82	15.95	.336
.90-D-16	.901	192.6	565.5	655.7	1.96	.49	0.00	9.81	3.99	.084
.90-D-17	.903	192.9	564.8	654.8	1.96	.47	0.00	9.82	7.98	.167
.90-D-18	.902	192.3	563.7	653.7	1.96	.46	0.00	9.83	16.00	.337
.90-D-19	.904	191.5	551.0	649.1	3.00	.27	0.00	10.12	4.00	.085
.90-D-20	.902	190.0	548.4	645.4	3.00	.24	0.00	10.13	8.00	.171
.90-D-21	.907	192.8	550.1	650.9	3.00	.23	0.00	10.08	16.00	.341
.90-D-22	.904	192.0	550.6	650.4	2.99	.50	0.00	10.16	4.00	.085
.90-D-23	.902	190.7	548.3	647.7	2.99	.47	0.00	10.17	8.00	.171
.90-D-24	.908	192.2	547.3	647.6	2.99	.47	0.00	10.21	16.01	.343
.90-D-25	.909	200.0	566.1	674.3	3.97	.24	0.00	10.01	4.001	0.84
.90-D-26	.907	199.0	565.7	672.5	3.98	.24	0.00	10.10	8.00	.167
.90-D-27	.903	197.2	566.0	671.0	3.97	0.25	0.00	10.00	16.01	.337
.90-D-28	.906	198.5	568.3	671.9	3.97	0.51	0.00	10.02	4.00	.084
.90-D-29	.902	197.6	567.0	671.7	3.97	0.46	0.00	10.04	7.99	.169
.90-D-30	.900	196.3	566.7	669.0	3.97	0.47	0.00	10.03	16.01	.337
.90-D-31	.899	191.1	564.2	652.2	.045	0.00	1.98	9.88	7.98	.169
.90-D-32	.898	190.9	563.9	652.4	.05	0.00	3.48	9.81	7.99	.170
.90-D-33	.898	190.6	563.5	651.9	.05	0.00	5.90	9.79	7.99	.170
.90-D-34	.898	191.0	564.2	652.9	.05	0.00	1.97	9.81	16.00	.339
.90-D-35	.901	192.0	565.2	654.1	.05	0.00	4.00	9.84	16.00	.338

[1]Codes are defined in section "Results and Discussion."

TABLE IV. Continued

M = 0.90

Code[1]	M	q, psf	T_o, R	p_t, psf	$\bar{\alpha}$, deg	α, deg	δ, deg	R	f, Hz	k
0.90-D-36	0.899	191.3	564.4	652.8	0.04	0	5.82	9.81×10^6	16.01	0.3400
.90-D-37	.901	188.5	553.0	641.5	.99	0	2.26	9.94	7.99	.1710
.90-D-38	.901	186.9	548.7	636.0	.99	0	4.40	9.97	8.00	.1710
.90-D-39	.903	187.7	548.0	636.8	.99	0	6.77	10.01	7.99	.1710
.90-D-40	.906	189.1	547.2	639.2	.99	0	2.23	10.07	16.00	.3420
.90-D-41	.902	187.9	548.8	637.9	.99	0	4.45	10.00	16.00	.3400
.90-D-42	.898	187.2	550.1	639.0	.99	0	6.70	9.98	15.99	.3440
.90-D-43	.900	188.0	548.8	640.1	.99	0	2.25	10.03	21.97	.4670
.90-D-44	.903	189.0	551.3	641.5	.99	0	4.44	10.02	21.99	.4700
.90-D-45	.904	189.9	549.3	643.3	.99	0	6.65	10.08	21.97	.4710
.90-D-46	.905	191.7	557.9	648.7	1.97	0	2.24	9.91	8.01	.1690
.90-D-47	.902	191.1	559.2	649.6	1.97	0	4.36	9.88	8.01	.1700
.90-D-48	.905	192.6	560.0	651.8	1.97	0	6.63	9.88	8.01	.1690
.90-D-49	.907	192.6	561.0	650.7	1.97	0	2.19	9.88	16.01	.3370
.90-D-50	.900	190.9	561.8	650.7	1.97	0	4.38	9.82	16.01	.3390
.90-D-51	.906	191.2	562.3	651.0	1.97	0	6.55	9.82	16.00	.3380
.90-D-52	.900	191.1	562.0	651.3	1.97	0	2.16	9.83	21.97	.4650
.90-D-53	.900	191.1	562.5	651.6	1.97	0	4.36	9.82	21.96	.4620
.90-D-54	.901	191.6	563.2	652.6	1.97	0	6.55	9.82	21.99	.4660
.90-D-55	.901	193.4	567.3	658.6	2.99	0	2.20	9.80	8.01	.1680
.90-D-56	.904	194.9	567.2	661.1	2.99	0	4.38	9.82	8.01	.1680
.90-D-57	.905	195.2	567.9	661.6	2.99	0	6.65	9.84	8.01	.1680
.90-D-58	.902	194.6	567.7	661.4	2.99	0	2.17	9.84	16.00	.3370
.90-D-59	.901	193.9	567.5	659.6	2.99	0	4.39	9.82	16.01	.3370
.90-D-60	.906	195.6	567.9	661.9	2.99	0	6.56	9.85	16.00	.3350
.90-D-61	.901	193.8	567.3	660.1	2.99	0	2.18	9.89	21.97	.4600
.90-D-62	.905	195.6	567.8	662.5	2.99	0	4.32	9.86	22.00	.4610
.90-D-63	.900	193.9	567.7	661.1	2.99	0	6.56	9.83	0.00	.4610

[1]Codes are defined in section "Results and Discussion."

TABLE IV. Continued

M = 0.92

Code[1]	M	q, psf	T_o, R	p_t, psf	$\bar{\alpha}$ deg	α deg	δ, deg	R	f, Hz	k
0.92-D-1	.922	199.7	558.1	662.5	.05	.25	0.00	10.21×10^6	3.98	.083
.92-D-2	.922	199.7	555.9	660.8	.05	.24	0.00	10.25	7.98	.166
.92-D-3	.921	198.3	555.3	657.7	.05	.23	0.00	10.25	16.01	.335
.92-D-4	.922	200.3	558.4	664.5	.05	.50	0.00	10.23	3.98	.083
.92-D-5	.921	198.5	556.1	659.2	.05	.47	0.00	10.21	7.97	.166
.92-D-6	.921	197.8	554.4	658.1	.05	.46	0.00	10.22	16.01	.335
.92-D-7	.921	201.4	559.7	669.1	1.04	.25	0.00	10.26	4.00	.083
.92-D-8	.925	202.3	560.7	669.1	1.04	.24	0.00	10.22	8.00	.165
.92-D-9	.921	201.0	561.1	667.7	1.03	.23	0.00	10.20	16.00	.333
.92-D-10	.921	201.4	561.1	671.1	1.04	.50	0.00	10.27	4.00	.083
.92-D-11	.921	201.4	561.2	669.1	1.04	.47	0.00	10.22	8.00	.166
.92-D-12	.919	200.8	560.4	668.3	1.04	.46	0.00	10.21	16.00	.332
.92-D-13	.921	202.8	563.4	673.6	1.88	.25	0.00	10.23	4.00	.083
.92-D-14	.925	203.9	561.6	673.9	1.89	.24	0.00	10.23	8.00	.165
.92-D-15	.924	203.4	563.2	673.1	2.02	.23	0.00	10.24	16.00	.332
.92-D-16	.923	203.3	561.3	673.6	1.89	.50	0.00	10.29	4.00	.083
.92-D-17	.923	204.7	563.3	675.6	1.88	.47	0.00	10.29	8.00	.166
.92-D-18	.923	203.1	561.6	673.1	1.96	.46	0.00	10.28	16.00	.331
.92-D-19	.925	205.6	562.6	679.6	3.03	.25	0.00	10.34	4.00	.082
.92-D-20	.923	204.9	564.7	679.2	3.03	.24	0.00	10.28	8.00	.166
.92-D-21	.919	203.3	564.2	677.1	3.03	.50	0.00	10.25	8.00	.165
.92-D-22	.923	204.8	562.6	678.9	3.03	.47	0.00	10.33	16.00	.331
.92-D-23	.921	204.4	562.5	679.0	4.01	.25	0.00	10.33	4.00	.083
.92-D-24	.921	204.1	564.3	678.6	4.01	.24	0.00	10.27	8.00	.165
.92-D-25	.924	205.4	564.4	680.1	4.01	.23	0.00	10.30	16.00	.330
.92-D-26	.923	205.4	562.7	680.5	4.00	.50	0.00	10.35	4.00	.083
.92-D-27	.921	204.2	565.0	678.5	4.01	.47	0.00	10.25	8.00	.165
.92-D-28	.920	203.9	563.7	678.2	3.99	.46	0.00	10.28	16.00	.332
.92-D-29	.925	196.2	545.1	647.8	.05	0.00	1.95	10.34	7.98	.167
.92-D-30	.927	197.4	547.3	650.2	.05	0.00	3.92	10.32	7.98	.167
.92-D-31	.920	195.2	545.6	648.4	.05	0.00	5.88	10.32	7.98	.168
.92-D-32	.920	195.7	547.9	650.0	.05	0.00	1.94	10.29	15.98	.336
.92-D-33	.923	197.2	548.0	652.8	.05	0.00	3.93	10.29	15.98	.337
.92-D-34	.923	197.5	549.9	653.9	.05	0.00	5.85	10.28	15.98	.335
.92-D-35	.919	196.1	551.1	652.4	.05	0.00	1.97	10.31	22.00	.460
.92-D-36	.924	197.6	551.8	653.9	.05	0.00	3.89	10.25	22.00	.459
.92-D-37	.924	197.9	552.3	654.7	.05	0.00	5.83	10.33	21.99	.460
.92-D-38	.925	201.5	559.7	666.2	1.04	0.00	1.97	10.23	8.01	.166
.92-D-39	.924	201.4	560.5	666.6	1.04	0.00	3.92	10.21	8.01	.166
.92-D-40	.924	201.8	559.9	667.6	1.04	0.00	5.91	10.24	8.00	.166
.92-D-41	.925	202.2	559.6	668.6	1.04	0.00	1.97	10.27	16.01	.332
.92-D-42	.923	201.3	560.3	667.3	1.04	0.00	3.89	10.22	16.01	.332
.92-D-43	.924	202.2	559.6	669.1	1.04	0.00	5.85	10.27	16.01	.332
.92-D-44	.924	202.2	560.3	669.1	1.04	0.00	1.94	10.24	21.99	.458
.92-D-45	.921	201.2	558.9	668.3	1.04	0.00	3.85	10.27	21.99	.457
.92-D-46	.921	201.0	561.2	667.9	1.04	0.00	5.82	10.20	21.97	.475
.92-D-47	.920	201.6	560.2	670.8	2.02	0.00	1.96	10.27	7.97	.165
.92-D-48	.920	201.7	561.2	670.9	2.02	0.00	3.89	10.25	7.97	.165
.92-D-49	.923	202.6	562.5	671.5	2.02	0.00	5.84	10.27	7.97	.165
.92-D-50	.921	202.1	562.4	671.6	2.02	0.00	2.00	10.23	16.00	.332

[1]Codes are defined in section "Results and Discussion."

TABLE IV. Continued

M = 0.92

Code[1]	M	q, psf	T_o, R	p_t, psf	$\bar{\alpha}$, deg	α, deg	δ, deg	R	f, Hz	k
0.92-D-51	0.924	203.4	563.0	673.4	2.02	0	3.90	10.25×10^6	15.99	0.3320
.92-D-52	.924	203.7	561.5	673.9	2.02	0	5.84	10.30	16.01	.3320
.92-D-53	.920	201.9	562.4	671.8	2.02	0	1.92	10.23	21.99	.4560
.92-D-54	.926	204.1	563.0	674.2	2.02	0	3.85	10.27	21.99	.4540
.92-D-55	.927	204.7	562.9	674.7	2.02	0	5.78	10.30	8.00	.454
.92-D-56	.918	202.6	562.5	675.6	3.04	0	3.91	10.27	8.00	.1660
.92-D-57	.919	203.2	564.9	676.7	3.04	0	6.00	10.26	8.00	.1660
.92-D-58	.919	203.5	563.0	677.9	3.04	0	3.90	10.27	16.00	.3320
.92-D-59	.924	205.1	564.8	678.9	3.04	0	5.85	10.27	16.00	.3320
.92-D-60	.921	203.6	561.9	676.4	3.04	0	1.96	10.30	21.96	.4540
.92-D-61	.921	203.7	561.9	676.8	3.04	0	3.88	10.31	21.97	.4550
.92-D-62	.921	203.9	563.5	677.1	3.04	0	5.81	10.27	21.96	.4550

[1]Codes are defined in section "Results and Discussion."

TABLE IV. Continued

M = 0.94

Code[1]	M	q, psf	T_o, R	p_t, psf	$\bar{\alpha}$, deg	α, deg	δ, deg	R	f, Hz	k
0.94-D-1	.946	204.7	563.8	660.5	.05	.26	0.00	10.07×10^6	3.99	.081
.94-D-2	.943	203.4	563.9	658.8	.05	.23	0.00	10.03	7.99	.162
.94-D-3	.947	204.8	562.0	660.1	.05	.23	0.00	10.11	16.01	.324
.94-D-4	.947	204.8	564.2	660.8	.05	.46	0.00	10.04	3.99	.081
.94-D-5	.945	203.9	563.3	658.8	.05	.47	0.00	10.06	7.98	.162
.94-D-6	.942	203.2	562.1	658.4	.05	.46	0.00	10.07	16.03	.326
.94-D-7	.940	199.8	562.1	651.8	.97	0.00	0.00	9.96	3.96	.081
.94-D-8	.942	201.7	559.6	653.3	.97	0.00	0.00	10.06	7.98	.161
.94-D-9	.944	201.5	559.9	652.0	.97	0.00	0.00	10.04	16.01	.324
.94-D-10	.942	200.0	561.8	653.2	.97	.50	0.00	10.04	3.96	.080
.94-D-11	.942	201.0	559.5	651.9	.97	.46	0.00	10.04	7.99	.162
.94-D-12	.944	201.5	561.8	652.0	.97	.46	0.00	10.04	16.00	.324
.94-D-13	.943	199.1	555.6	644.4	2.01	.25	0.00	10.03	4.00	.324
.94-D-14	.950	200.9	553.0	645.1	2.01	.23	0.00	10.13	7.96	.162
.94-D-15	.945	198.6	551.8	641.3	2.01	.23	0.00	10.09	16.00	.328
.94-D-16	.943	199.0	555.7	644.0	2.00	.50	0.00	10.03	4.00	.082
.94-D-17	.946	200.0	555.5	644.6	2.00	.46	0.00	10.05	7.96	.162
.94-D-18	.942	197.6	553.3	640.5	2.00	.47	0.00	10.03	15.98	.328
.94-D-19	.949	203.8	561.8	655.7	3.05	.24	0.00	10.08	4.00	.081
.94-D-20	.940	201.0	561.8	652.8	3.05	.24	0.00	9.99	7.98	.162
.94-D-21	.944	201.5	559.7	652.0	3.05	.23	0.00	10.04	15.99	.325
.94-D-22	.943	202.1	562.0	654.2	3.05	.46	0.00	10.02	7.99	.162
.94-D-23	.944	202.1	560.3	653.9	3.05	.46	0.00	10.06	16.00	.325
.94-D-24	.942	202.3	563.1	656.3	4.03	.24	0.00	10.01	3.99	.081
.94-D-25	.943	202.7	563.3	656.6	4.03	.24	0.00	10.02	7.95	.161
.94-D-26	.939	201.7	562.0	656.2	4.03	.24	0.00	10.04	16.00	.324
.94-D-27	.947	204.1	563.0	658.3	4.03	.47	0.00	10.06	3.99	.031
.94-D-28	.944	203.4	563.6	658.2	4.03	.47	0.00	10.04	7.95	.161
.94-D-29	.941	202.1	563.5	656.0	4.03	.46	0.00	10.06	15.98	.323
.94-D-30	.939	201.9	561.8	657.2	.05	0.00	1.97	10.05	7.99	.162
.94-D-31	.946	204.1	563.8	659.2	.05	0.00	3.90	10.03	7.99	.162
.94-D-32	.944	203.4	562.9	658.5	.05	0.00	5.83	10.06	7.99	.161
.94-D-33	.939	202.0	563.0	657.2	.05	0.00	1.98	10.02	15.98	.323
.94-D-34	.942	203.4	561.3	659.1	.05	0.00	3.96	10.06	15.98	.326
.94-D-35	.947	204.2	563.7	658.5	.05	0.00	5.95	10.04	15.98	.323
.94-D-36	.940	202.4	563.4	657.5	.05	0.00	1.97	10.02	21.95	.444
.94-D-37	.942	203.5	563.2	659.5	.05	0.00	3.99	10.06	21.95	.444
.94-D-38	.944	203.5	563.7	658.2	.05	0.00	5.83	10.03	21.97	.444
.94-D-39	.942	200.3	560.0	649.0	.97	0.00	1.98	10.04	7.99	.162
.94-D-40	.943	200.6	560.3	649.5	.97	0.00	3.90	9.99	7.99	.163
.94-D-41	.945	201.6	560.5	651.4	.97	0.00	5.90	10.02	7.99	.163
.94-D-42	.941	200.0	560.1	649.0	.97	0.00	1.92	9.98	16.00	.323
.94-D-43	.940	200.0	560.2	649.5	.97	0.00	3.91	9.98	16.00	.326
.94-D-44	.944	201.5	560.6	651.8	.97	0.00	5.85	10.04	16.00	.325
.94-D-45	.945	202.0	558.9	652.7	.97	0.00	1.95	10.08	21.97	.445
.94-D-46	.942	200.0	561.2	650.2	.97	0.00	3.89	9.97	21.97	.448
.94-D-47	.943	201.4	559.8	652.2	.97	0.00	5.85	9.98	21.97	.447
.94-D-48	.948	204.3	564.1	657.7	1.96	0.00	2.00	10.03	7.96	.161

[1]Codes are defined in section "Results and Discussion."

TABLE IV. Continued

M = 0.94

Code[1]	M	q, psf	T_o, R	p_t, psf	$\bar{\alpha}$, deg	α, deg	δ, deg	R	f, Hz	k
0.94-D-49	0.942	202.3	563.8	656.2	1.96	0	3.90	9.99×10^6	7.96	0.1620
.94-D-50	.944	203.4	564.2	658.1	1.96	0	5.88	10.02	7.96	.1620
.94-D-51	.941	202.2	563.7	656.2	1.96	0	1.99	10.00	16.00	.3240
.94-D-52	.940	196.9	552.2	639.3	2.01	0	5.81	10.09	16.03	.3280
.94-D-53	.940	199.0	*****	*****	2.01	0	1.97	*****	21.97	.4460
.94-D-54	.940	197.1	*****	*****	2.00	0	3.87	*****	21.97	.4510
.94-D-55	.942	197.0	548.5	637.7	2.01	0	5.85	10.11	21.95	.4490
.94-D-56	.942	200.4	560.1	649.8	3.05	0	1.96	9.99	7.99	.1620
.94-D-57	.945	201.3	560.9	650.4	3.05	0	3.91	9.99	7.99	.1630
.94-D-58	.943	200.8	560.3	650.3	3.05	0	5.87	10.00	7.98	.1620
.94-D-59	.941	200.6	560.7	650.8	3.05	0	1.95	9.99	16.00	.3250
.94-D-60	.940	200.2	558.6	650.3	3.05	0	3.86	10.04	15.99	.325
.94-D-61	.942	200.9	559.0	651.2	3.05	0	5.74	10.05	16.00	.324
.94-D-62	.945	202.0	559.5	652.8	3.05	0	1.96	10.06	21.96	.446
.94-D-63	.945	202.1	561.1	652.8	3.05	0	3.86	10.02	21.96	.446
.94-D-64	.945	202.3	561.8	653.8	3.05	0	5.83	10.03	21.96	.444

[1]Codes are defined in section "Results and Discussion."

TABLE IV. Concluded

M = 0.96

Code[1]	M	q, psf	T_0, R	p_t, psf	$\bar{\alpha}$, deg	α, deg	δ, deg	R	f, Hz	k
0.96-D-1	0.961	207.3	563.2	658.0	0.04	0.25	0.00	10.03 x 10^6	8.01	0.1590
.96-D-2	.963	207.0	561.1	655.9	.04	.25	0.00	10.06	16.01	.3180
.96-D-3	.960	207.4	565.1	659.7	.04	.50	0.00	10.04	3.99	.0790
.96-D-4	.961	207.2	564.8	658.1	.04	.50	0.00	10.10	7.99	.1580
.96-D-5	.959	206.3	560.8	656.4	.04	.50	0.00	10.10	16.01	.3190
.96-D-6	.961	200.4	568.0	636.7	.05	0.00	2.26	9.61	7.99	.1580
.96-D-7	.962	201.0	568.7	637.8	.05	0.00	4.48	9.61	8.00	.1580
.96-D-8	.963	201.5	568.4	638.6	.05	0.00	6.83	9.63	7.99	.1580
.96-D-9	.962	201.4	568.7	639.0	.05	0.00	2.25	9.63	16.00	.3150
.96-D-10	.960	200.6	569.3	638.1	.05	0.00	4.54	9.59	16.00	.3150
.96-D-11	.964	202.3	569.2	640.3	.05	0.00	6.92	9.64	16.00	.3150
.96-D-12	.962	203.4	552.0	649.9	.05	0.00	2.13	10.17	22.00	.4410
.96-D-13	.964	204.7	551.9	647.6	.05	0.00	4.38	10.16	22.03	.4420
.96-D-14	.961	203.9	554.1	647.2	.05	0.00	6.65	10.14	22.01	.441

M = 1.12

Code[1]	M	q, psf	T_0, R	p_t, psf	$\bar{\alpha}$, deg	α, deg	δ, deg	R	f, Hz	k
1.12-D-1	1.120	233.6	576.1	648.3	0	0.25	0.00	9.69 x 10^6	3.98	0.0680
1.12-D-2	1.120	232.4	572.9	645.8	0	.24	0.00	9.73	8.00	.1360
1.12-D-3	1.120	233.5	575.4	647.6	0	.23	0.00	9.69	16.01	.2730
1.12-D-4	1.120	232.4	573.4	646.6	0	.50	0.00	9.73	3.98	.0680
1.12-D-5	1.120	232.4	575.4	646.1	0	.47	0.00	9.67	8.00	.1360
1.12-D-6	1.120	232.5	575.6	646.3	0	.47	0.00	9.68	16.01	.2720
1.12-D-7	1.120	232.1	571.0	643.8	0	0.00	2.26	9.65	7.95	.1350
1.12-D-8	1.120	231.6	573.1	643.2	0	0.00	4.50	9.69	7.95	.1360
1.12-D-9	1.120	231.8	573.5	643.7	0	0.00	6.83	9.68	7.95	.1360
1.12-D-1	1.120	232.3	571.6	644.8	0	0.00	2.20	9.67	16.00	.2730
1.12-D-1	1.120	231.7	572.5	643.8	0	0.00	4.37	9.76	16.01	.2730
1.12-D-12	1.120	232.9	571.6	645.9	0	0.00	6.62	9.76	16.00	.2720
1.12-D-13	1.120	232.1	574.5	644.8	0	0.00	2.23	9.68	21.99	.3740
1.12-D-14	1.120	232.8	575.0	646.1	0	0.00	4.43	9.68	21.99	.3750
1.12-D-15	1.120	232.0	574.6	644.7	0	0.00	6.64	9.67	21.99	.323

[1]Codes are defined in section "Results and Discussion."

TABLE V. SAMPLE UNSTEADY DATA SET

.40-D-16	MACH	Q PSF	TO R	H PSF	ALPHA BAR DEG.	ALPHA DEG.	DELTA DEG.	RN *10**6	FREQ. HZ.	K
	.403	78.3	527.5	929.8	3.04	.46	0.00	9.22	7.99	.3830

CHRD NO.*	LOC NO.	CPU	PHAS U	CPL	PHAS L	DEL CP	D PHAS
1	1	.0333	119.70	.0212	175.30	.0485	-39.21
1	2	.0133	-151.90	.0038	-151.20	.0171	28.25
1	3	.0173	-156.80	.0183	-167.30	.0354	17.79
1	4	.0171	-153.00	.0171	-160.50	.0341	23.25
1	5	.0166	-148.50	.0164	-155.10	.0330	28.22
1	6	.0198	-144.50	.0195	-150.50	.0393	32.53
1	7	.0157	-133.90	.0155	-137.90	.0312	44.11
1	8	.0136	-123.80	.0137	-129.60	.0273	53.30
1	9	.0136	-119.60	.0138	-123.20	.0274	58.59
1	10	.0122	-119.60	.0130	-123.00	.0251	58.64
1	11	.0123	-115.70	.0121	-122.10	.0244	61.13
1	12	.0092	-105.40	.0096	-109.70	.0189	72.40
1	13	.0078	-94.89	.0077	-100.30	.0155	82.42
1	14	.0055	-86.98	.0058	-94.06	.0113	89.37
1	15	.0026	-76.24	.0028	-88.94	.0054	97.16
2	1	.0512	27.05	.0256	179.90	.0507	-130.66
2	2	.0119	-99.23	.0030	-121.60	.0147	76.25
2	3	.0181	-158.50	.0173	-159.70	.0354	20.91
2	4	.0170	-154.90	.0162	-158.90	.0332	23.14
2	5	.0166	-147.50	.0113	-150.90	.0279	31.12
2	6	.0176	-136.50	.0173	-141.50	.0348	41.02
2	7	.0157	-134.50	.0000	-22.87	.0157	45.50
2	8	.0126	-128.30	.0124	-132.00	.0249	49.87
2	9	.0152	-119.90	.0108	-121.70	.0240	59.29
2	10	.0130	-116.70	.0118	-122.90	.0248	60.34
2	11	.0110	-114.20	.0098	-122.00	.0208	62.13
2	12	.0068	-110.70	.0084	-114.60	.0152	67.14
2	13	.0008	143.90	.0055	-109.80	.0053	61.38
3	1	.0418	-99.31	.0221	-177.90	.0510	55.59
3	2	.0341	-179.70	.0014	82.04	.0340	-2.12
3	3	.0247	-169.30	.0194	-164.80	.0440	12.68

TABLE V. Concluded

.40-D-16	MACH	Q PSF	TO R	H PSF	ALPHA BAR DEG.	ALPHA DEG.	DELTA DEG.	RN *10**6
	.403	78.3	527.5	929.8	3.04	.46	0.00	9.22

CHRD NO.*	LOC NO.	CPU	PHAS U	CPL	PHAS L	DEL CP	D PHAS
3	4	.0069	-146.60	.0039	-125.60	.0107	41.02
3	5	.0056	-119.40	.0057	-113.70	.0113	63.47
3	6	.0039	-138.80	.0051	-103.80	.0086	60.98
3	7	.0036	119.30	.0020	-64.17	.0015	-56.07
4	1	.0330	14.16	.0002	-55.68	.0330	-166.12
4	2	.0696	177.50	.0069	129.20	.0744	-6.46
4	3	.0285	-171.20	.0188	-165.80	.0472	10.94
4	4	.0272	-167.90	.0187	-161.60	.0459	14.67
4	5	.0217	-161.80	.0170	-157.50	.0386	20.09
4	6	.0221	-157.60	.0187	-154.50	.0409	23.82
4	7	.0166	-146.80	.0146	-146.30	.0313	33.43
4	8	.0149	-139.40	.0136	-142.40	.0286	39.17
4	9	.0126	-139.10	.0120	-139.10	.0246	40.90
4	10	.0118	-132.20	.0110	-134.00	.0228	46.93
4	11	.0104	-125.70	.0097	-130.70	.0201	51.89
4	12	.0096	-120.00	.0091	-129.50	.0186	55.39
4	13	.0089	-132.30	.0063	-123.10	.0131	52.06
4	14	.0066	-111.20	.0065	-116.80	.0131	66.03
4	15	.0051	-117.70	.0046	-107.70	.0097	67.03
4	16	.0025	-114.60	.0000	-178.70	.0025	65.40
5	1	.0082	-48.89	.0217	-166.80	.0193	35.32
5	2	.0143	-47.60	.0192	-163.90	.0182	60.83
5	3	.0128	-60.44	.0178	-162.40	.0197	57.03
5	4	.0096	-68.34	.0174	-160.40	.0223	43.77
5	5	.0097	-109.90	.0133	-152.90	.0215	45.10
5	6	.0085	-115.00	.0098	-145.60	.0177	48.62
5	7	.0095	-111.50	.0086	-139.60	.0175	55.12
5	8	.0064	-113.40	.0077	-136.20	.0138	54.16
5	9	.0070	-117.30	.0058	-128.30	.0128	57.72
5	10	.0003	18.72	.0000	157.10	.0003	-161.20

*Chords A through E in text are 1 through 5, respectively, in this table, microfiche, and digital tapes.

TABLE VI. SUMMARY OF STEADY PRESSURE FIGURES

[Nominal conditions]

Figure	M	$\bar{\alpha}$, deg	$\bar{\delta}$, deg	Comments
9	*	3	0	ΔC_p, comparison with linear theory
10	*	0.05	6	ΔC_p, comparison with linear theory
11	0.92	2	0	$C_{p,u}$, surface pressure distribution
12	.90	*	0	ΔC_p, comparison with small-disturbance theory
13	.90	2	*	ΔC_p, comparison with small-disturbance theory
14	*	0	0	$C_{p,u}$
15	.40	*	0	$C_{p,u}$
16	.88	*	0	$C_{p,u}$
17	.90	*	0	$C_{p,u}$
18	.92	*	0	$C_{p,u}$
19(a)	.94	*	0	$C_{p,u}$
19(b)	.94	*	0	ΔC_p
20(a)	*	1	6	$C_{p,u}$
20(b)	*	1	0	$C_{p,u}$
20(c)	*	1	-6	$C_{p,u}$
20(d)	*	1	6	ΔC_p
20(e)	*	1	0	ΔC_p
20(f)	*	1	-6	ΔC_p
21(a)	*	3	6	$C_{p,u}$
21(b)	*	3	0	$C_{p,u}$
21(c)	*	3	-6	$C_{p,u}$
21(d)	*	3	6	ΔC_p
21(e)	*	3	0	ΔC_p
21(f)	*	3	-6	ΔC_p
22(a)	.88	3	*	ΔC_p
22(b)	.90	3	*	ΔC_p
22(c)	.92	3	*	ΔC_p
22(d)	.94	3	*	ΔC_p
23(a)	.88	3	*	ΔC_p
23(b)	.90	3	*	ΔC_p
23(c)	.92	3	*	ΔC_p
23(d)	.94	3	*	ΔC_p
24(a)	.88	*	*	C_h
24(b)	.90	*	*	C_h
24(c)	.92	*	*	C_h
24(d)	.94	*	*	C_h

*Parameter varied.

TABLE VII. SUMMARY OF UNSTEADY PRESSURE FIGURES

[Nominal conditions]

Figure	M	$\bar{\alpha}$, deg	α, deg	δ, deg	f, Hz	Comments
25(a)	0.40	0.05	0.47	0	4	$\lvert C_{p,u}\rvert$, comparison with linear theory, chord D
25(b)	.40	.05	.47	0	8	$\lvert C_{p,u}\rvert$, comparison with linear theory, chord D
25(c)	.40	.05	.47	0	16	$\lvert C_{p,u}\rvert$, comparison with linear theory, chord D
26	.885	.05	.48	0	8	$\lvert C_{p,u}\rvert$, comparison with linear theory, chord D
27(a)	.90	0	.46	0	8	$\lvert C_{p,u}\rvert$, comparison with linear theory, chord D
27(b)	.90	0	.46	0	16	$\lvert C_{p,u}\rvert$, comparison with linear theory, chord D
28(a)	.40	*	.46	0	4	$\lvert C_{p,u}\rvert$/deg, $\lvert \Delta C_p\rvert$/deg, chord D
28(b)	.40	3	.46	0	*	$\lvert C_{p,u}\rvert$/deg, $\lvert \Delta C_p\rvert$/deg, chord D
29(a)	.90	*	.46	0	4	$\lvert C_{p,u}\rvert$/deg, $\lvert \Delta C_p\rvert$/deg, chord D
29(b)	.90	*	.46	0	16	$\lvert C_{p,u}\rvert$/deg, $\lvert \Delta C_p\rvert$/deg, chord D
30	.90	3	.46	0	*	$\lvert C_{p,u}\rvert$/deg, $\lvert \Delta C_p\rvert$/deg, chord D
31	.90	3	*	0	8	$\lvert C_{p,u}\rvert$/deg, $\lvert \Delta C_p\rvert$/deg, chord D
32(a)	*	3	.46	0	4	$\lvert C_{p,u}\rvert$/deg, $\lvert \Delta C_p\rvert$/deg, chord D
32(b)	*	3	.50	0	16	$\lvert C_{p,u}\rvert$/deg, $\lvert \Delta C_p\rvert$/deg, chord D
33(a)	*	3	.50	0	16	$\lvert C_{p,u}\rvert$/deg, chords A, B, C, D, and E
33(b)	*	3	.50	0	16	$\phi(C_{p,u})$, chords A, B, C, D, and E
33(c)	*	3	.50	0	16	$\lvert \Delta C_p\rvert$/deg, chords A, B, C, D, and E
33(d)	*	3	.50	0	16	$\phi(\Delta C_p)$, chords A, B, C, D, and E
34(a)	.40	.05	0	5.9	8	$\lvert C_{p,u}\rvert$, comparison with linear theory
34(b)	.40	.05	0	5.8	16	$\lvert C_{p,u}\rvert$, comparison with linear theory
35	.88	.05	0	5.9	8	$\lvert C_{p,u}\rvert$, comparison with linear theory
36(a)	.90	.05	0	2	8	$\lvert C_{p,u}\rvert$, comparison with linear theory
36(b)	.90	.05	0	3.5	8	$\lvert C_{p,u}\rvert$, comparison with linear theory
36(c)	.90	.05	0	5.9	8	$\lvert C_{p,u}\rvert$, comparison with linear theory
37(a)	*	1	0	6	8	$\lvert C_{p,u}\rvert$/deg, $\lvert \Delta C_p\rvert$/deg, chord D
37(b)	*	1	0	6	22	$\lvert C_{p,u}\rvert$/deg, $\lvert \Delta C_p\rvert$/deg, chord D
38	*	3	0	6	8	$\lvert C_{p,u}\rvert$/deg, $\lvert \Delta C_p\rvert$/deg, chord D
39(a)	.90	3	0	6	*	$\lvert C_{p,u}\rvert$/deg, $\lvert \Delta C_p\rvert$/deg, chord D
39(b)	.92	3	0	6	*	$\lvert C_{p,u}\rvert$/deg, $\lvert \Delta C_p\rvert$/deg, chord D
39(c)	.94	3	0	6	*	$\lvert C_{p,u}\rvert$/deg, $\lvert \Delta C_p\rvert$/deg, chord D
40(a)	.90	3	0	*	16	$\lvert C_{p,u}\rvert$/deg, $\lvert \Delta C_p\rvert$/deg, chord D
40(b)	.92	3	0	*	16	$\lvert C_{p,u}\rvert$/deg, $\lvert \Delta C_p\rvert$/deg, chord D
40(c)	.94	3	0	*	16	$\lvert C_{p,u}\rvert$/deg, $\lvert \Delta C_p\rvert$/deg, chord D
41(a)	.90	3	0	*	*	$\lvert C_{p,u}\rvert$/deg, chords A, B, C, D, and E
41(b)	.90	3	0	*	*	$\phi(C_{p,u})$, chords A, B, C, D, and E
41(c)	.90	3	0	*	*	$\lvert \Delta C_p\rvert$/deg, chords A, B, C, D, and E
41(d)	.90	3	0	*	*	$\phi(\Delta C_p)$, chords A, B, C, D, and E

*Parameter varied.

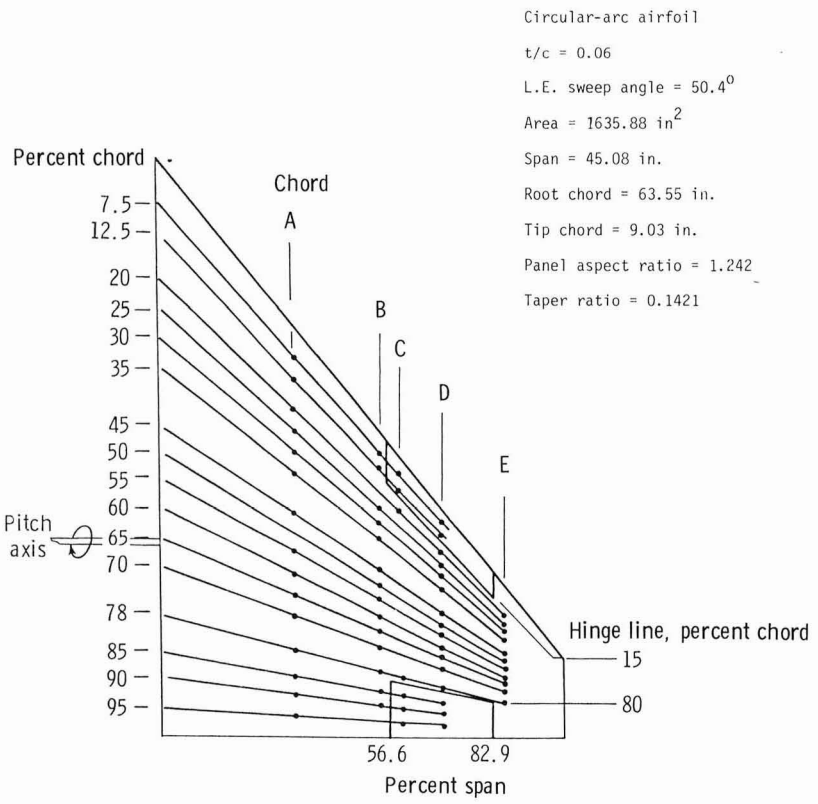

Figure 1. Planform geometry of clipped delta wing.

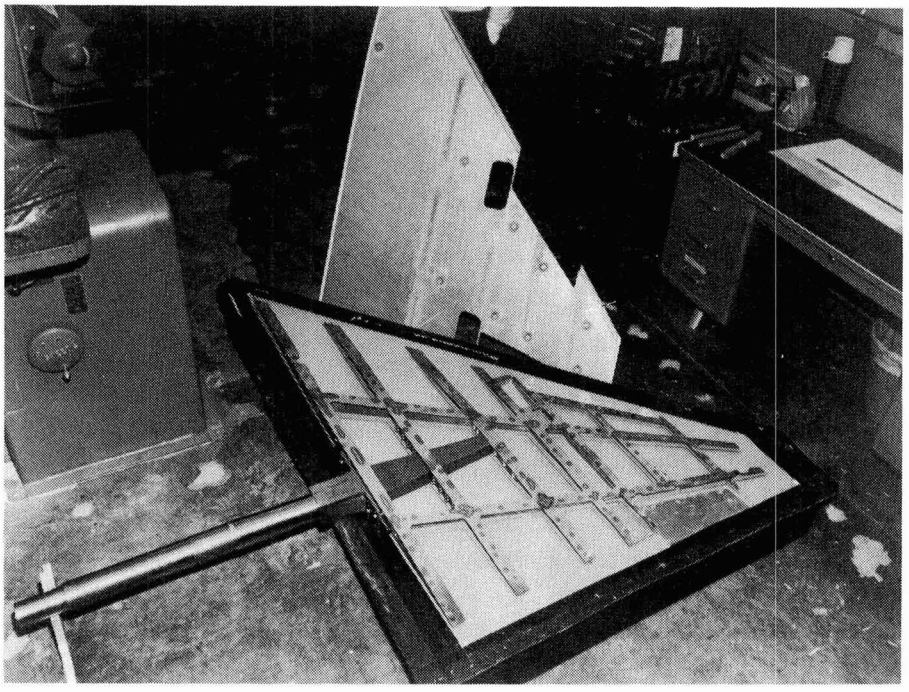

L-86-320

Figure 2. Construction of clipped delta wing.

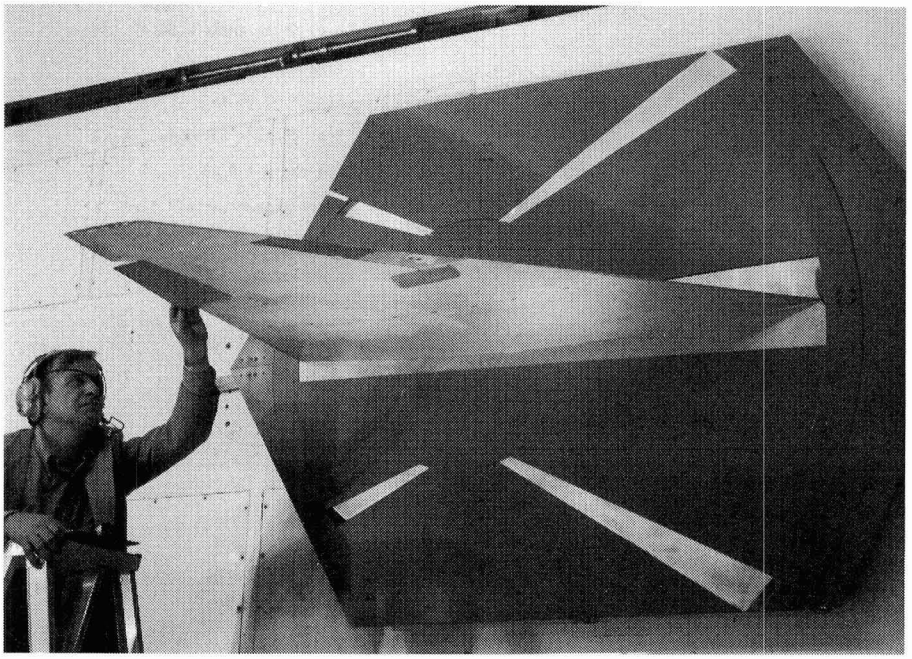

L-76-864

(a) Installed in Transonic Dynamics Tunnel.

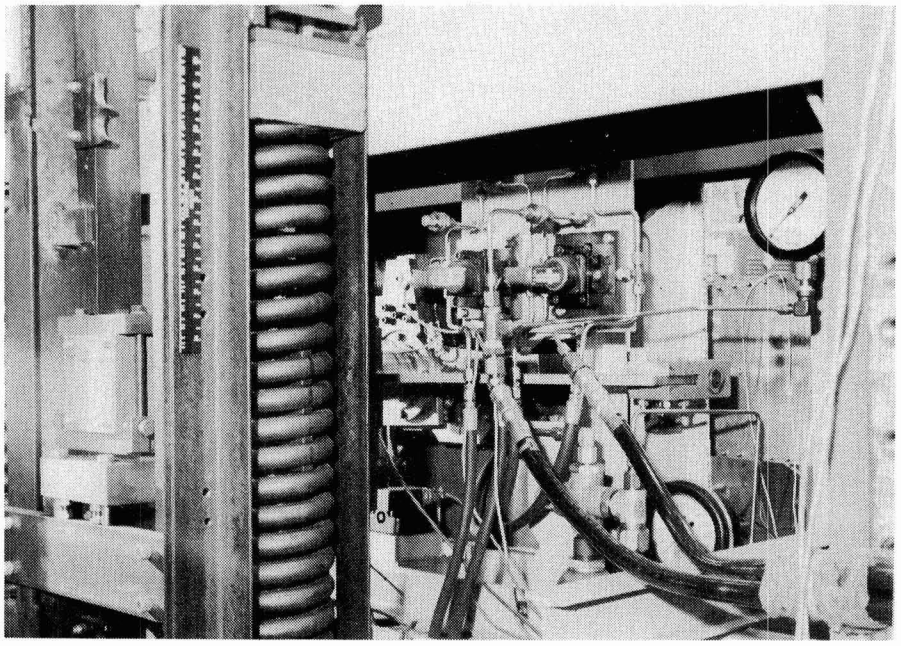

L-82-1664

(b) Oscillating mechanism.

Figure 3. Clipped delta wing.

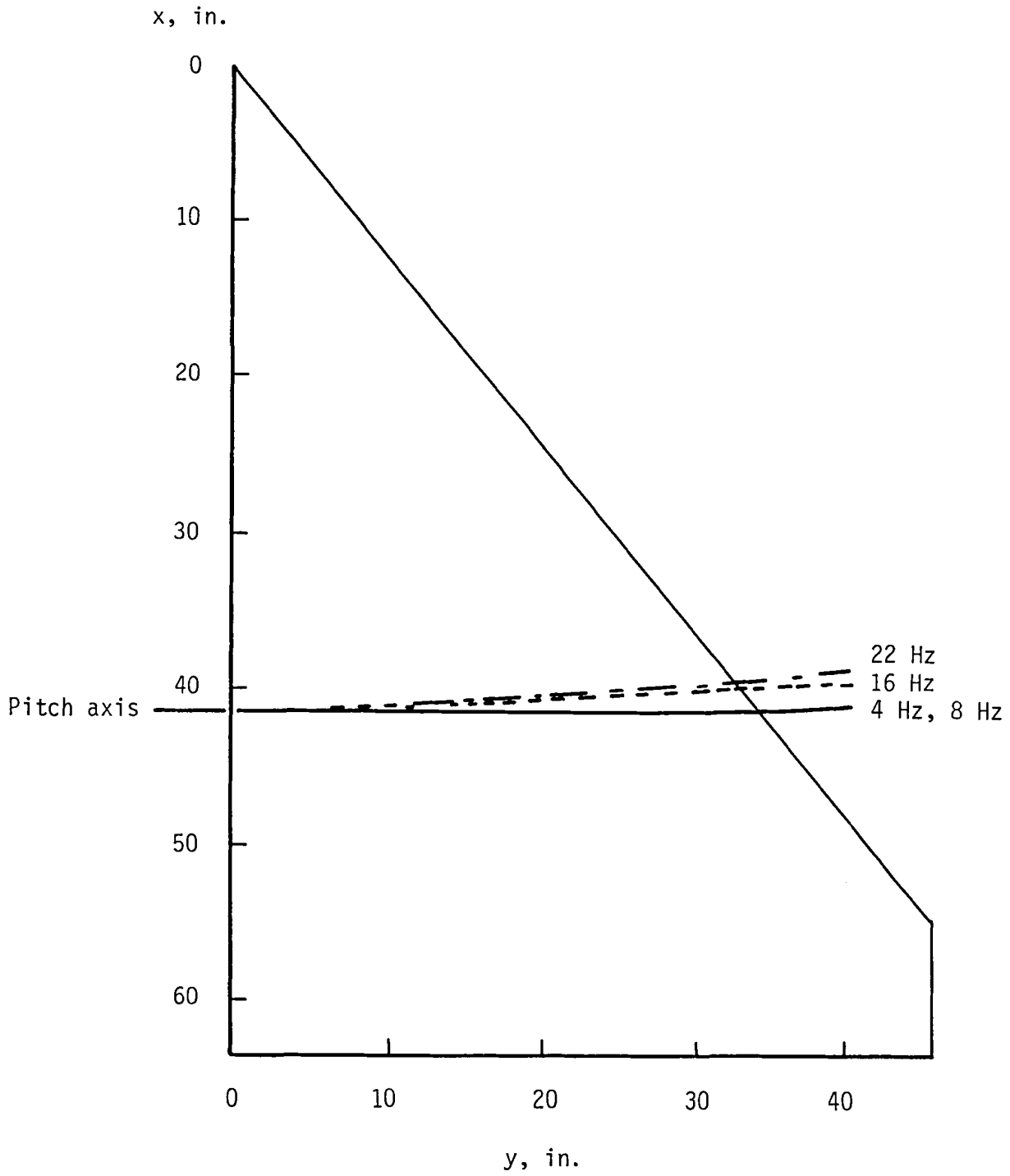

Figure 4. Node lines for test frequencies in still air.

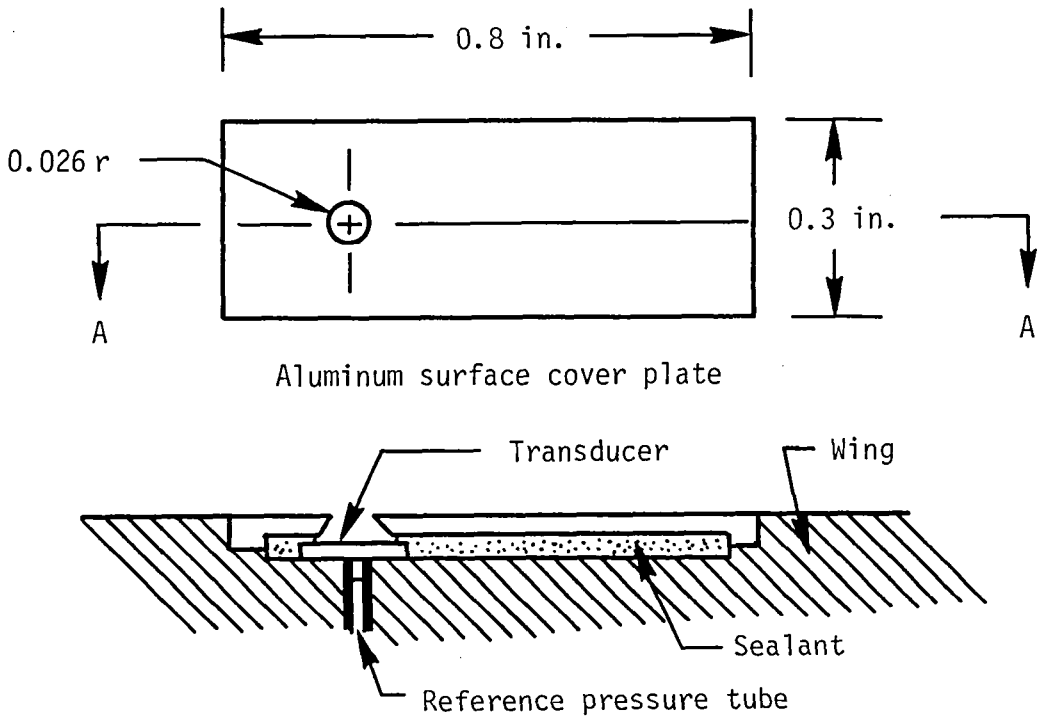

(a) Cover-plate-mounted transducer.

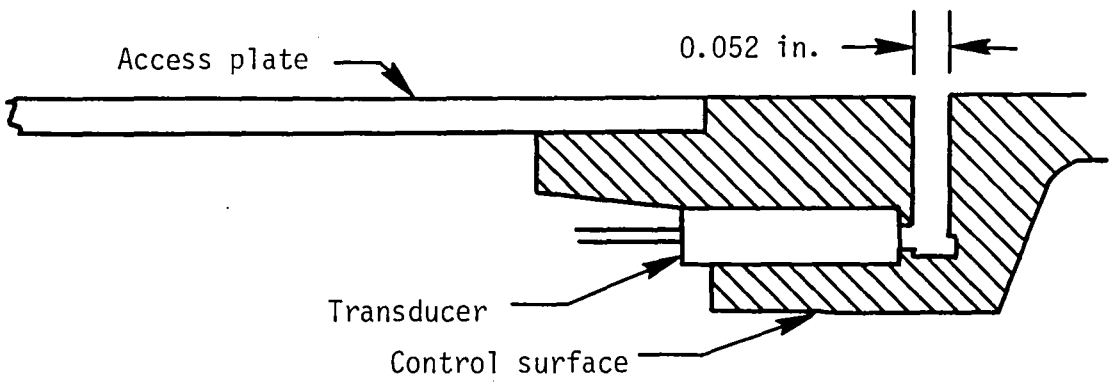

(b) Schematic of installation in control surface.

Figure 5. Transducer mounting configurations in delta-wing model.

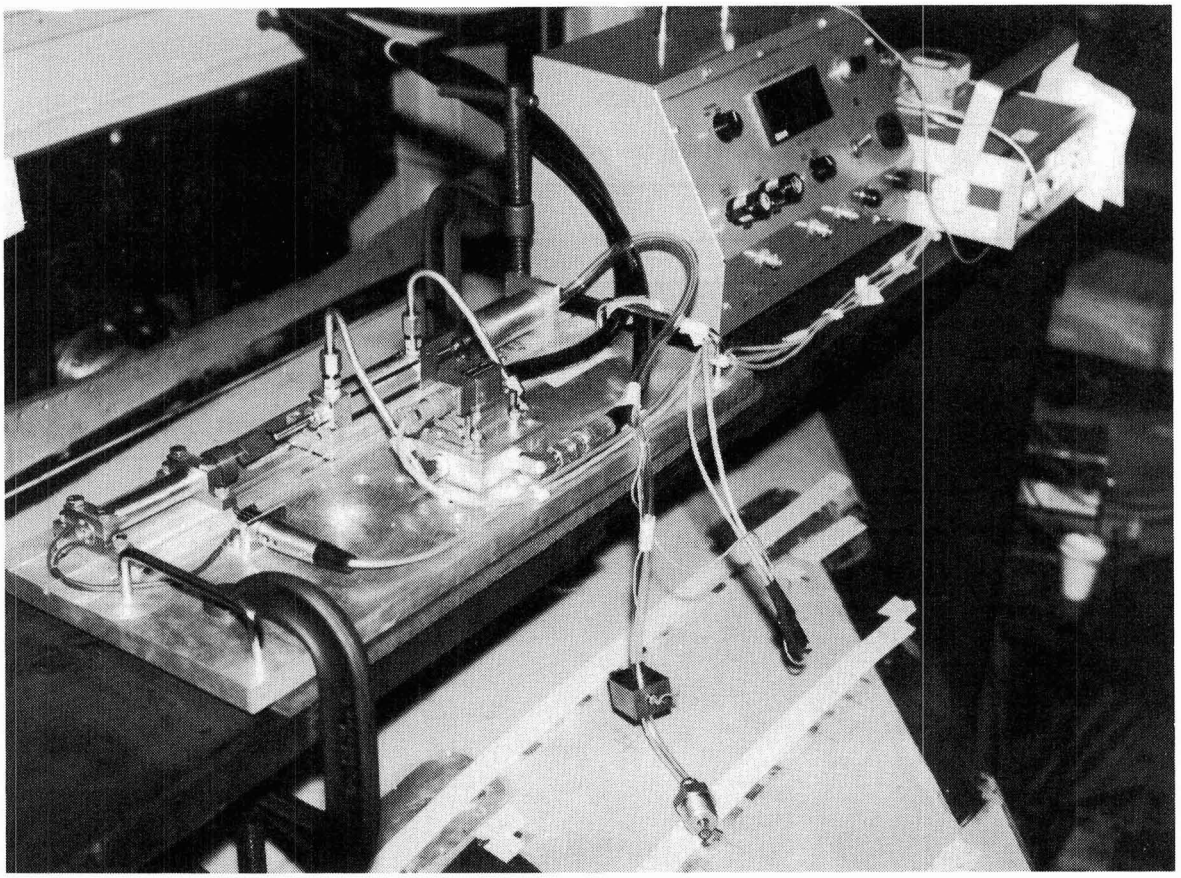

L-82-8945

Figure 6. Device for calibrating in situ pressure transducers.

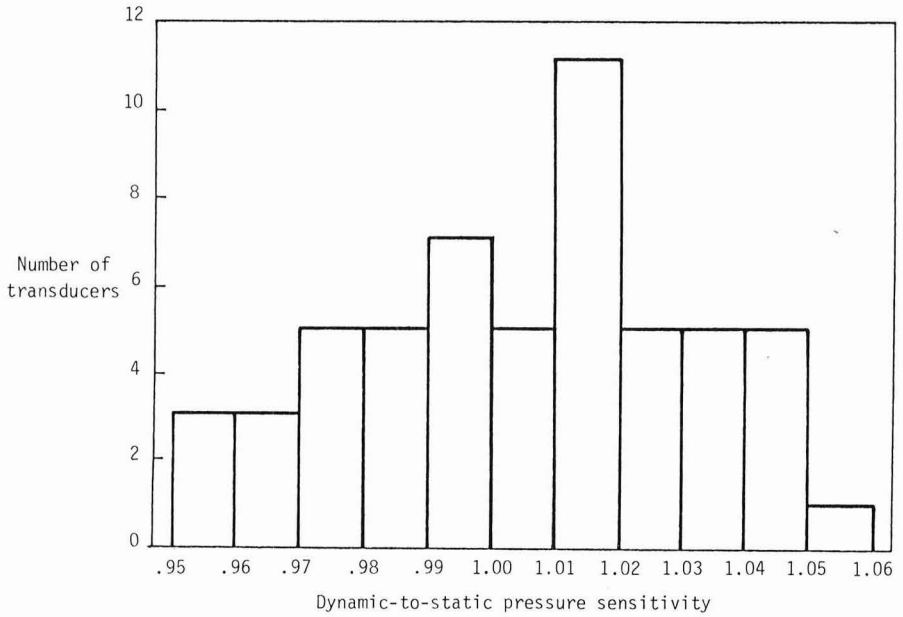

Figure 7. Distribution of dynamic-to-static pressure sensitivity ratios.

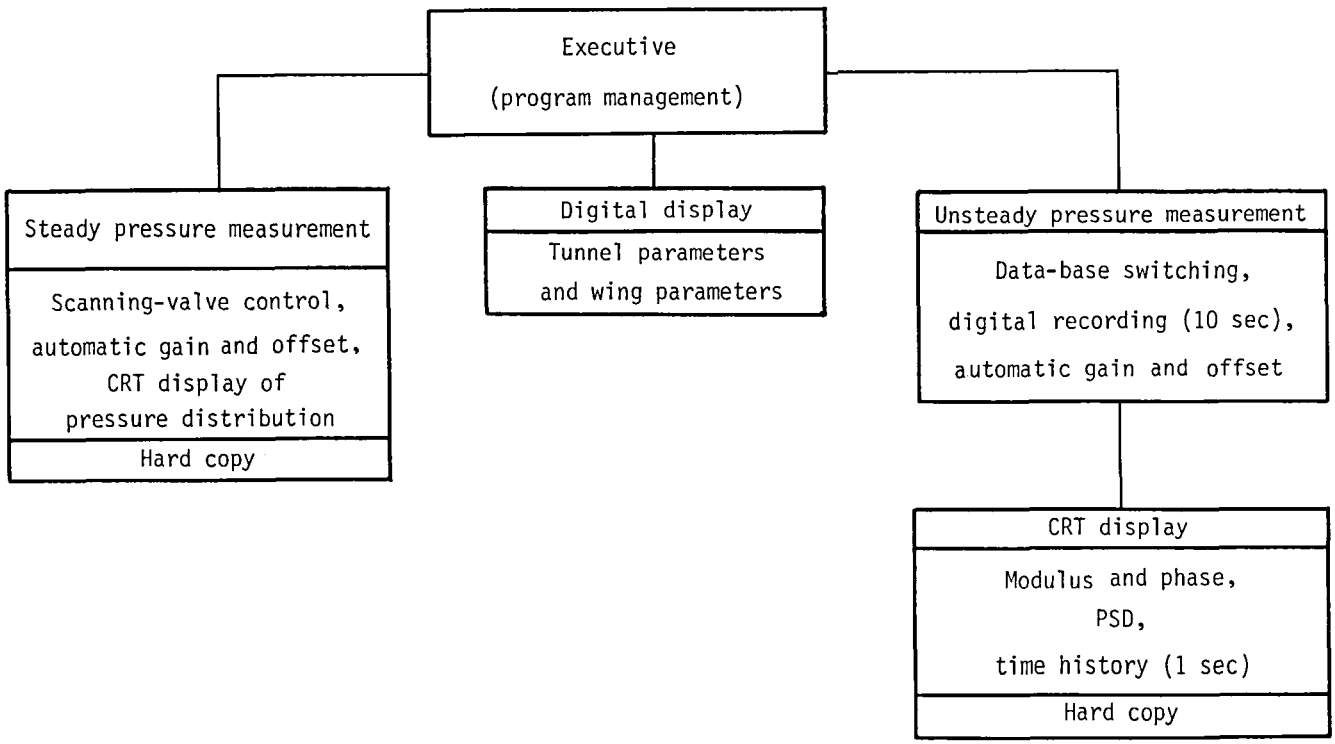

(a) On-line.

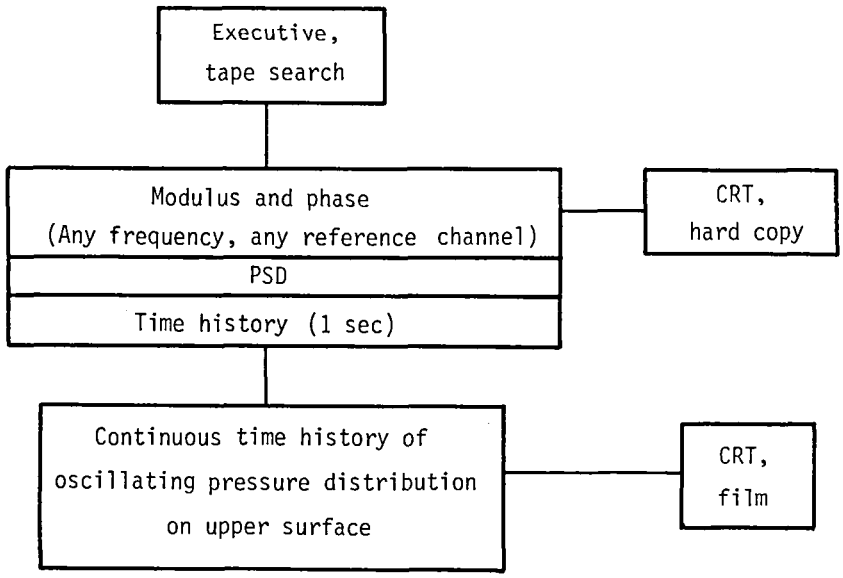

(b) Off-line.

Figure 8. Computer control and output capability.

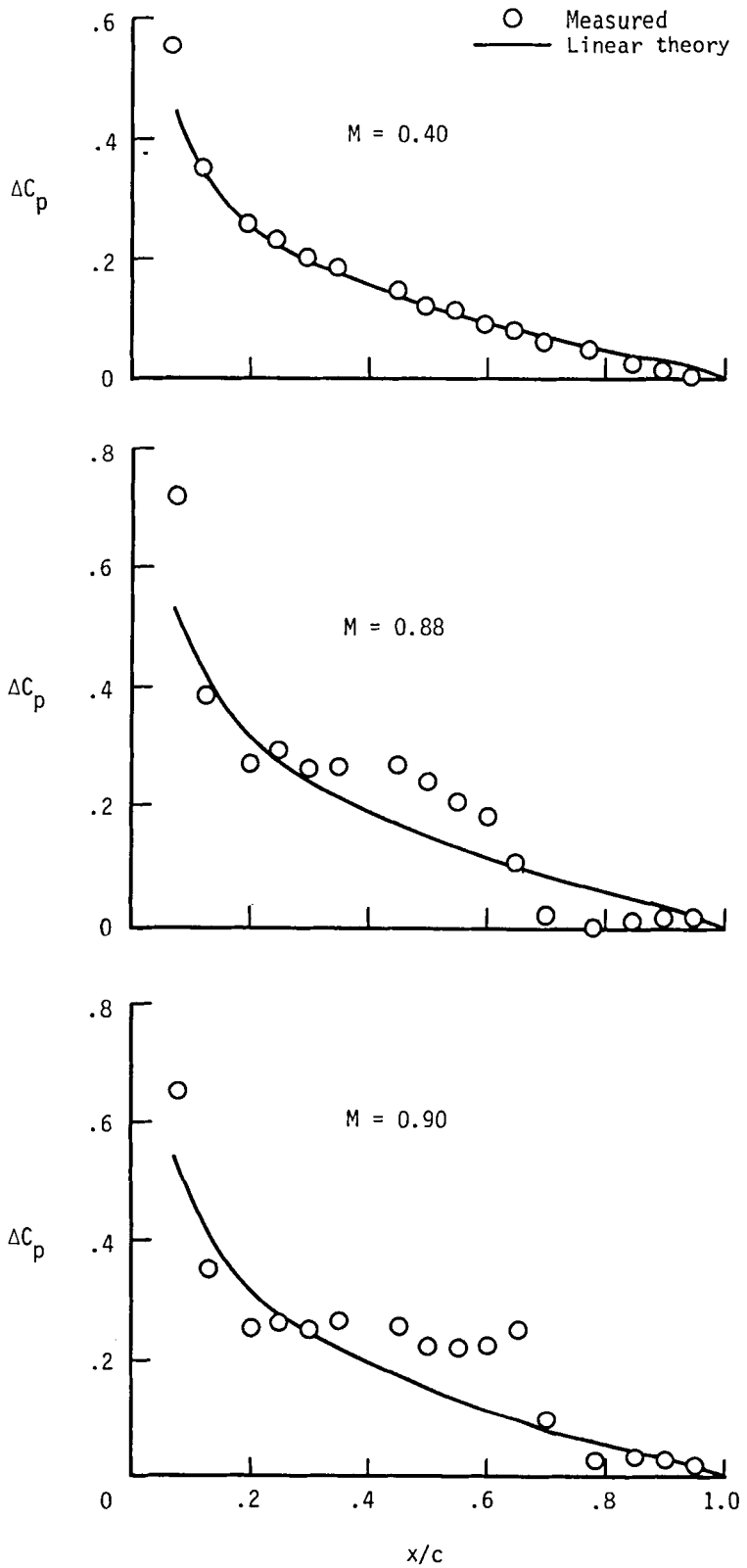

Figure 9. Comparison of experimental steady pressure distribution with linear-theory results for chord D at $\bar{\alpha} = 3°$ and $\bar{\delta} = 0°$.

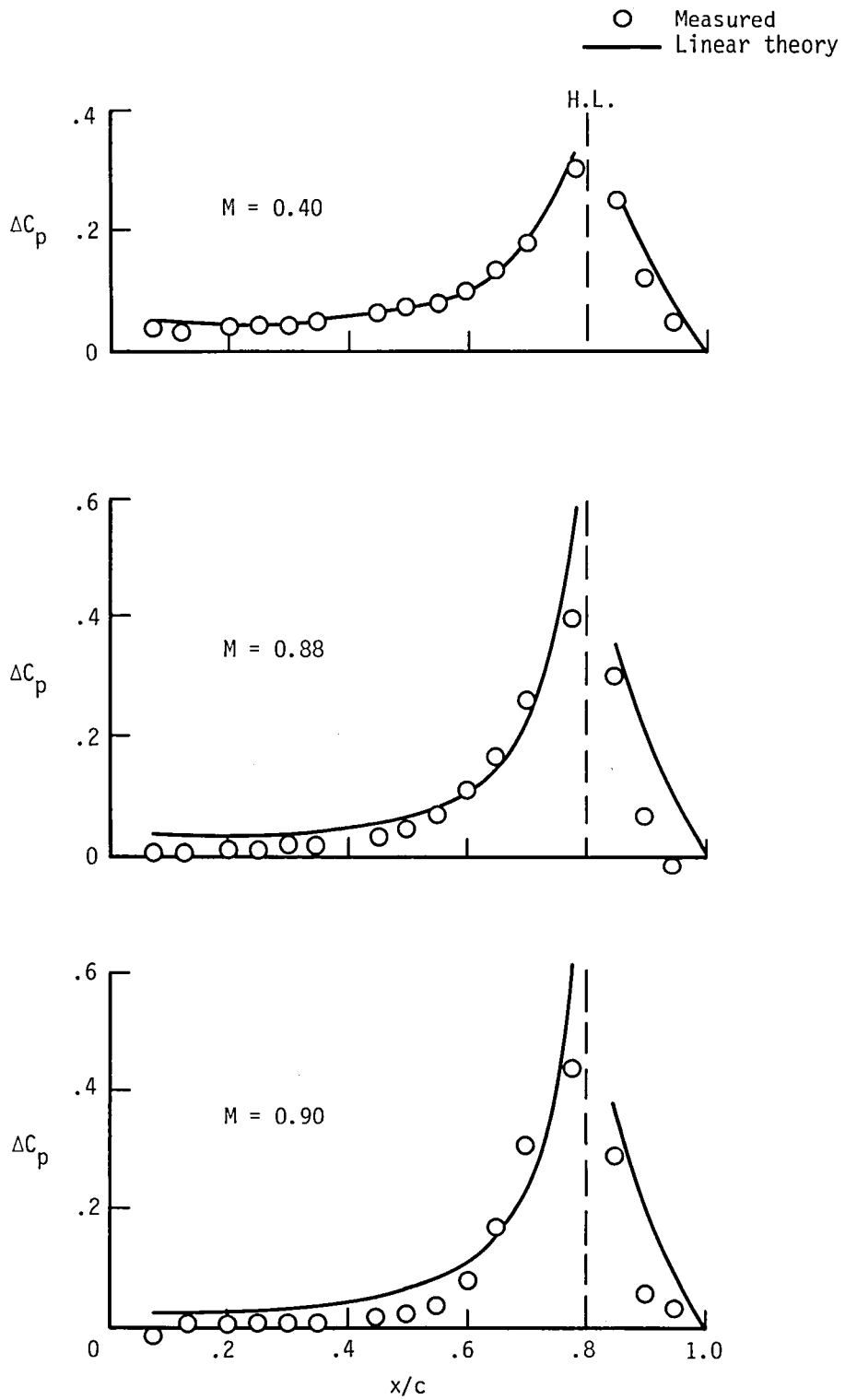

Figure 10. Comparison of experimental steady pressure distribution with linear-theory results for chord D at $\bar{\alpha} = 0.05°$ and $\bar{\delta} = 6°$.

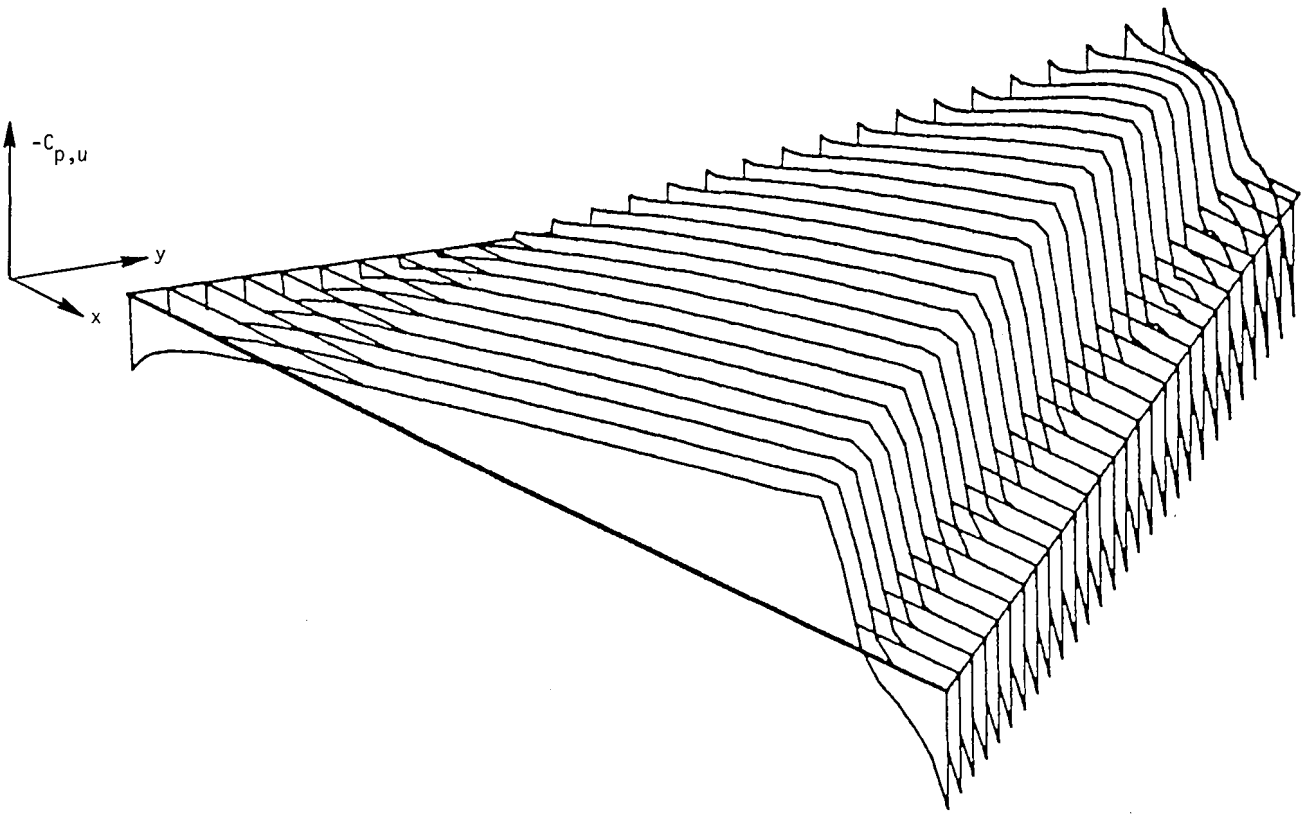

Figure 11. Calculated steady pressure distribution ($C_{p,u}$) for $M = 0.92$ and $\bar{\alpha} = 2°$. Transonic small-disturbance theory.

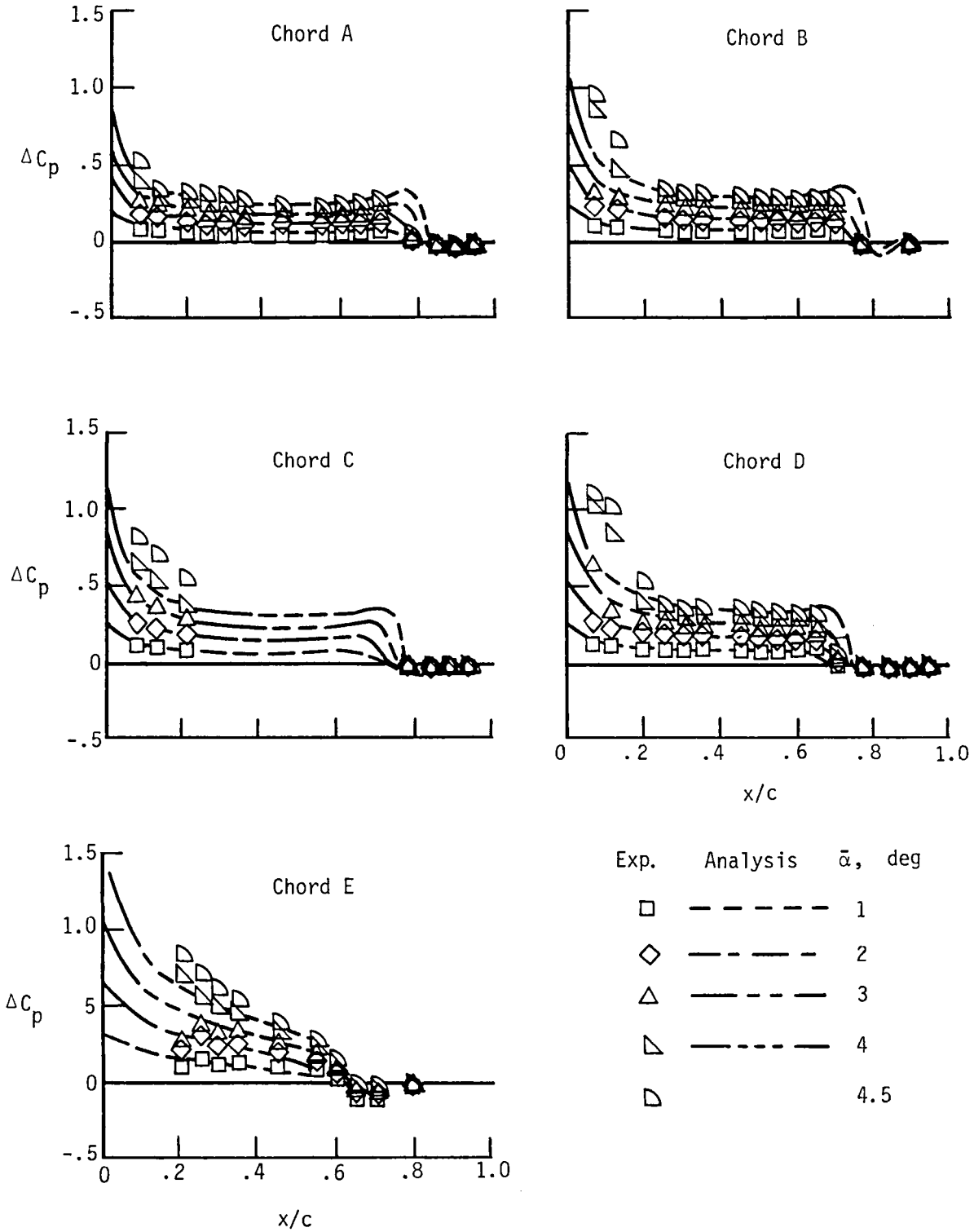

Figure 12. Comparison of experimental and analytical values of steady ΔC_p as a function of $\bar{\alpha}$ for $M = 0.90$ and $\bar{\delta} = 0°$.

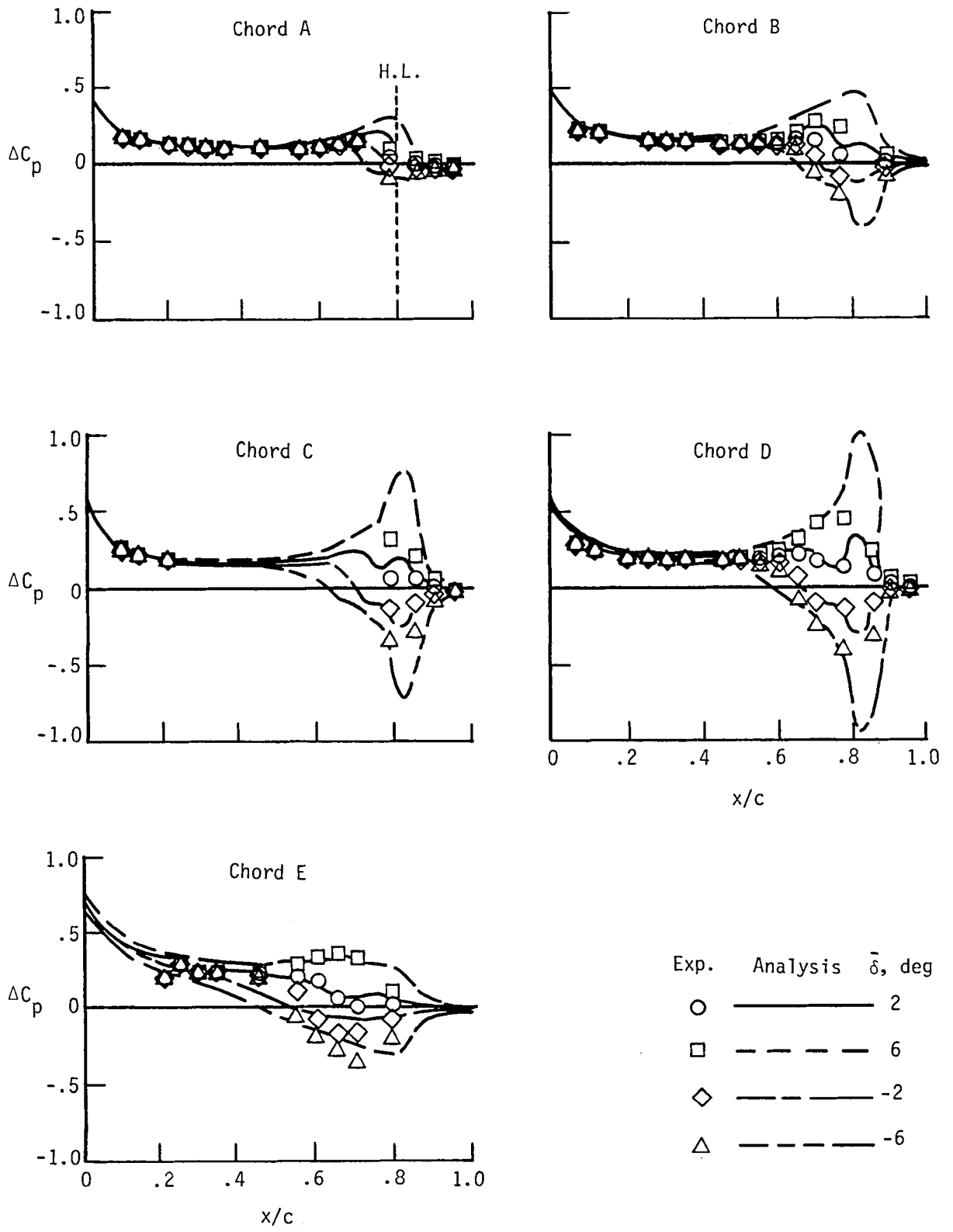

Figure 13. Comparison of experimental and analytical steady ΔC_p for variation of $\bar{\delta}$ at $\bar{\alpha} = 2°$ and $M = 0.90$.

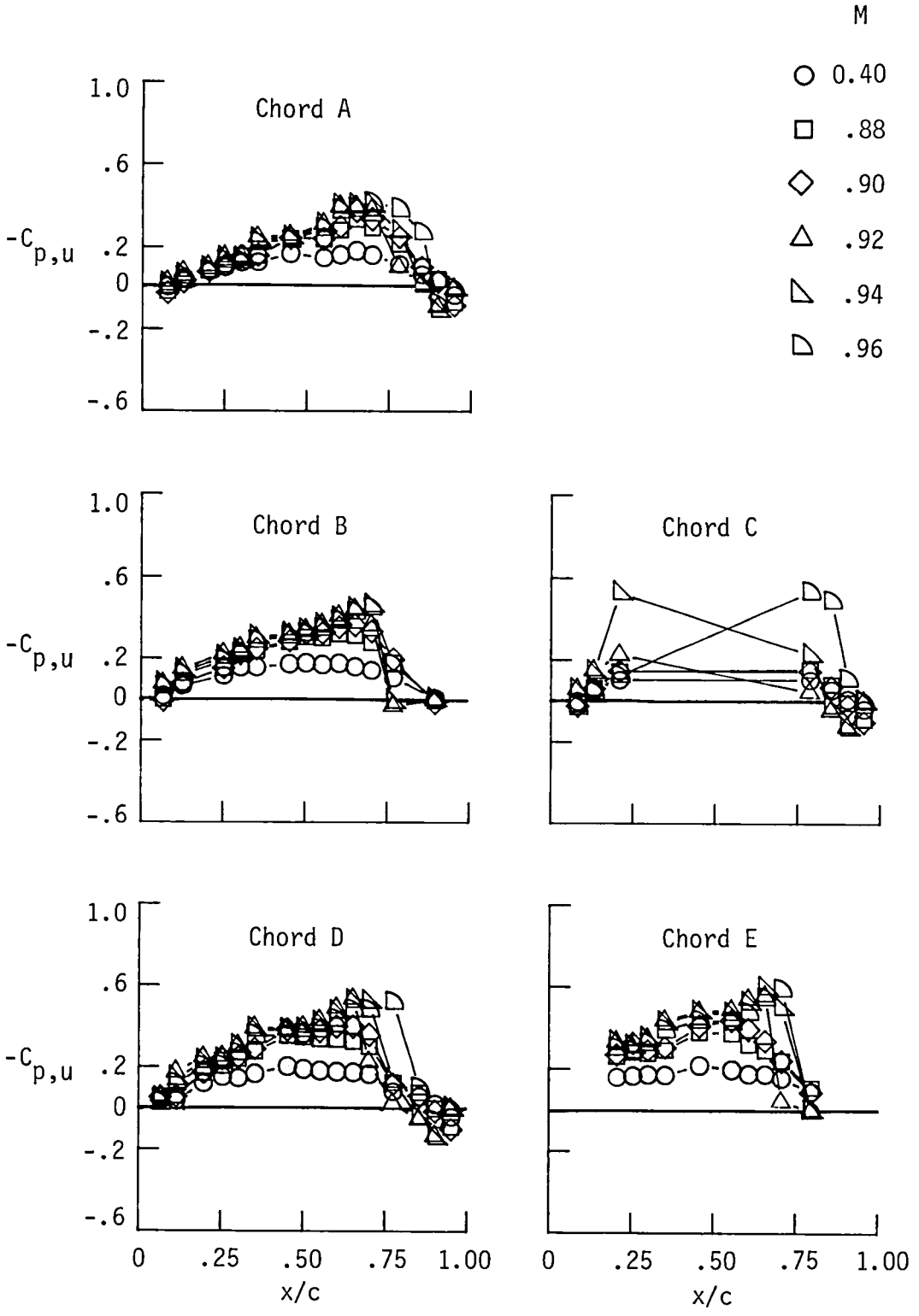

Figure 14. Upper-surface steady pressure distribution as a function of Mach number at $\bar{\alpha} = 0°$ and $\bar{\delta} = 0°$.

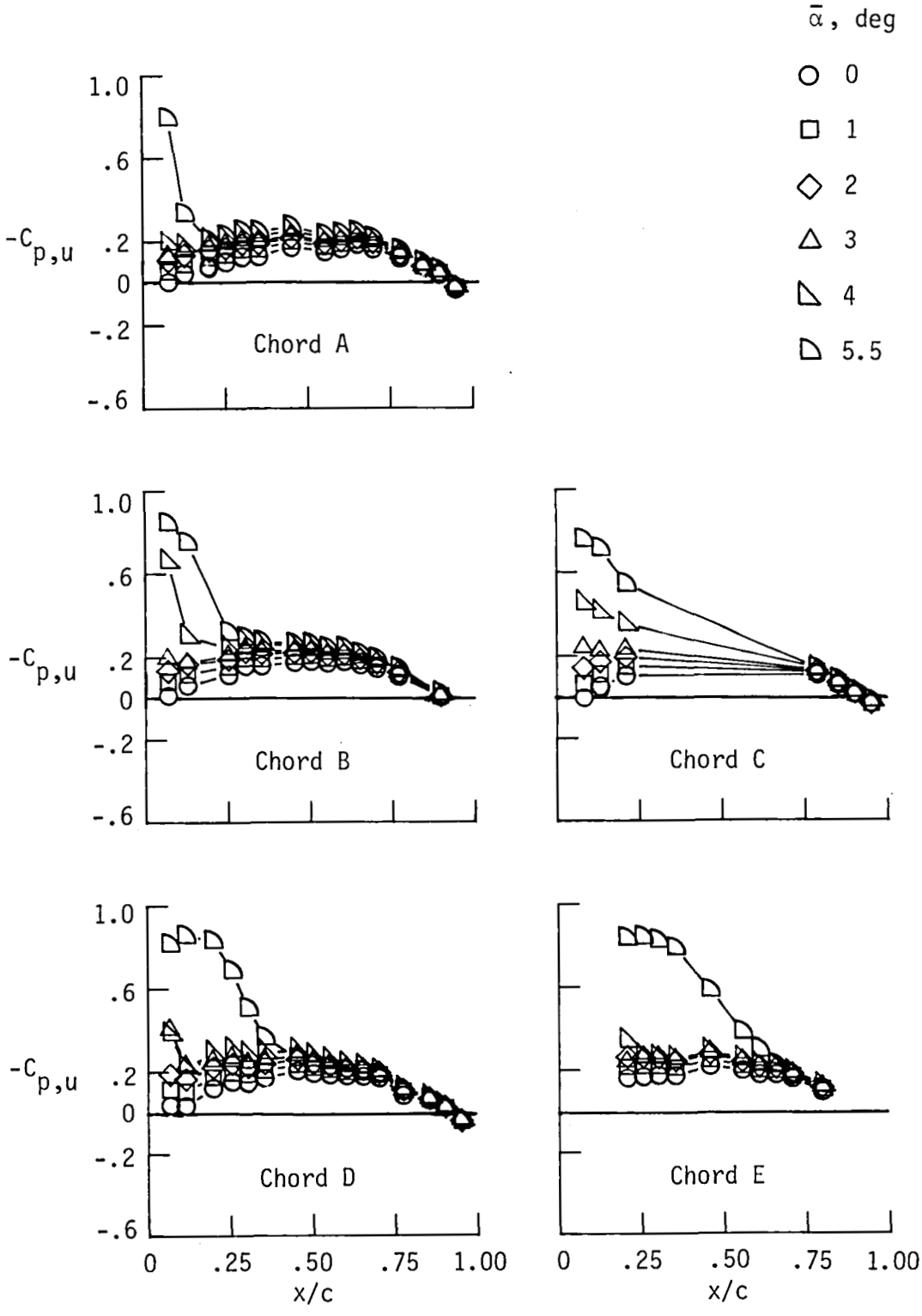

Figure 15. Steady pressure distribution as a function of $\bar{\alpha}$ for $M = 0.40$ and $\bar{\delta} = 0°$.

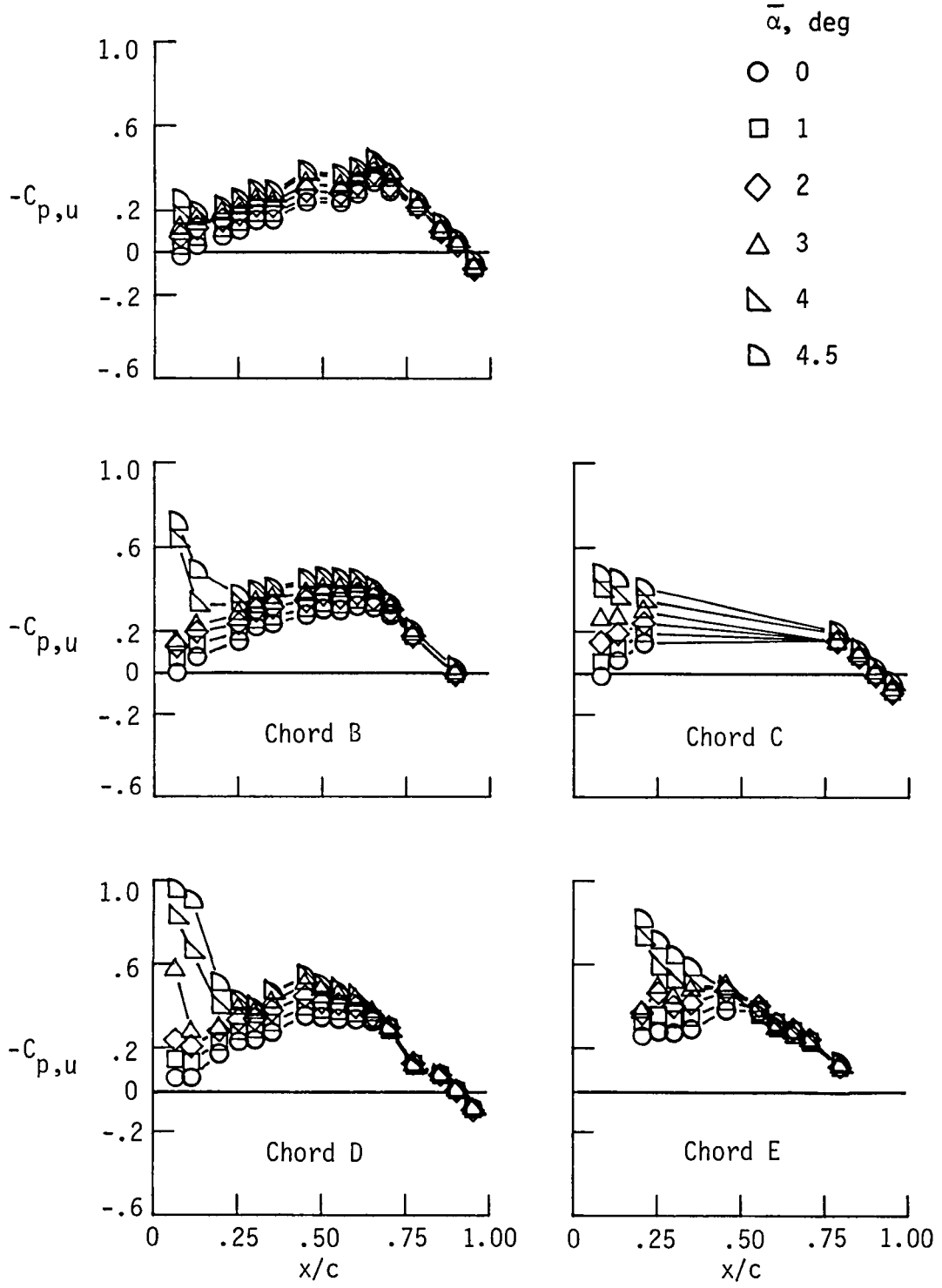

Figure 16. Steady pressure distribution as a function of $\bar{\alpha}$ for $M = 0.88$ and $\bar{\delta} = 0°$.

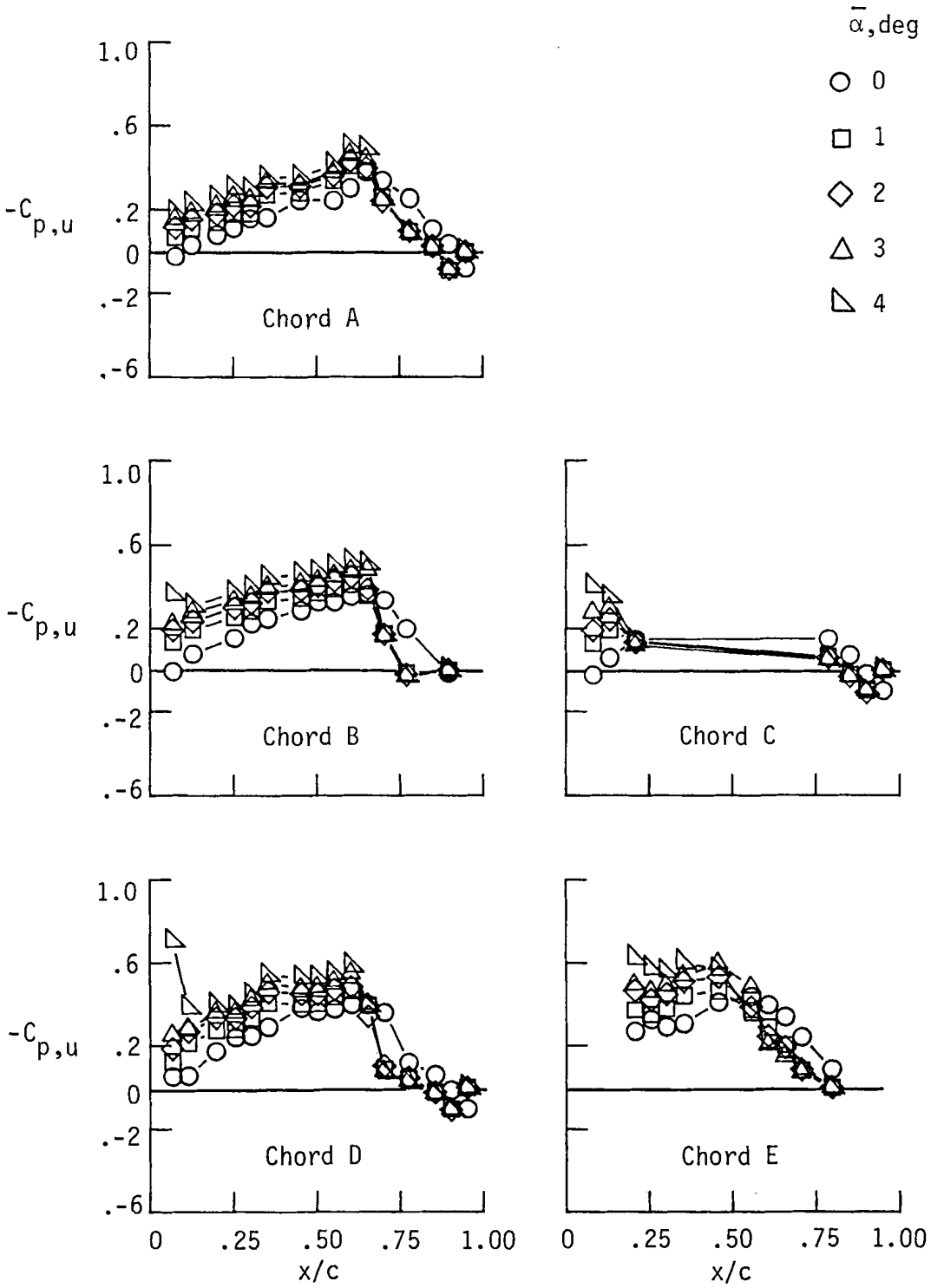

Figure 17. Steady pressure distribution as a function of $\bar{\alpha}$ for $M = 0.90$ and $\bar{\delta} = 0°$.

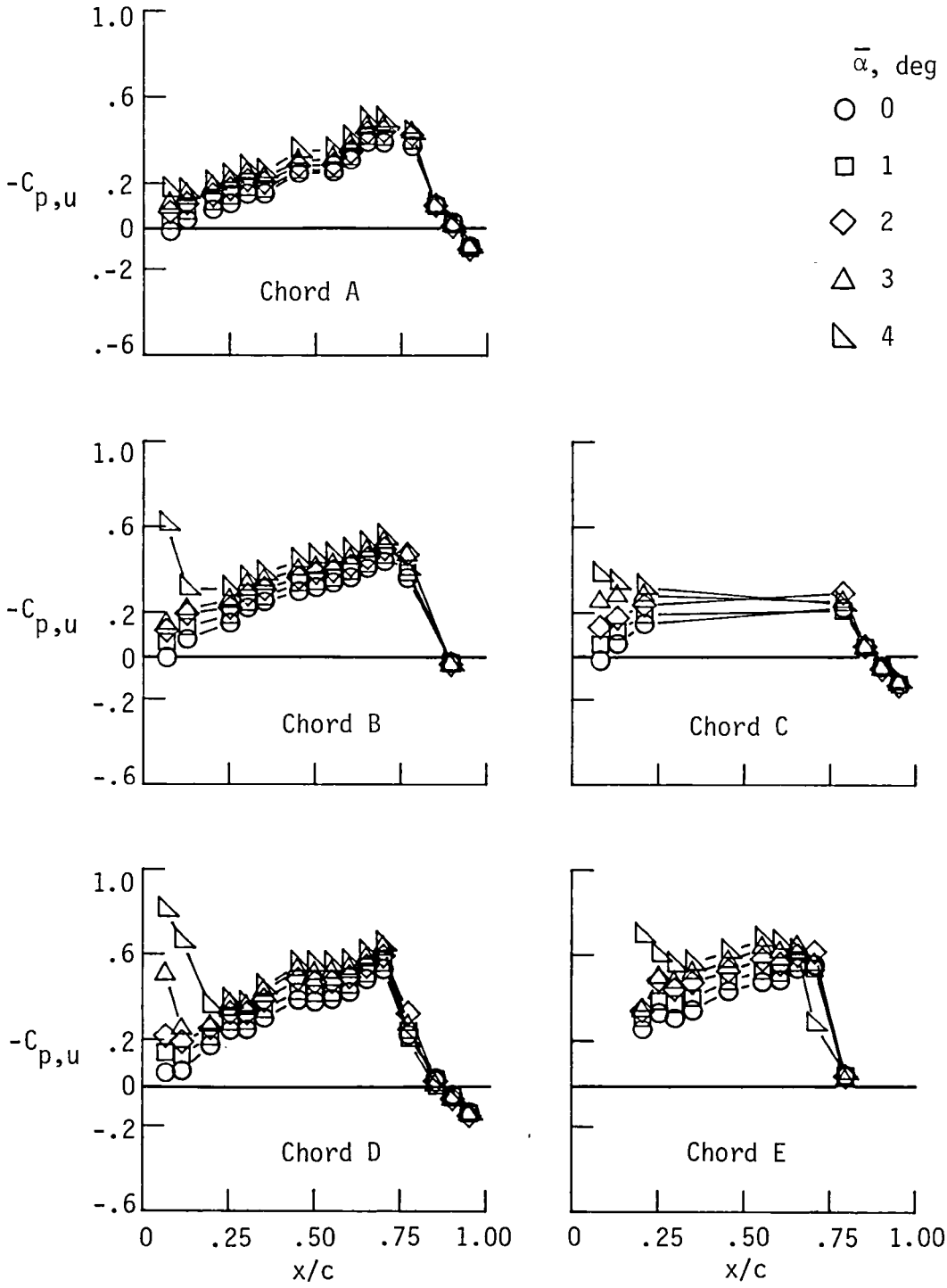

Figure 18. Steady pressure distribution as a function of $\bar{\alpha}$ for $M = 0.92$ and $\bar{\delta} = 0°$.

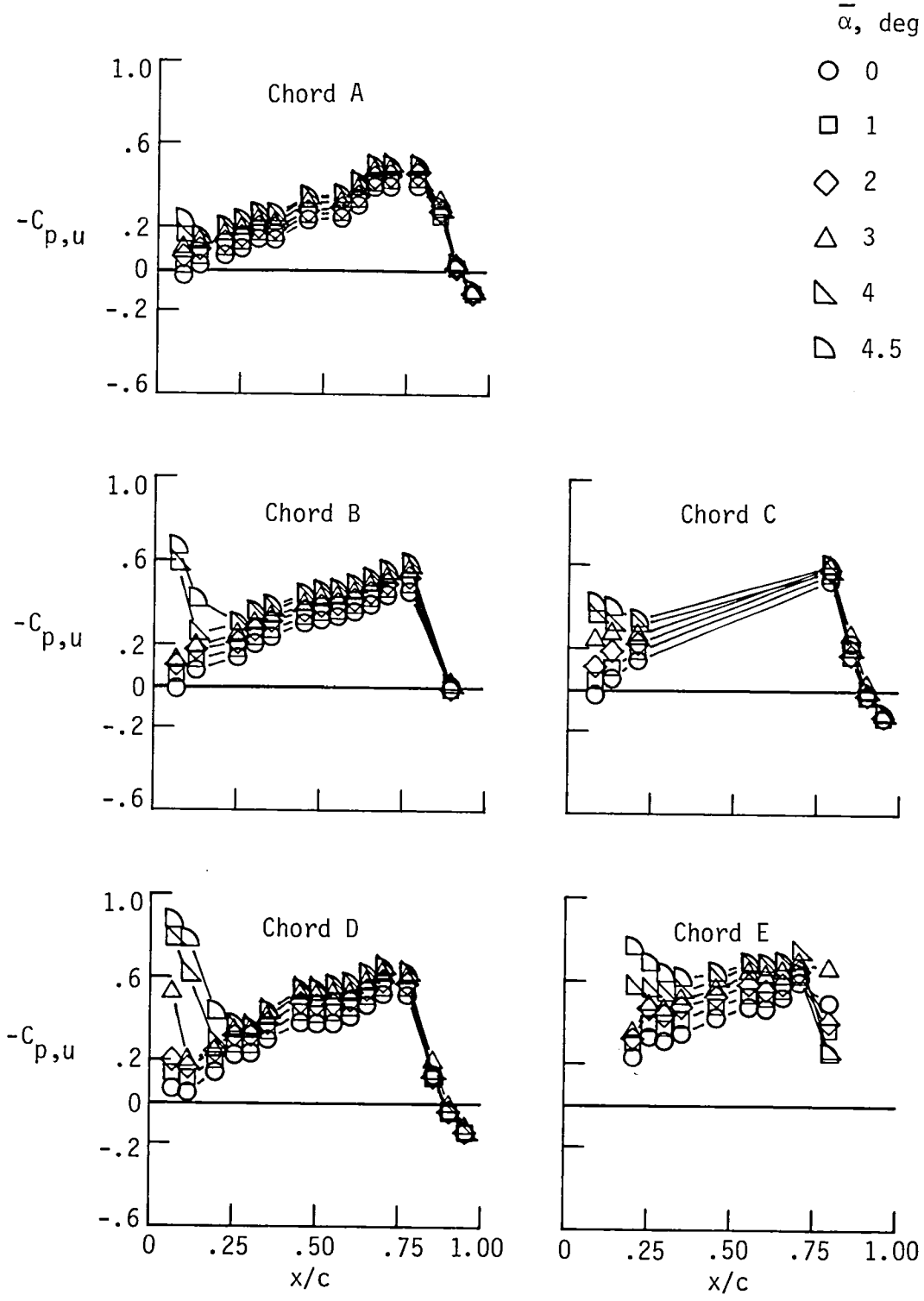

(a) $C_{p,u}$.

Figure 19. Steady pressure distributions as a function of $\bar{\alpha}$ for $M = 0.94$ and $\bar{\delta} = 0°$.

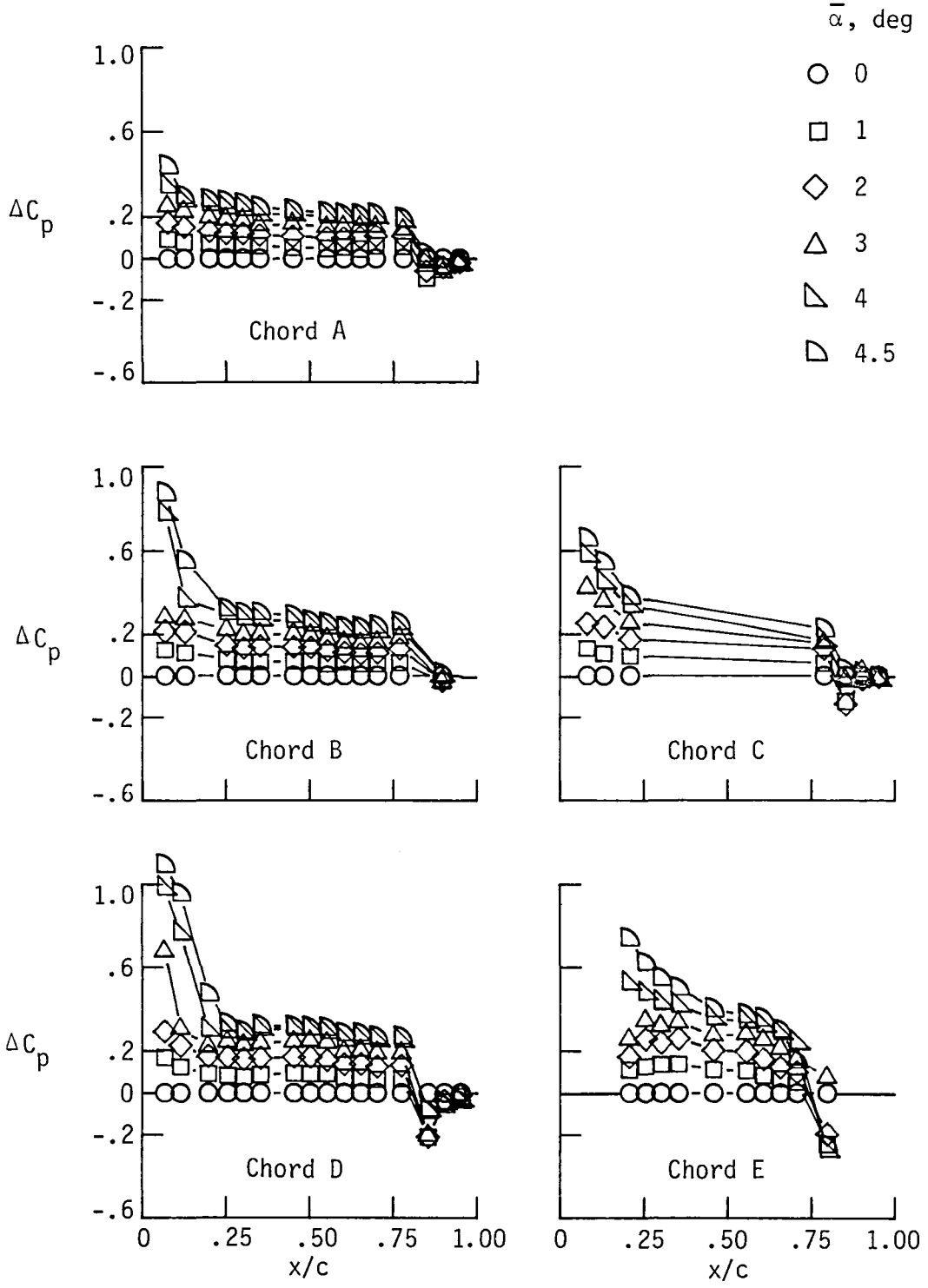

(b) ΔC_p.

Figure 19. Concluded.

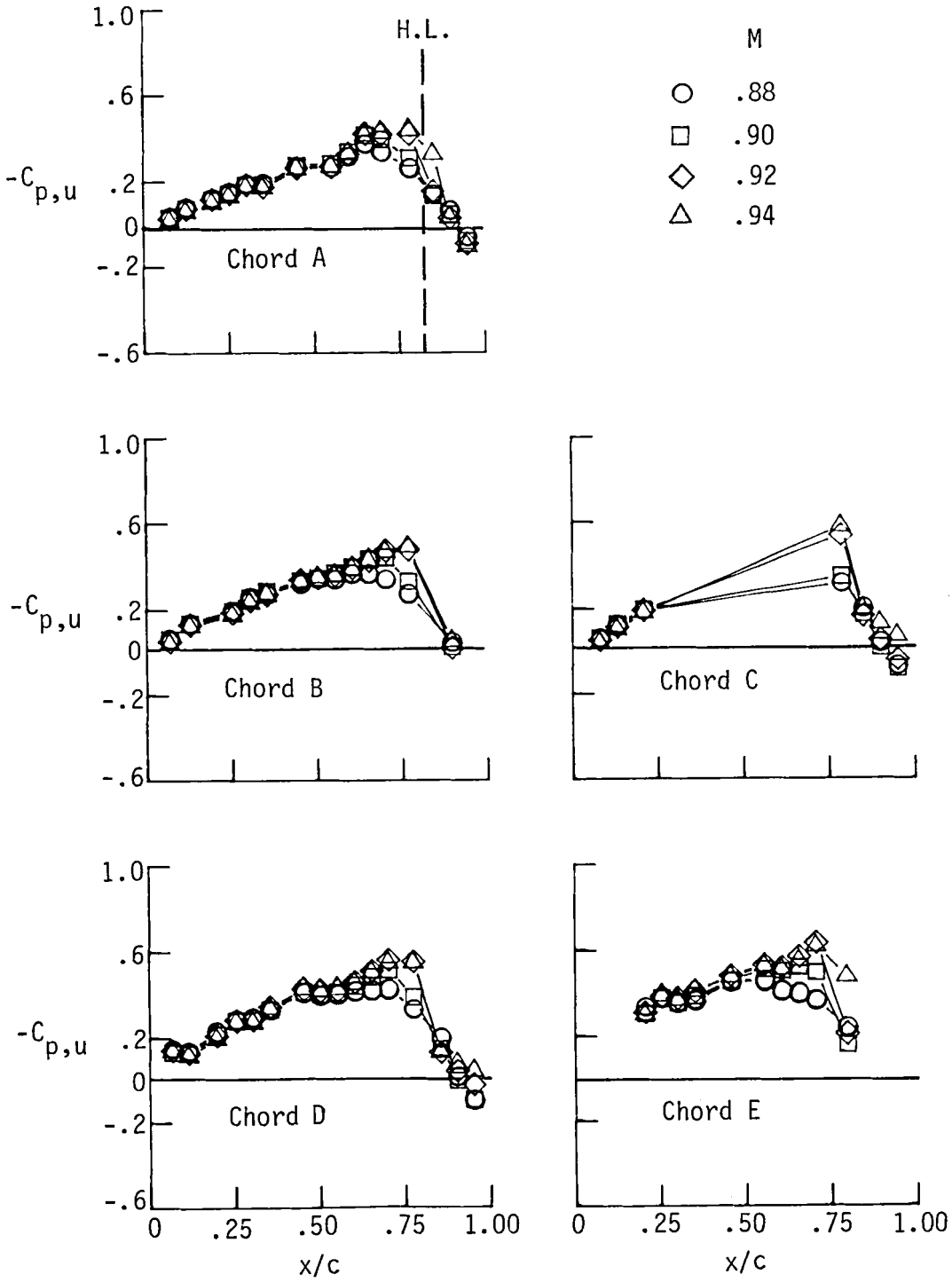

(a) $C_{p,u}$; $\bar{\delta} = 6°$.

Figure 20. Steady pressure distributions as a function of Mach number for $\bar{\alpha} = 1°$.

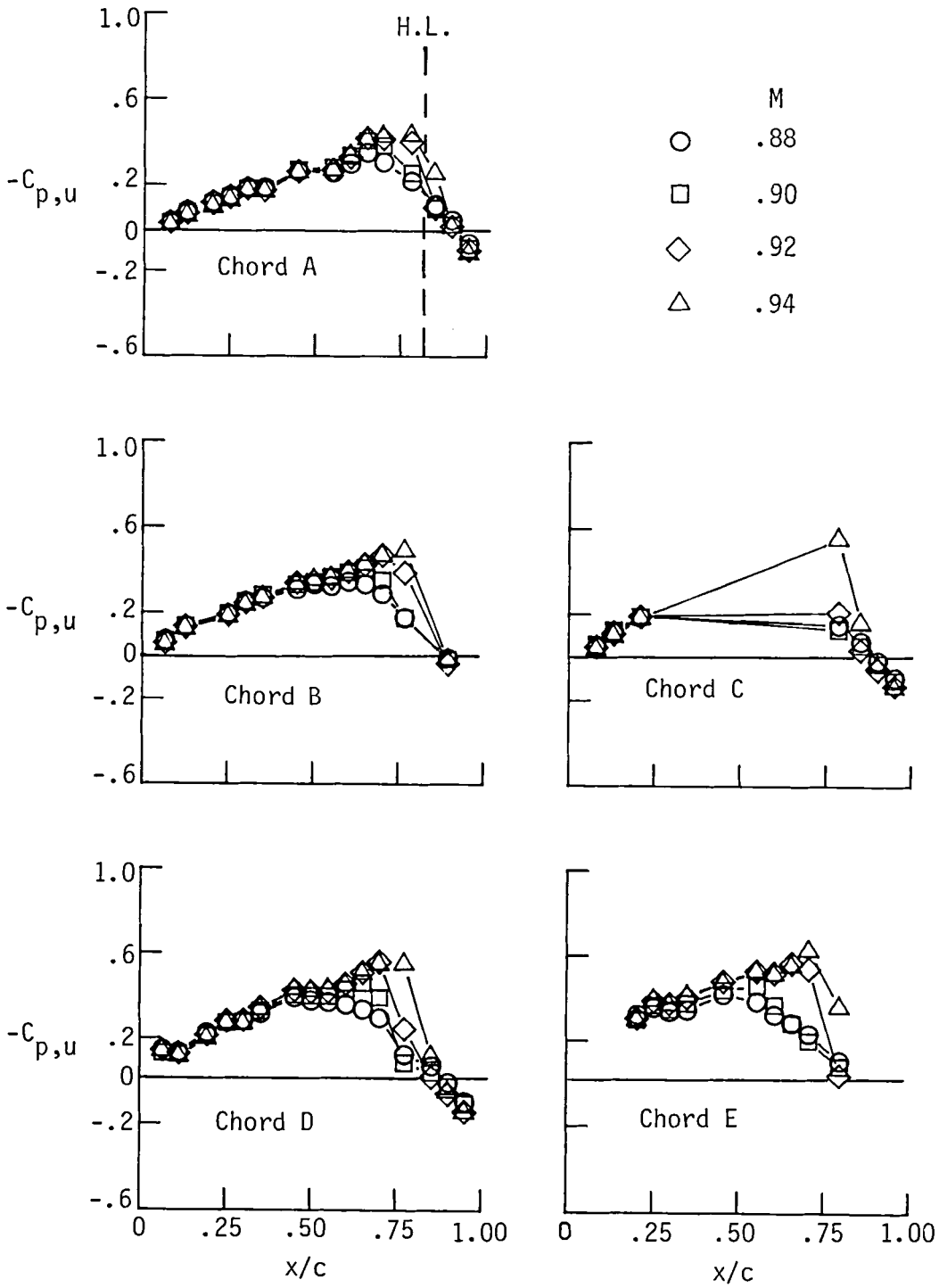

(b) $C_{p,u}$; $\bar{\delta} = 0°$.

Figure 20. Continued.

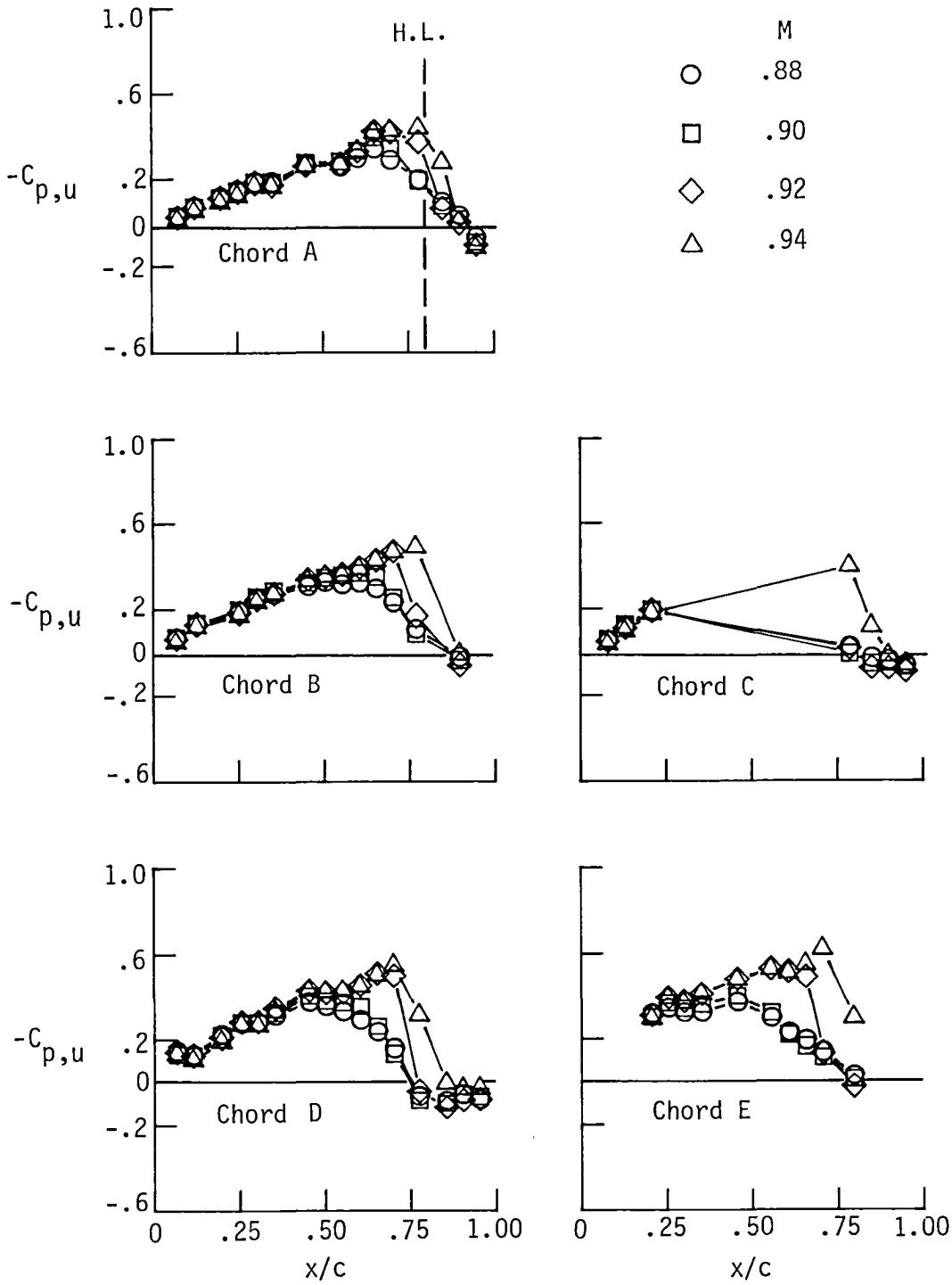

(c) $C_{p,u}$; $\bar{\delta} = -6°$.

Figure 20. Continued.

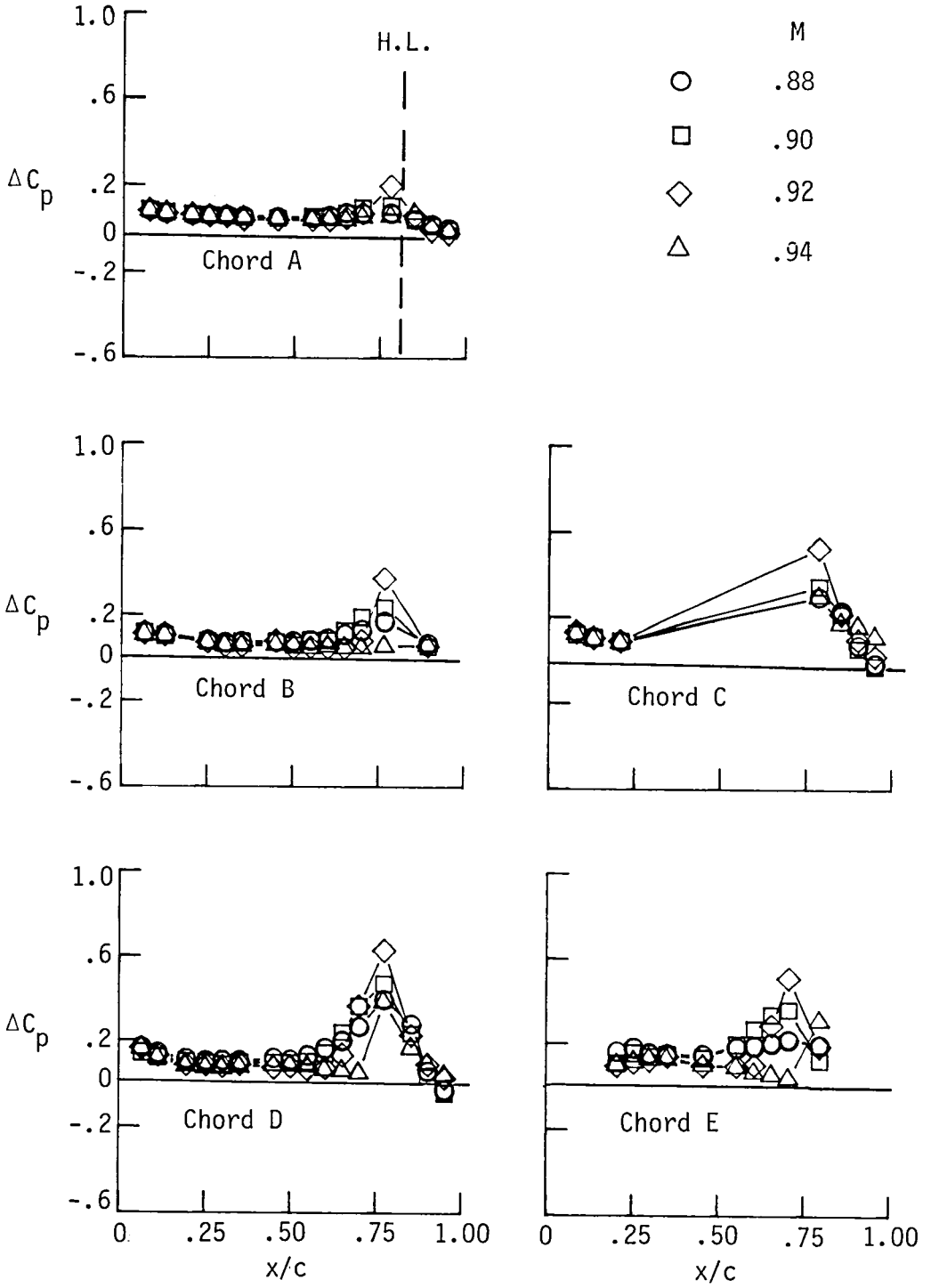

(d) ΔC_p; $\bar{\delta} = 6°$.

Figure 20. Continued.

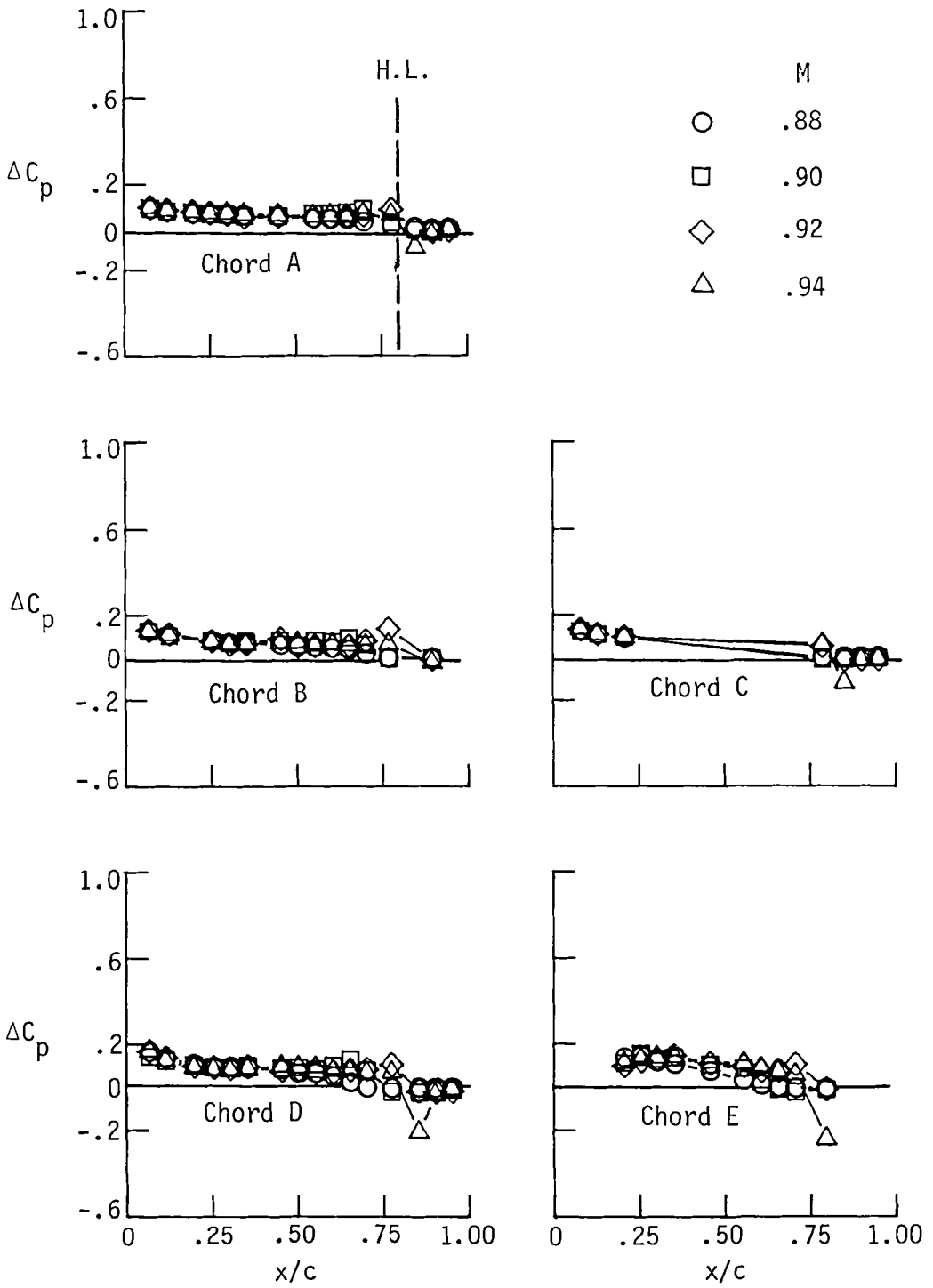

(e) ΔC_p; $\bar{\delta} = 0°$.

Figure 20. Continued.

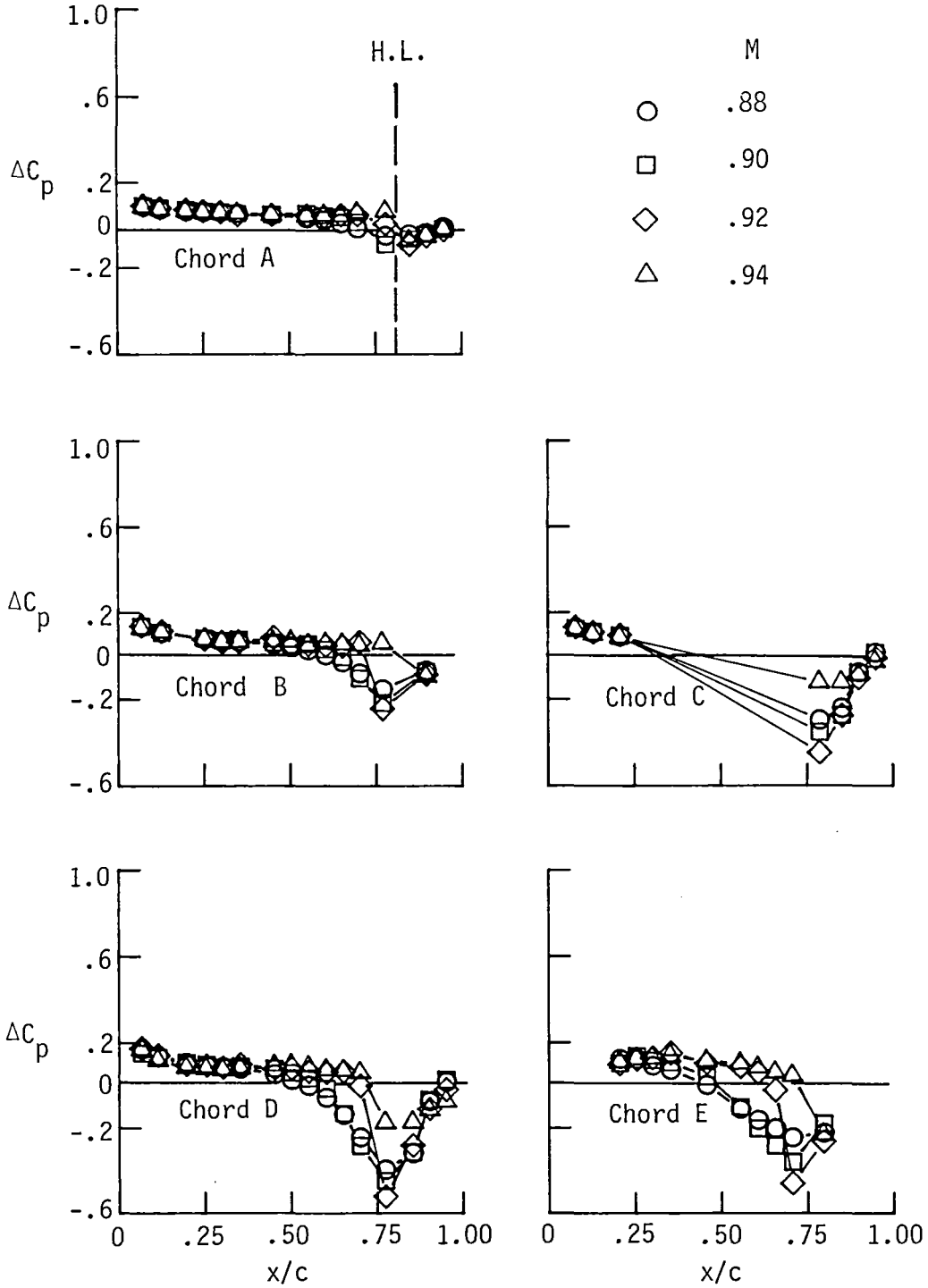

(f) ΔC_p; $\bar{\delta} = -6°$.

Figure 20. Concluded.

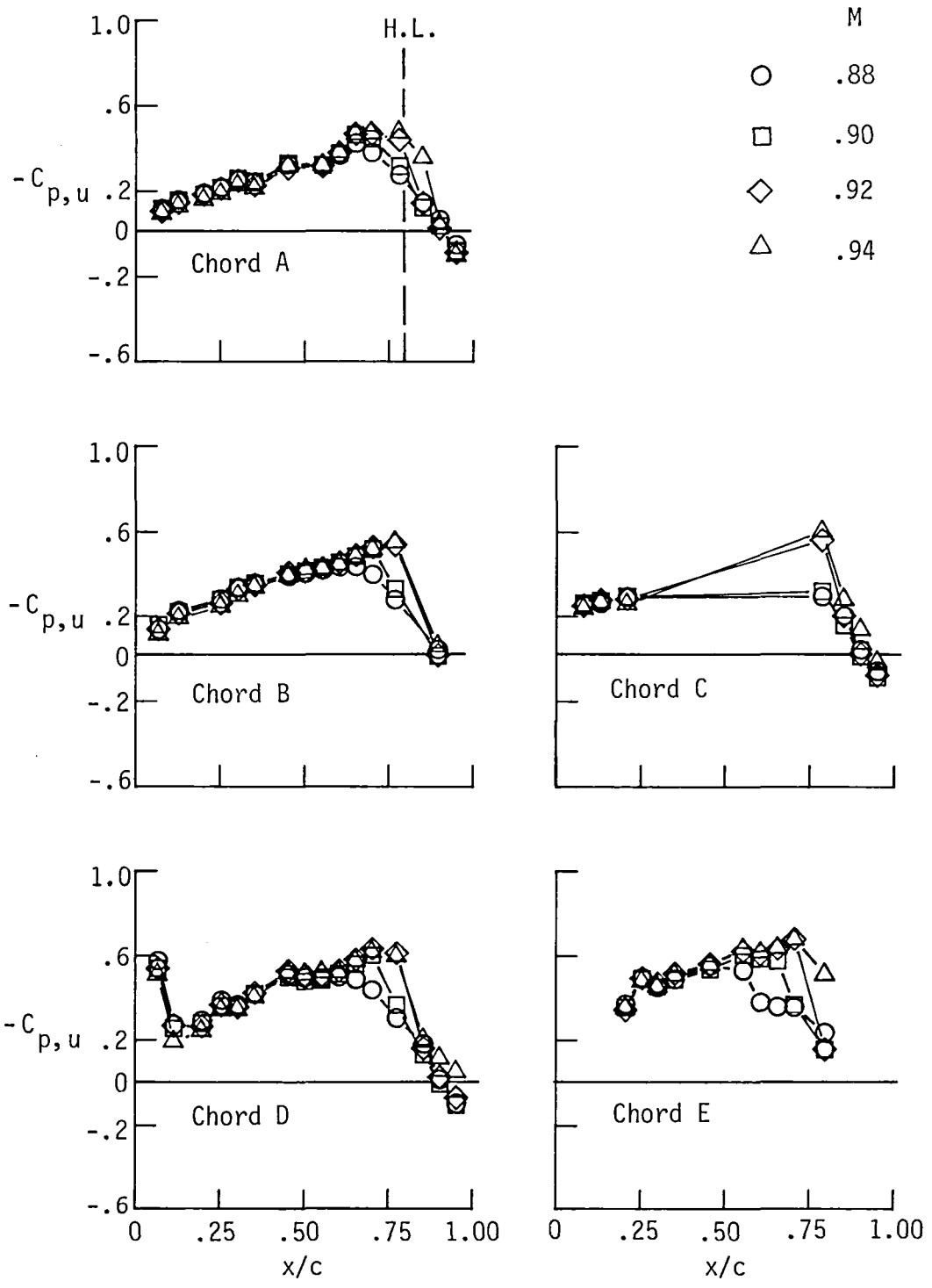

(a) $C_{p,u}$; $\bar{\delta} = 6°$.

Figure 21. Steady pressure distributions as a function of Mach number for $\bar{\alpha} = 3°$.

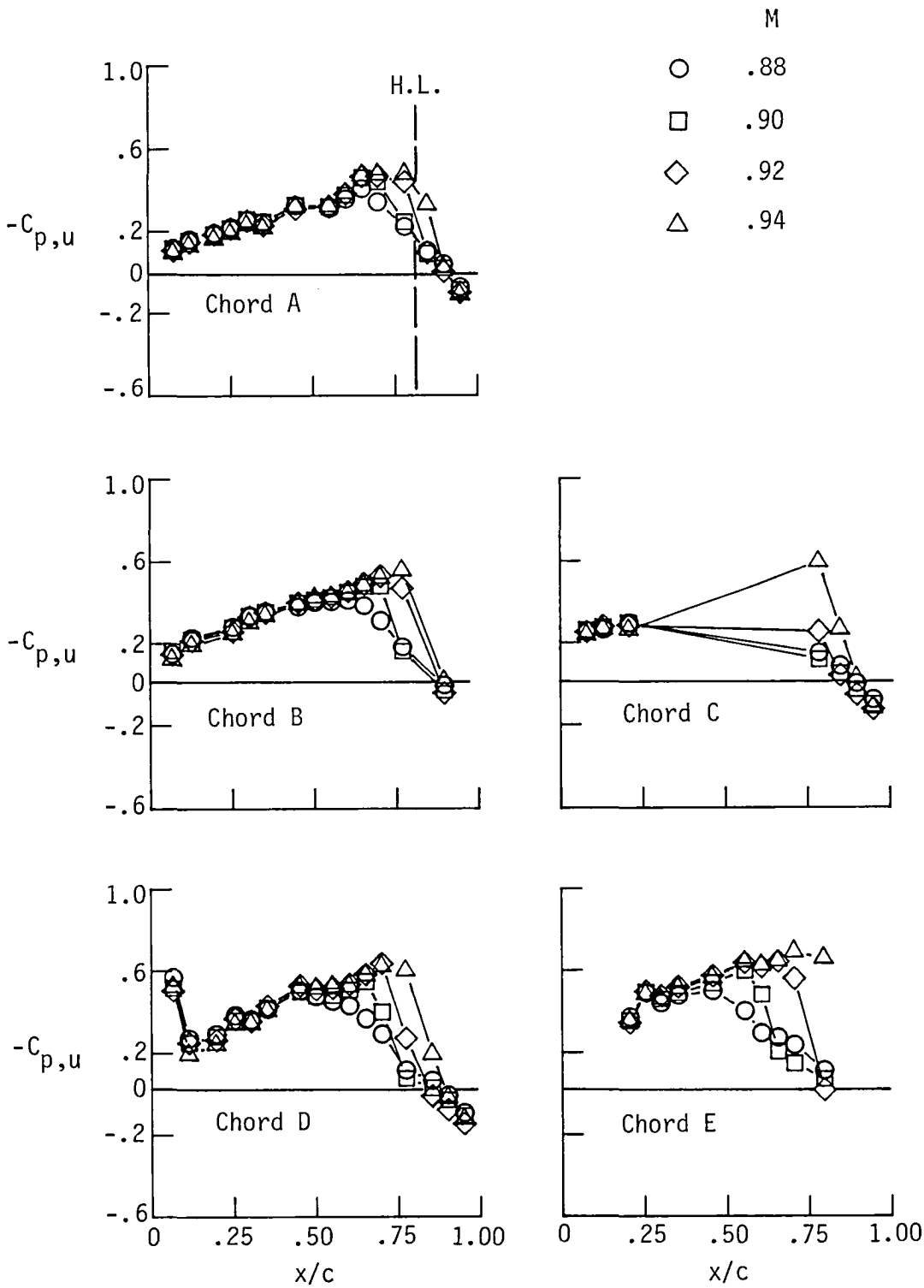

(b) $C_{p,u}$; $\bar{\delta} = 0°$.

Figure 21. Continued.

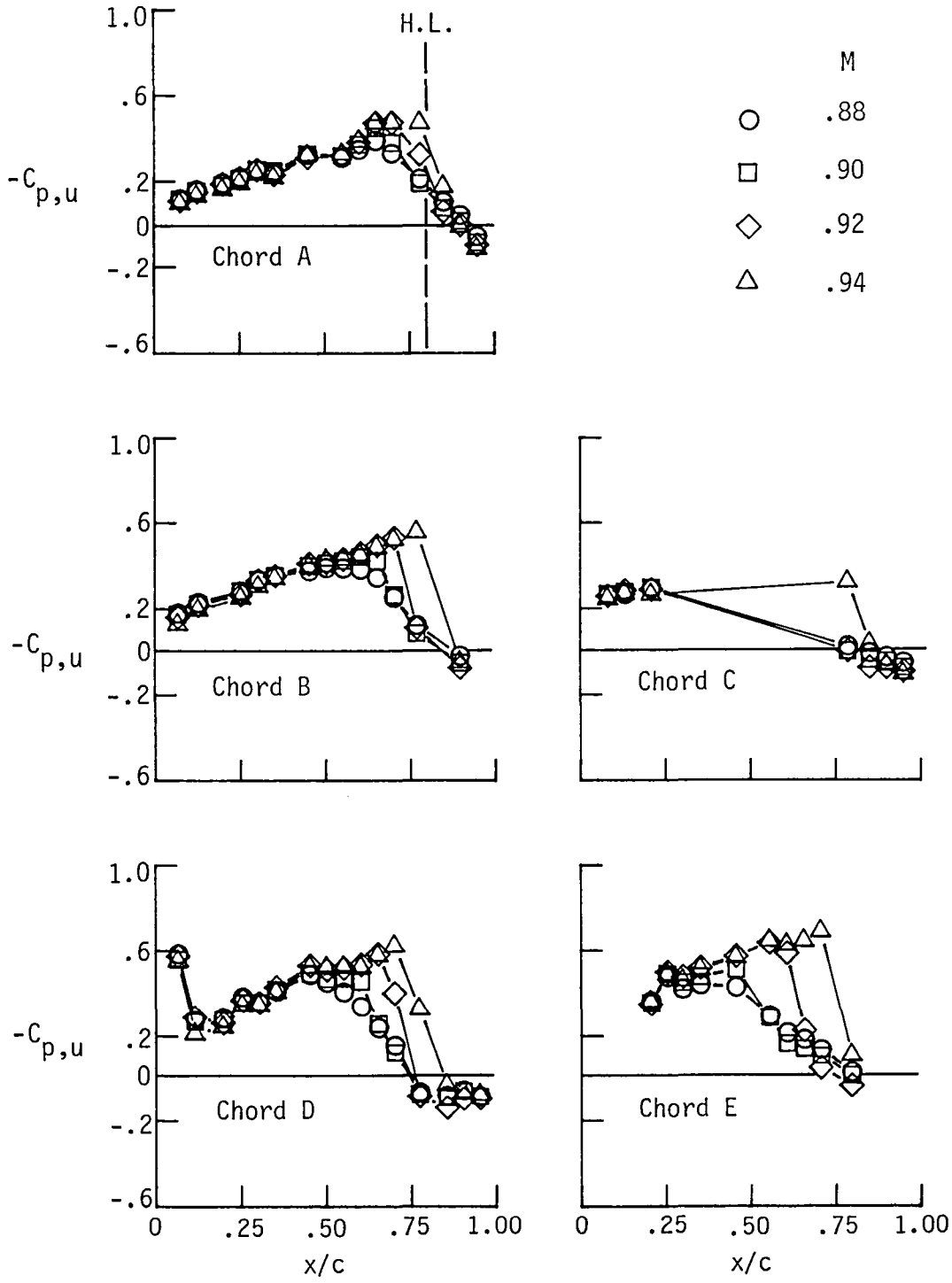

(c) $C_{p,u}$; $\bar{\delta} = -6°$.

Figure 21. Continued.

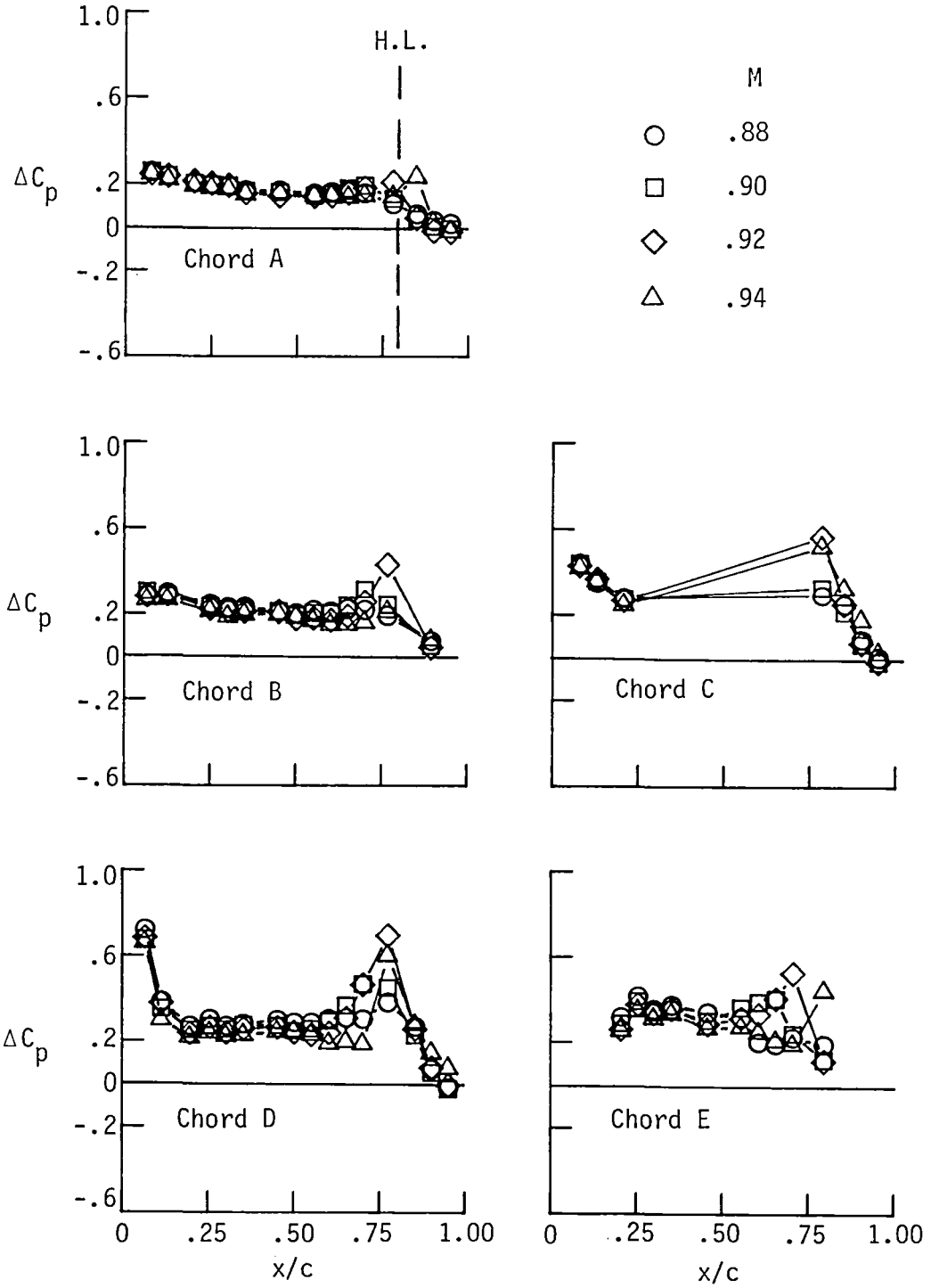

(d) ΔC_p; $\bar{\delta} = 6°$.

Figure 21. Continued.

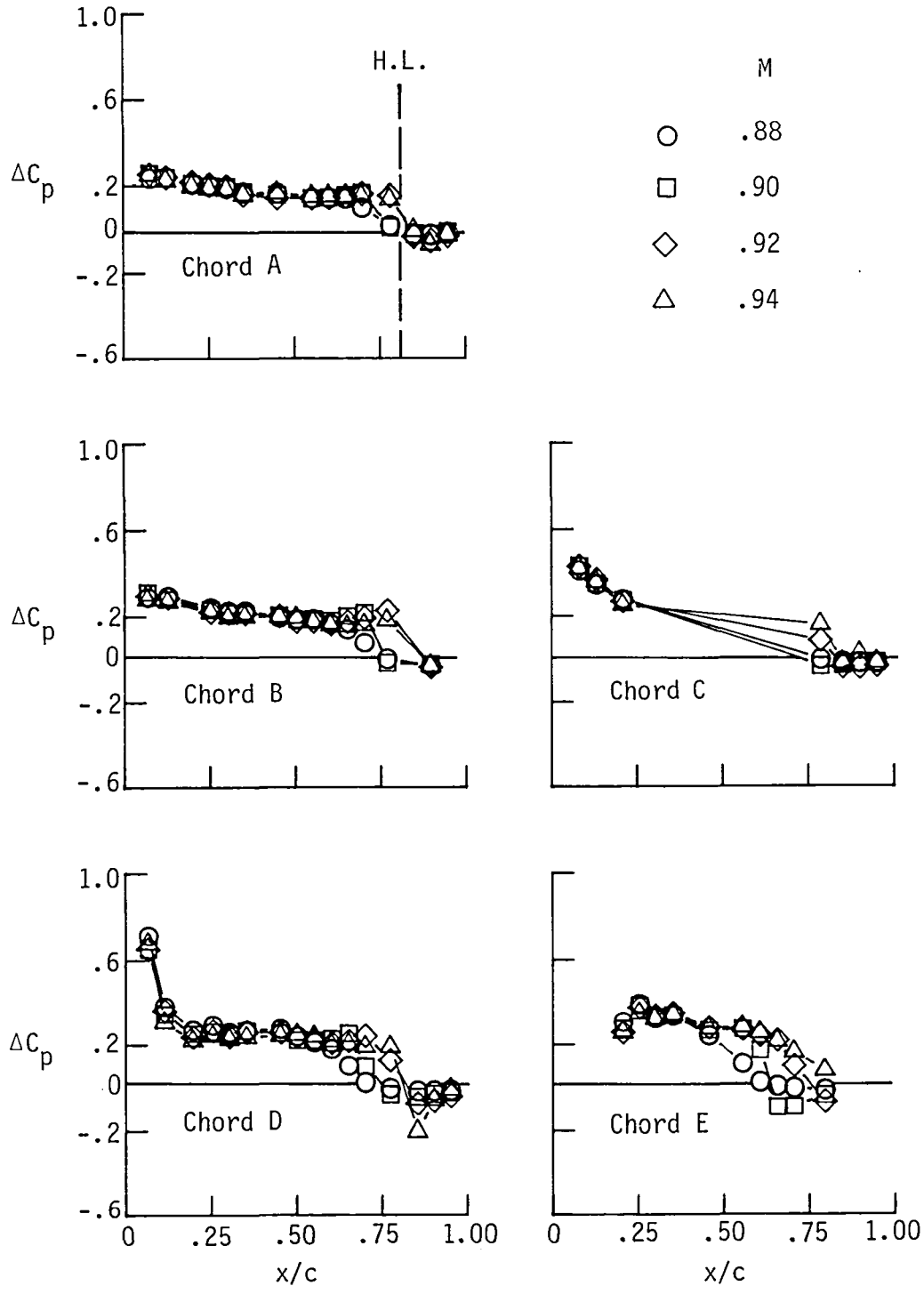

(e) ΔC_p; $\bar{\delta} = 0°$.

Figure 21. Continued.

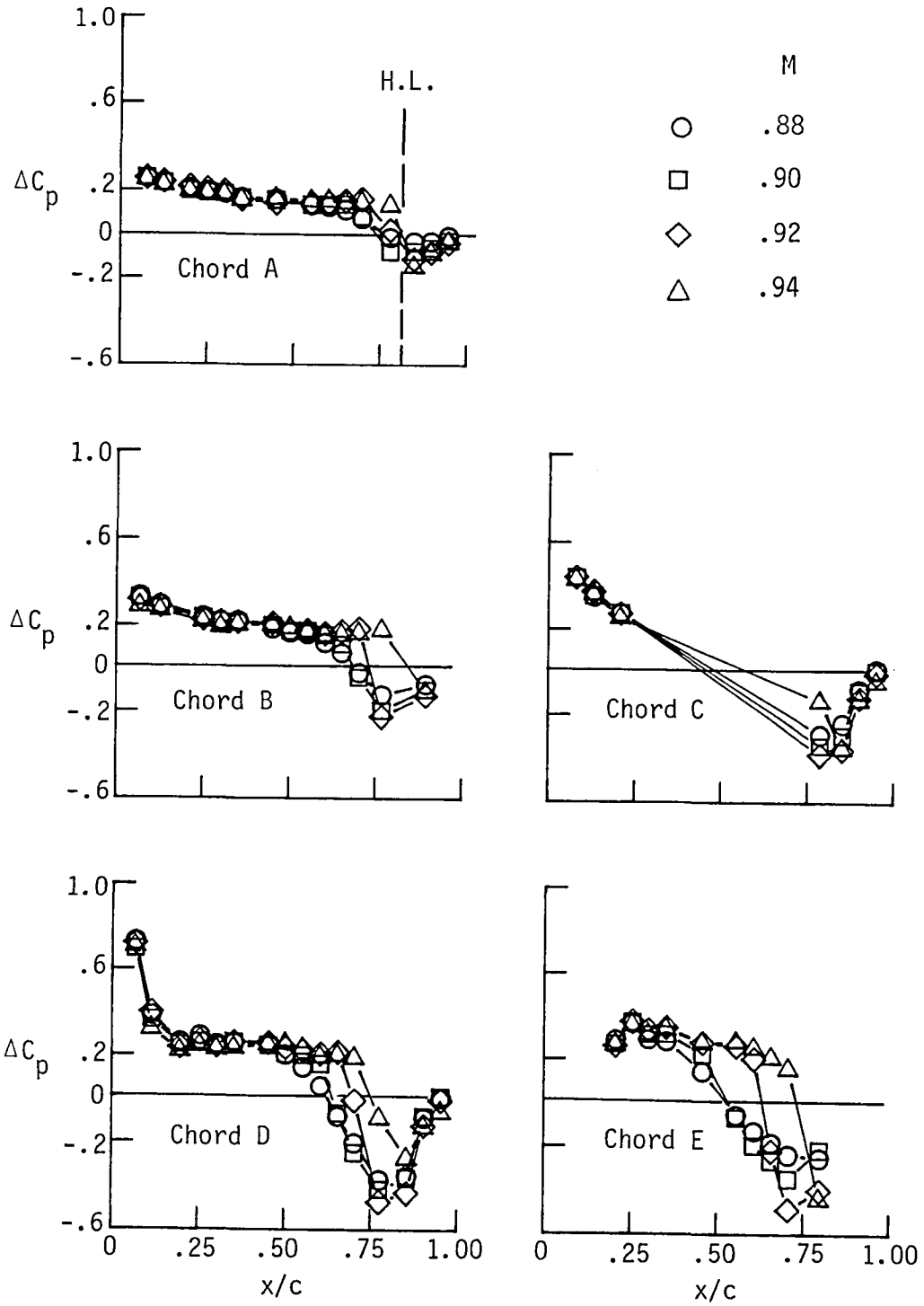

(f) ΔC_p; $\bar{\delta} = -6°$.

Figure 21. Concluded.

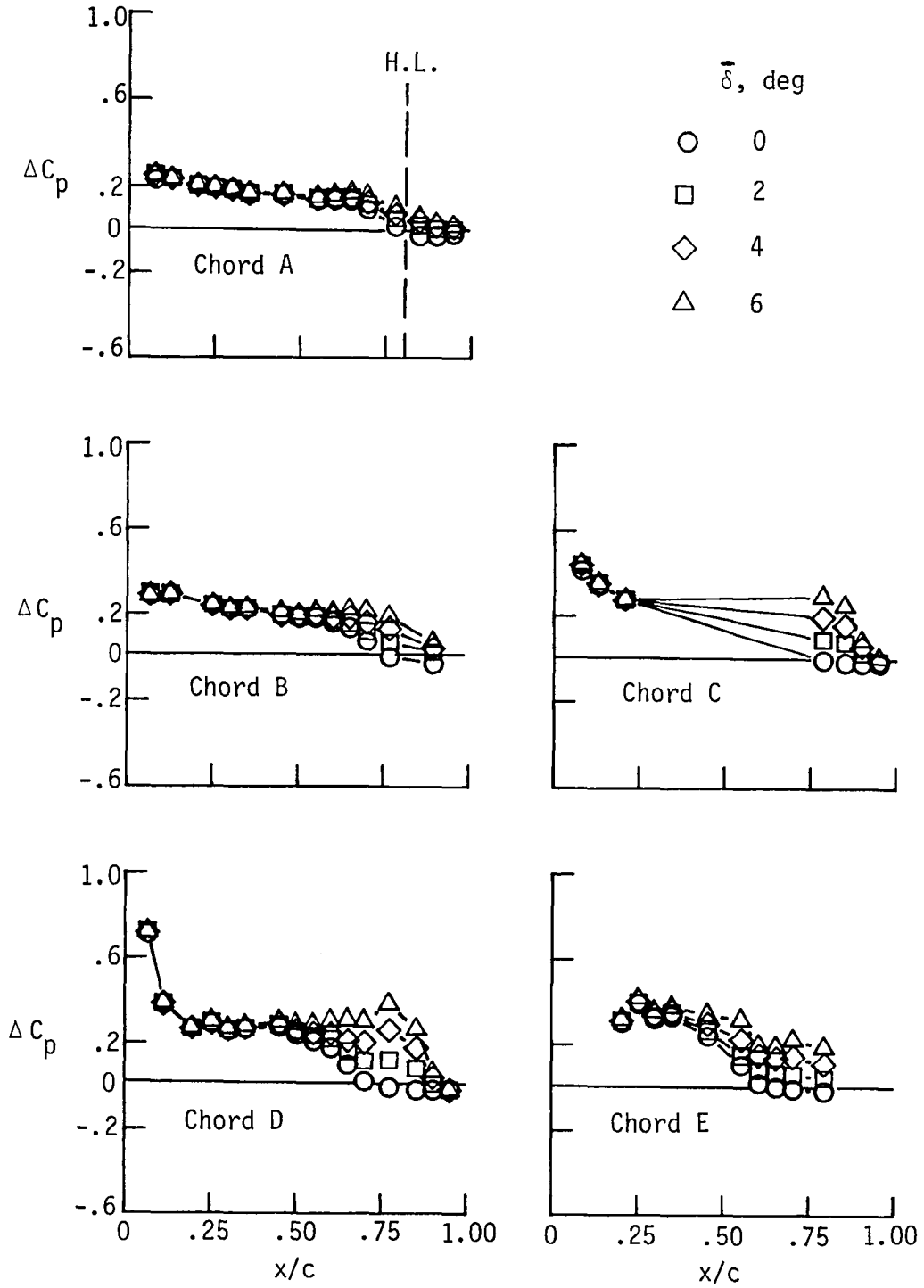

(a) $M = 0.88$.

Figure 22. Steady pressure distribution as a function of positive $\bar{\delta}$ at $\bar{\alpha} = 3°$.

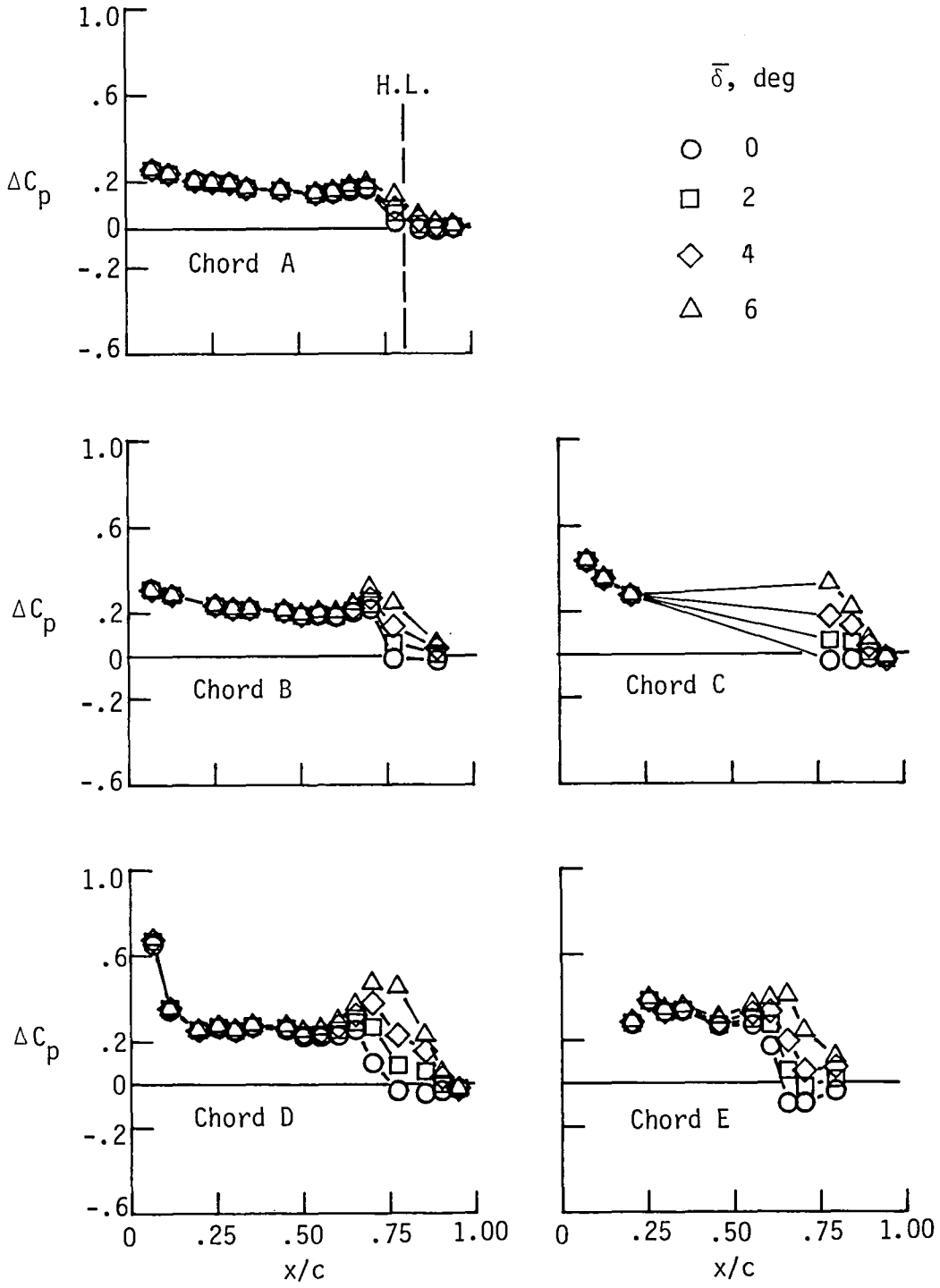

(b) $M = 0.90$.

Figure 22. Continued.

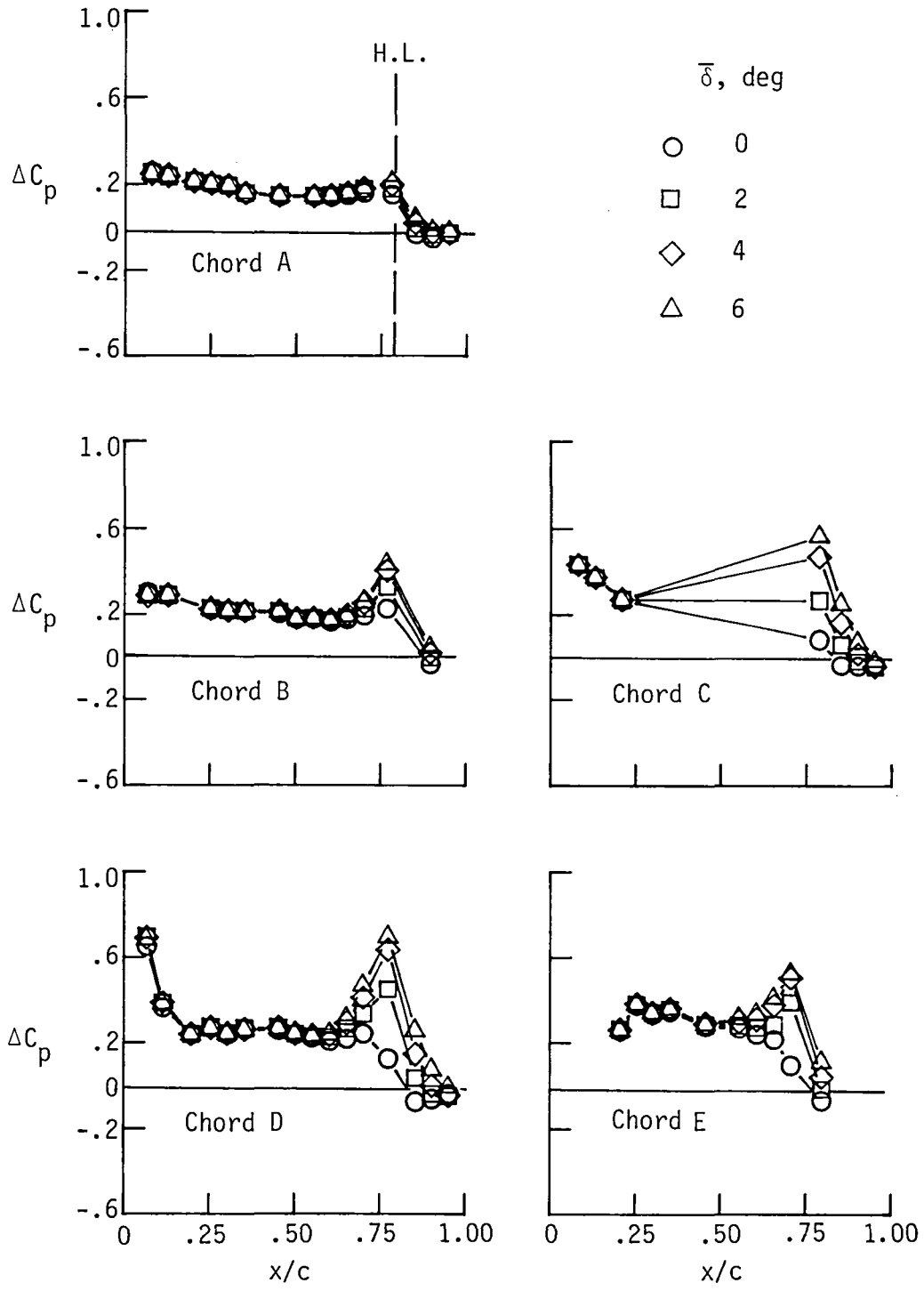

(c) $M = 0.92$.

Figure 22. Continued.

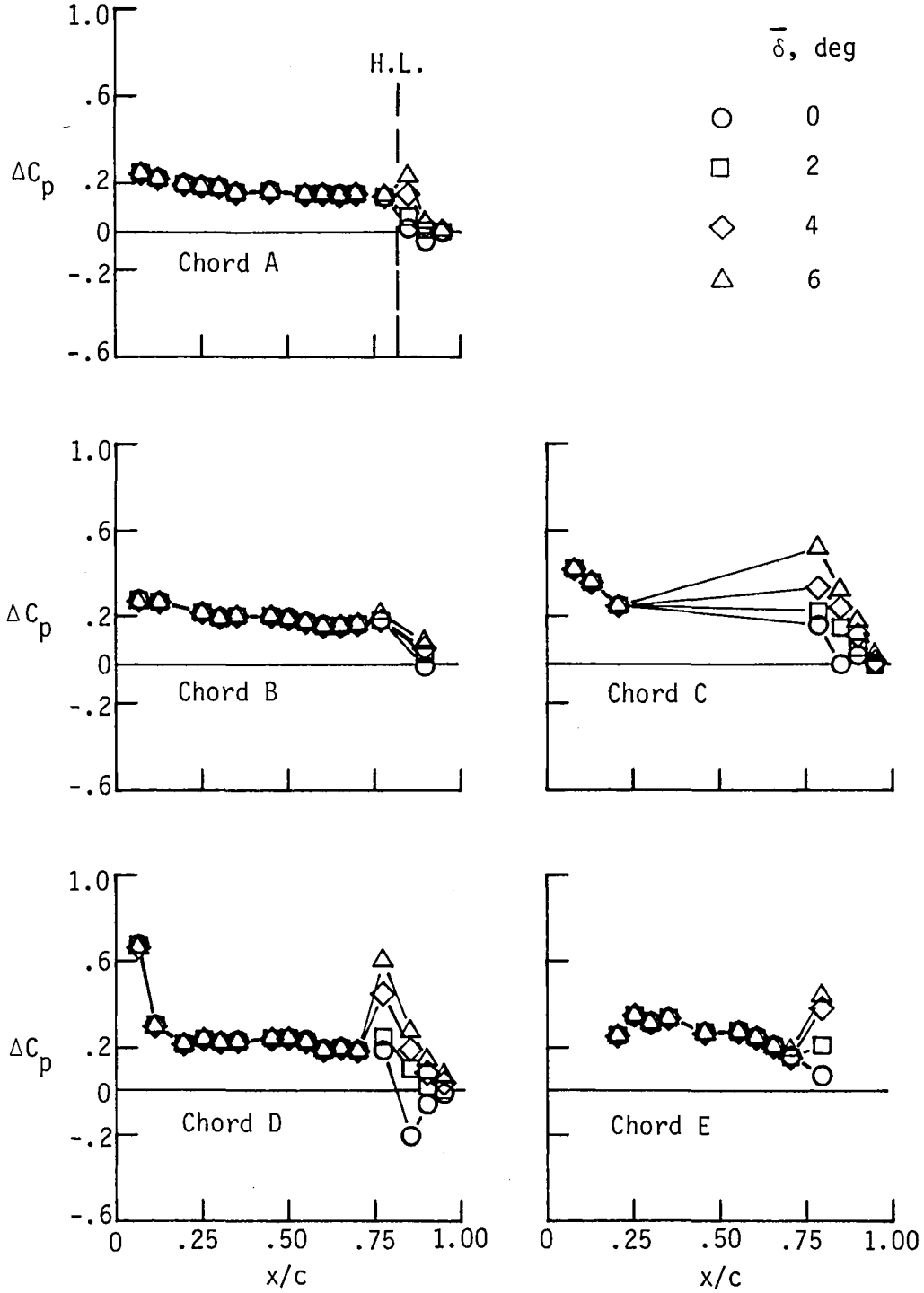

(d) $M = 0.94$.

Figure 22. Concluded.

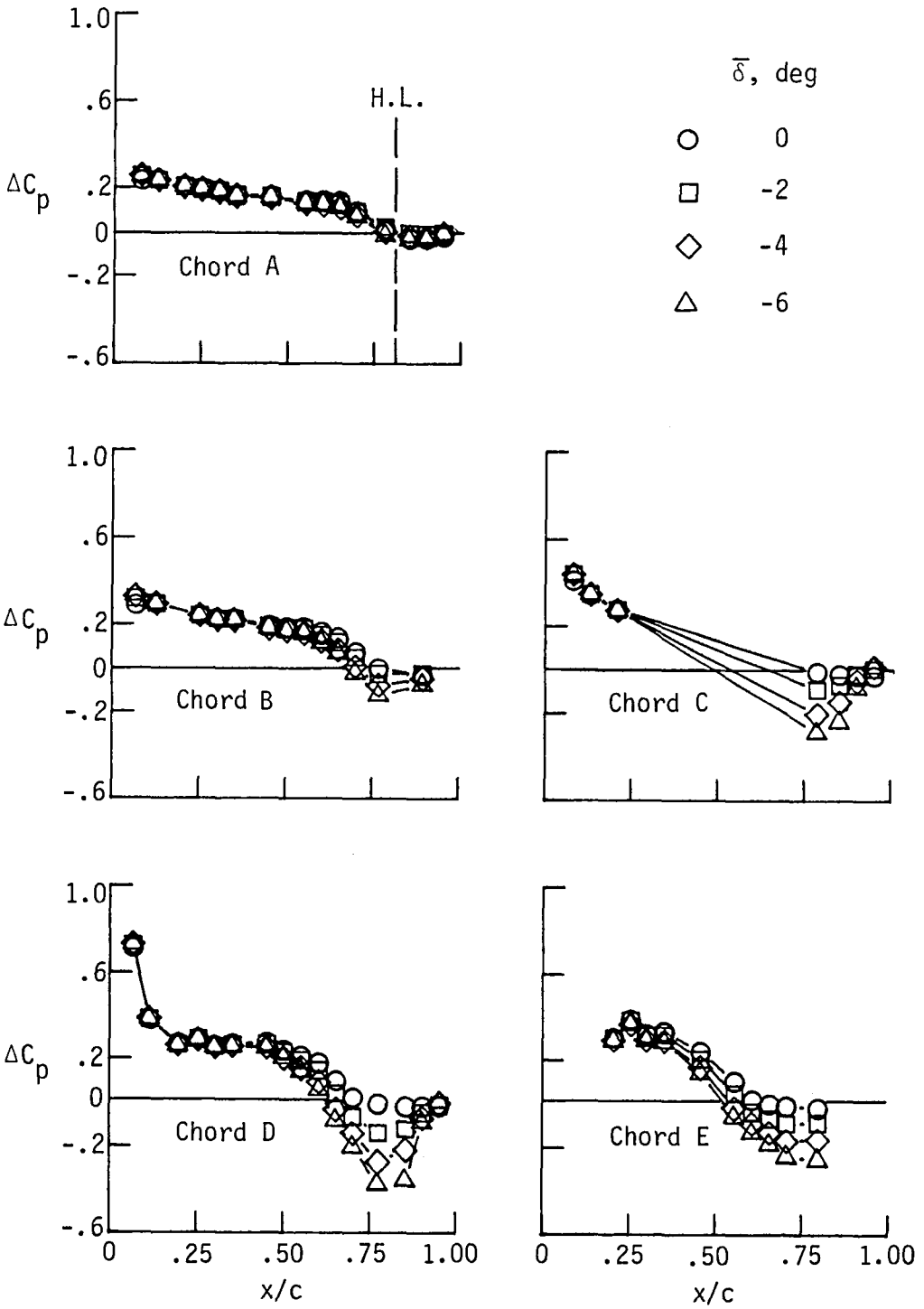

(a) $M = 0.88$.

Figure 23. Steady pressure distribution as a function of negative $\bar{\delta}$ at $\bar{\alpha} = 3°$.

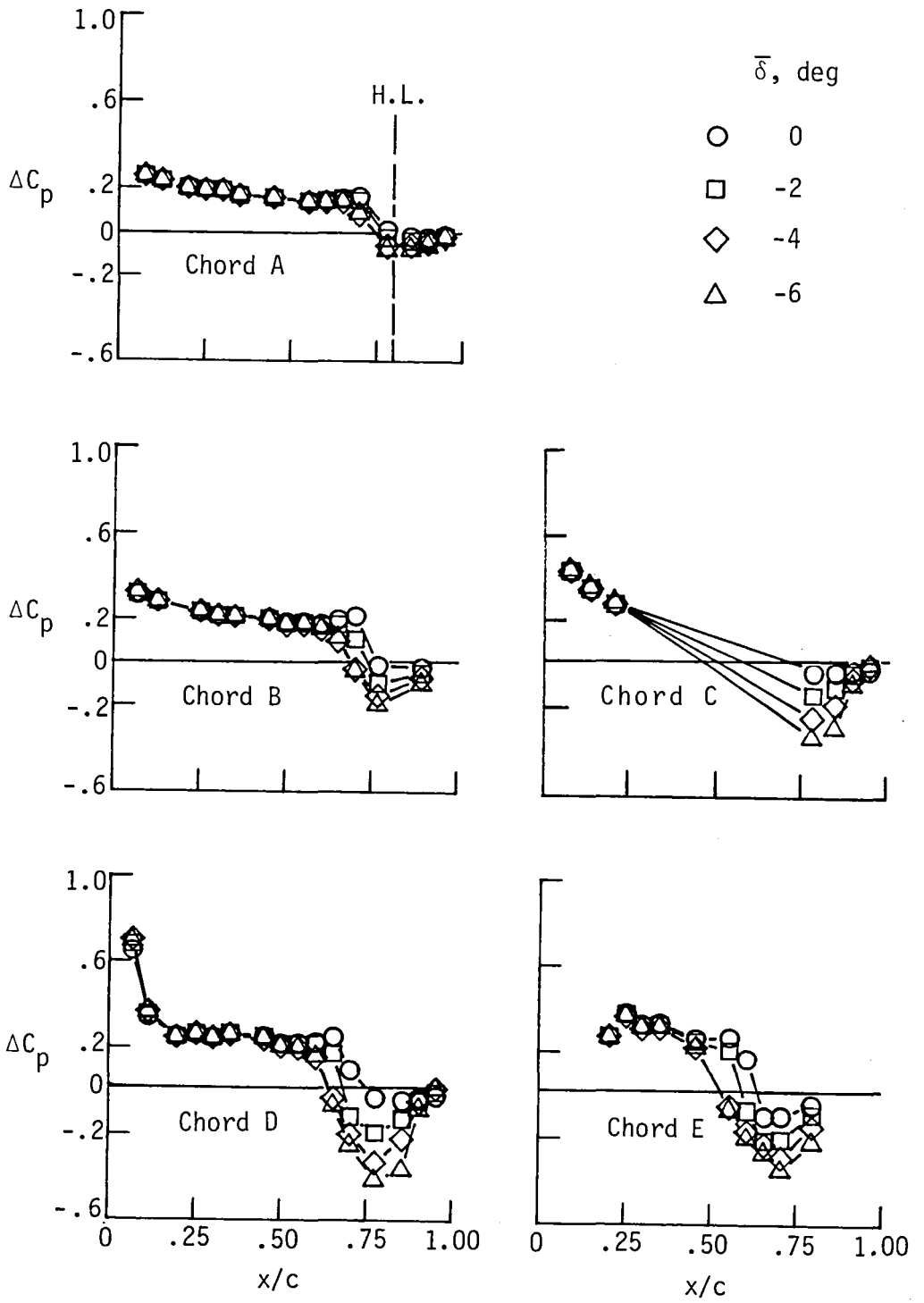

(b) $M = 0.90$.

Figure 23. Continued.

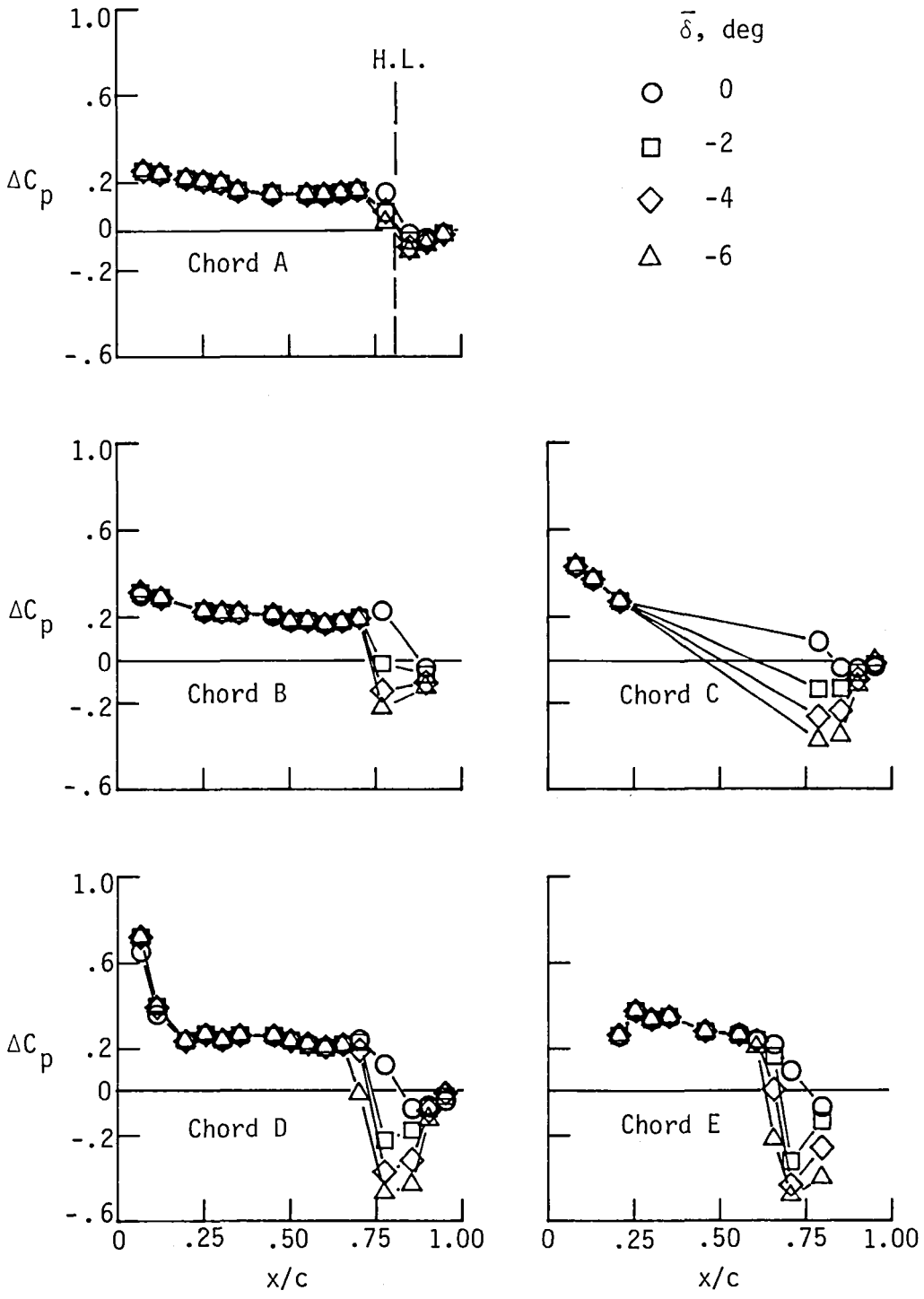

(c) $M = 0.92$.

Figure 23. Continued.

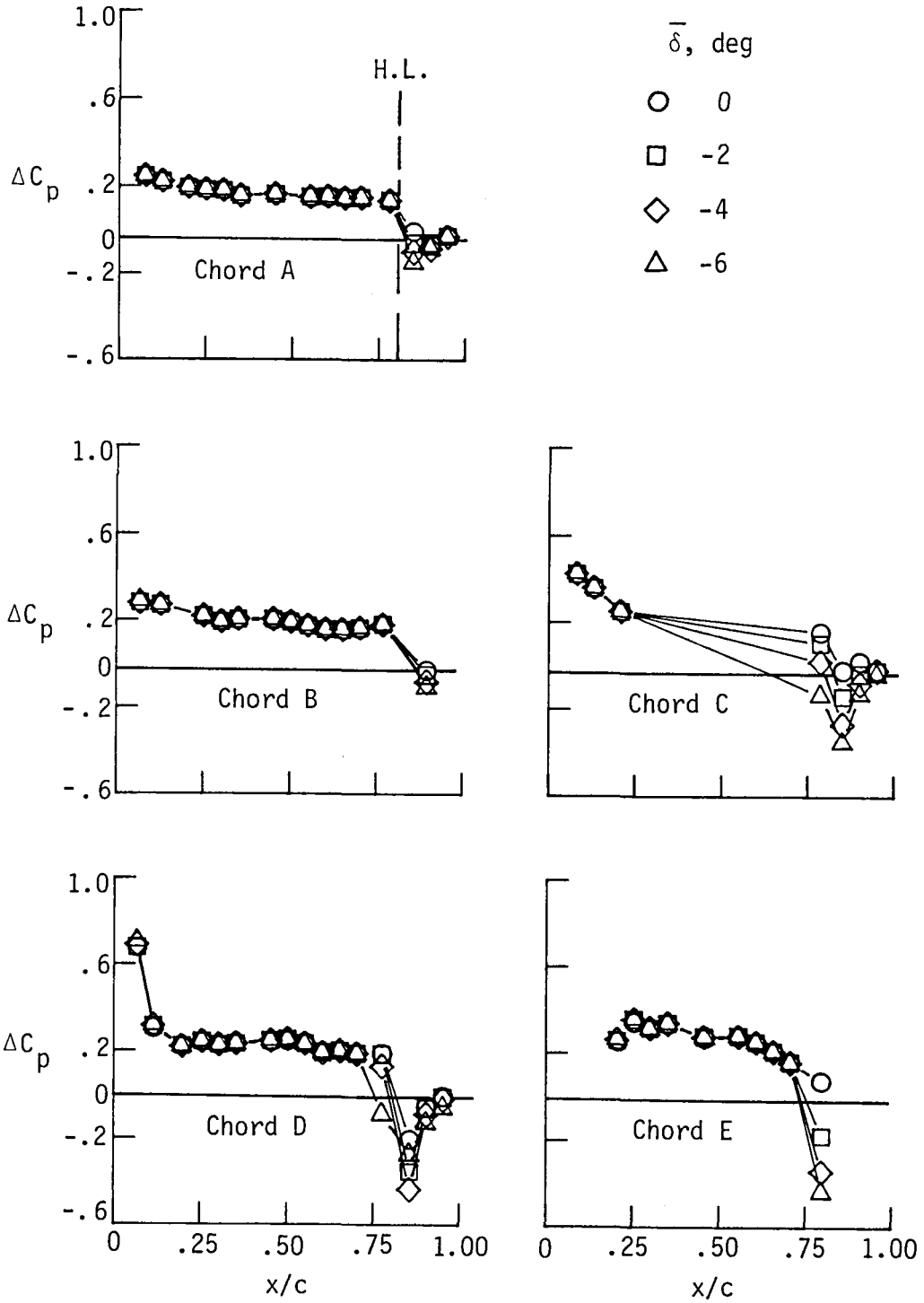

(d) $M = 0.94$.

Figure 23. Concluded.

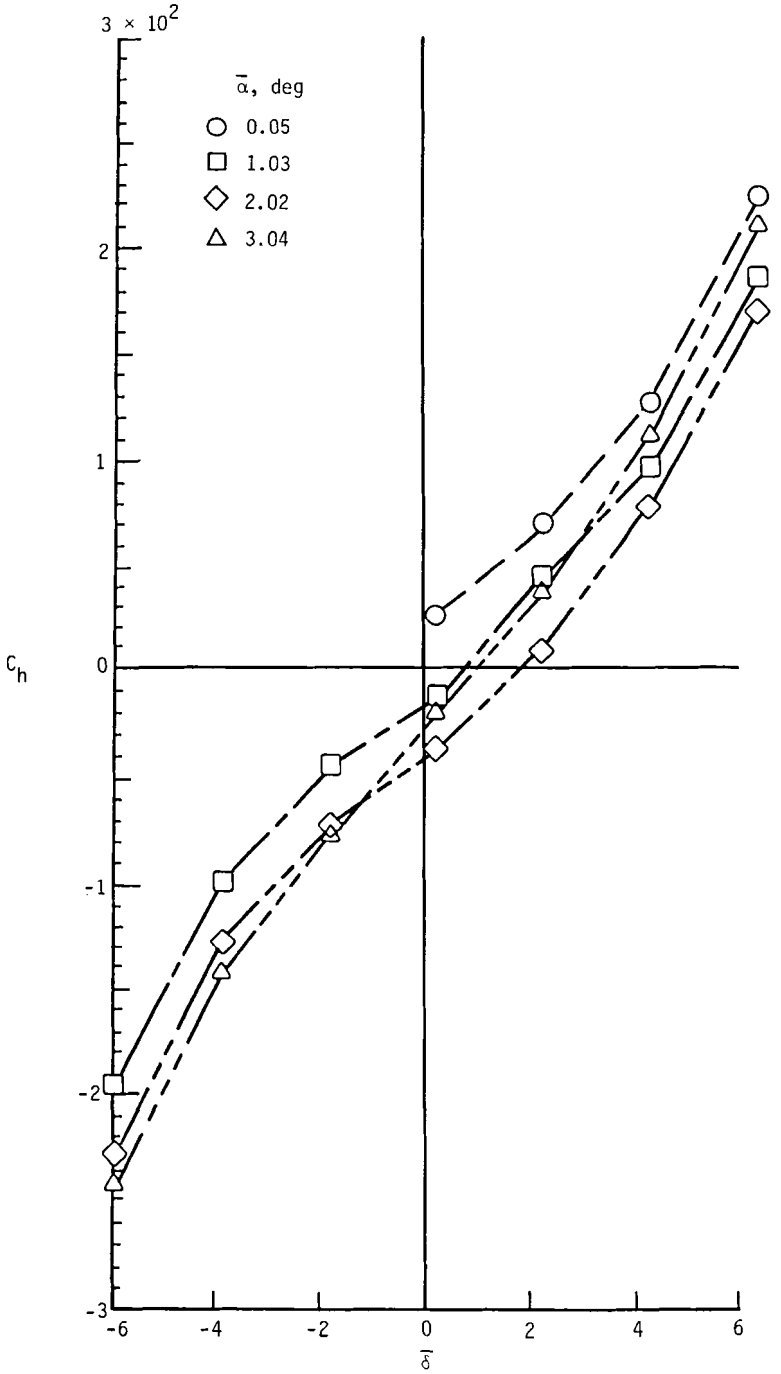

(a) $M = 0.88$.

Figure 24. Control-surface hinge moment as a function of $\bar{\delta}$ at angle of attack.

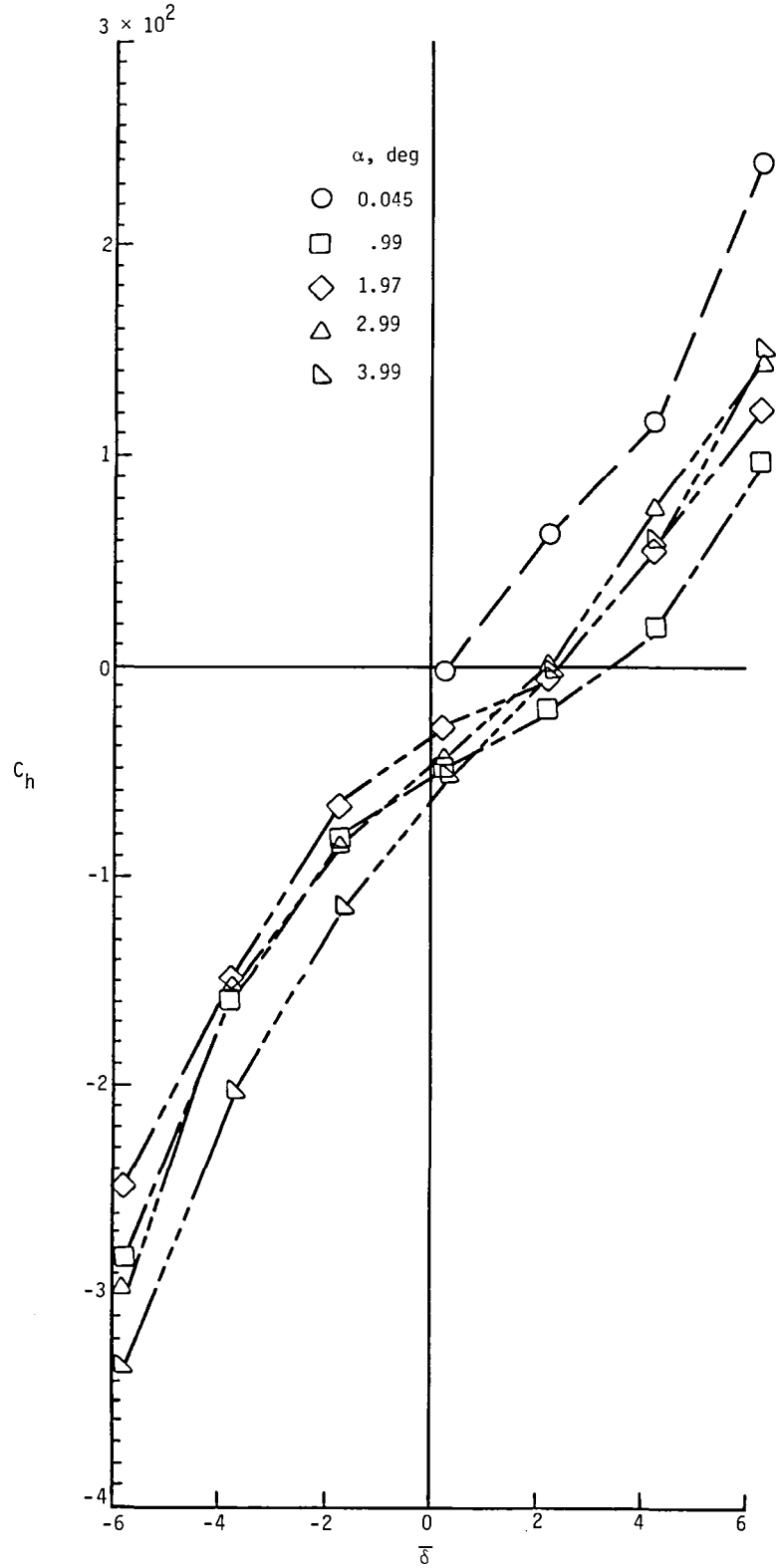

(b) $M = 0.90$.

Figure 24. Continued.

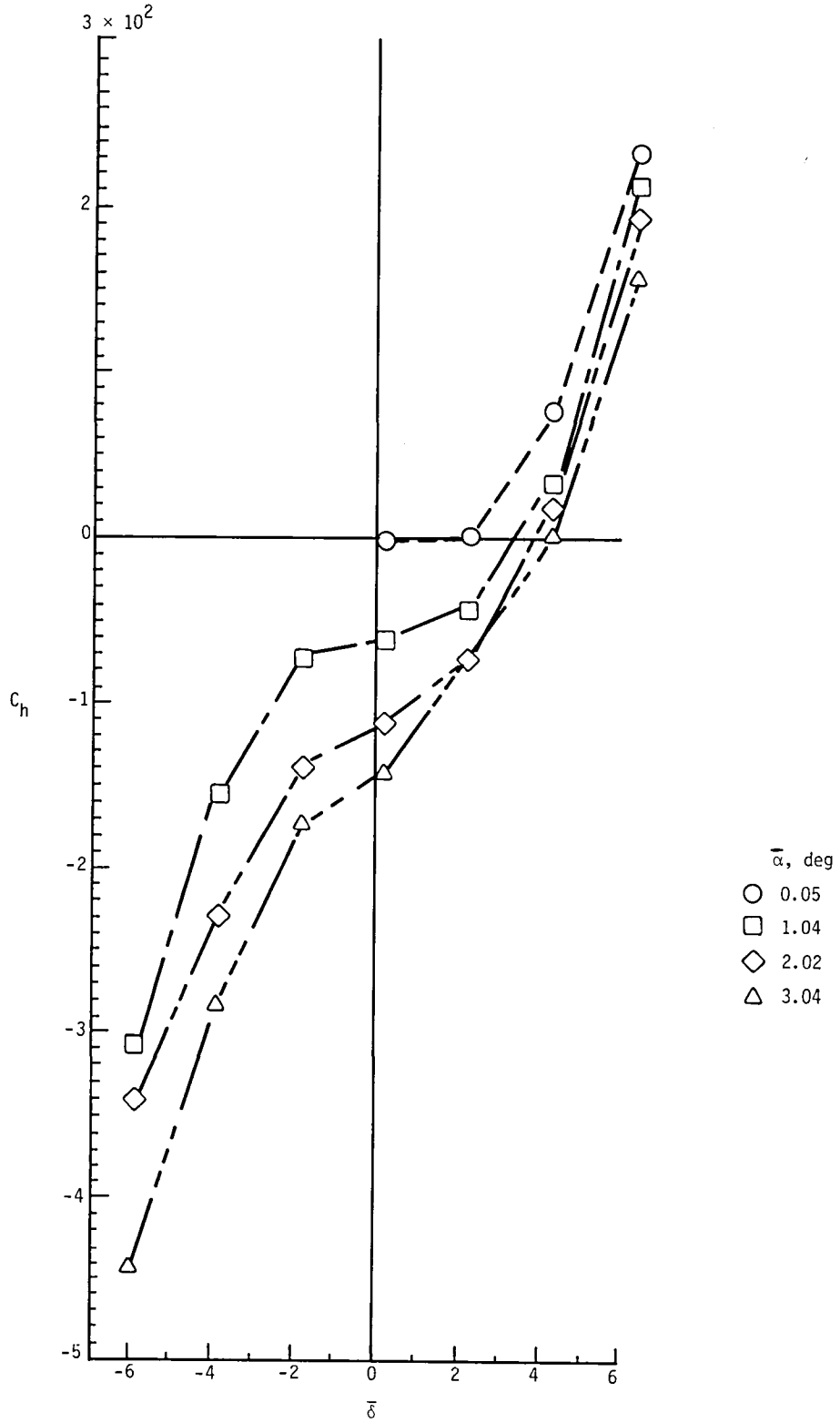

(c) $M = 0.92$.

Figure 24. Continued.

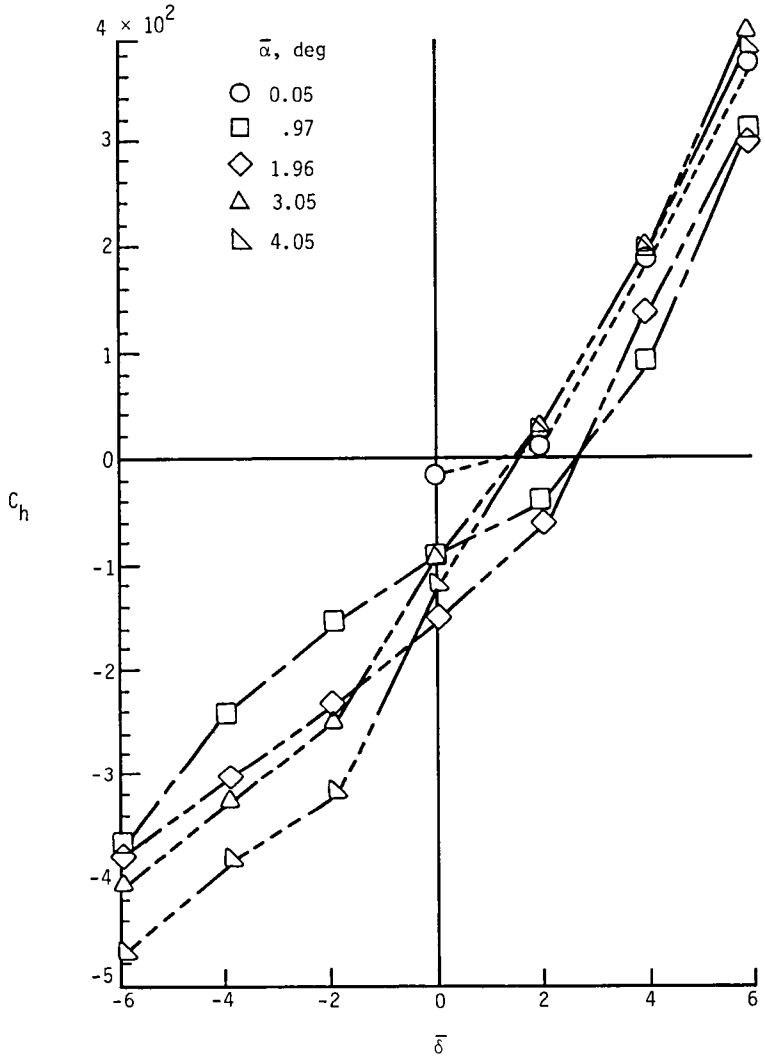

(d) $M = 0.94$.

Figure 24. Concluded.

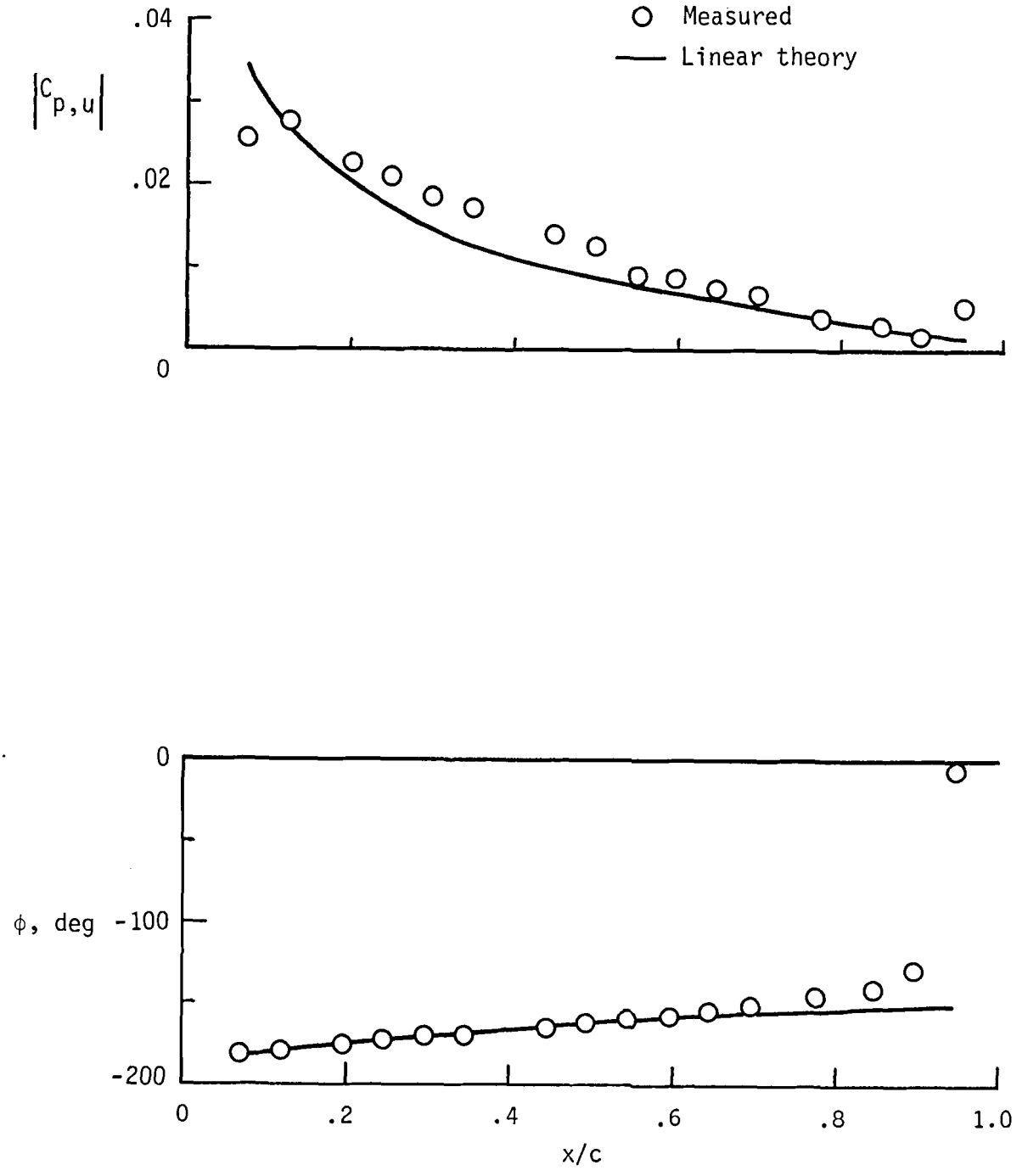

(a) $f = 4$ Hz.

Figure 25. Comparison of unsteady experimental pressures and phase angle with linear-theory results on chord D at $M = 0.40$, $\alpha = 0.47°$, and $\bar{\alpha} = 0.05°$ for wing pitch oscillation.

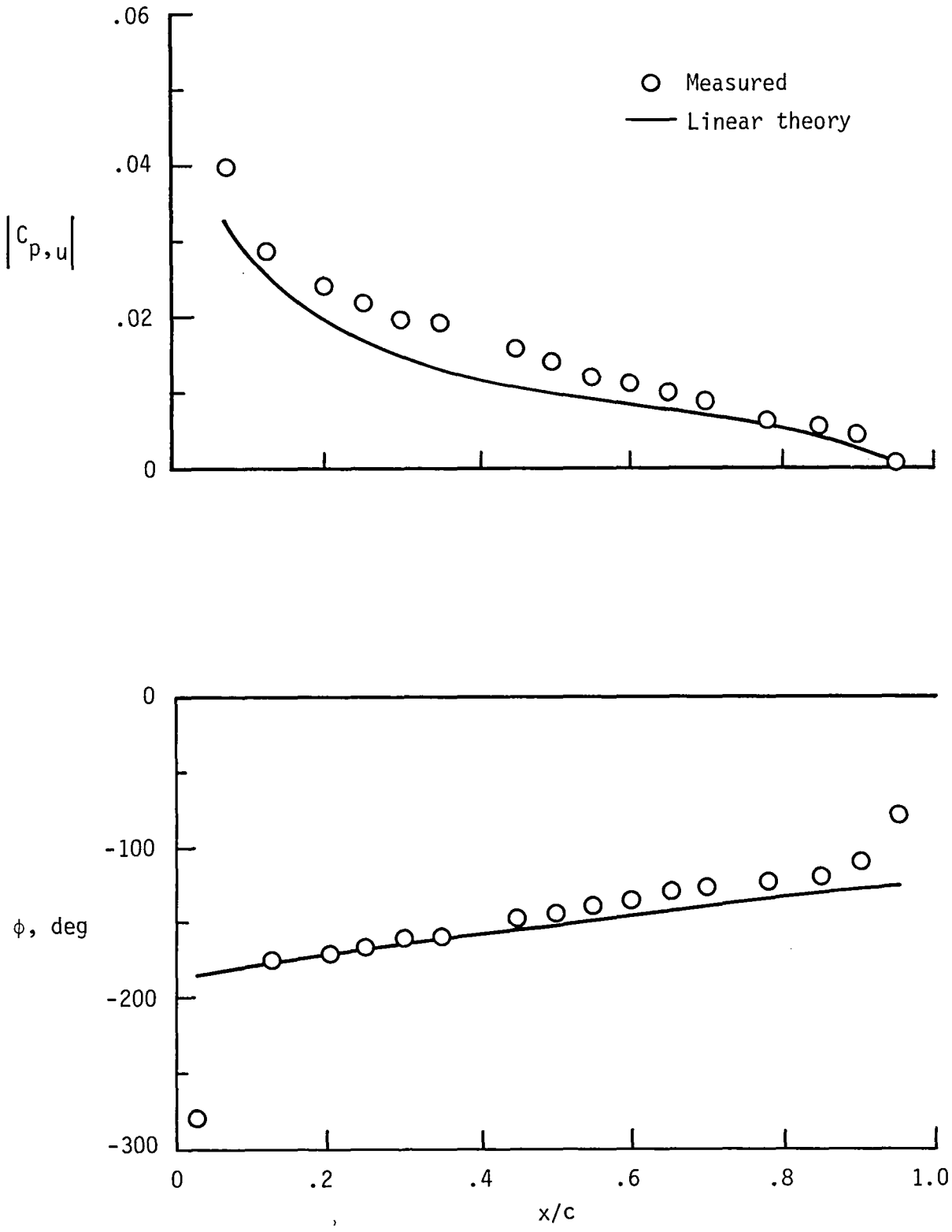

(b) $f = 8$ Hz.

Figure 25. Continued.

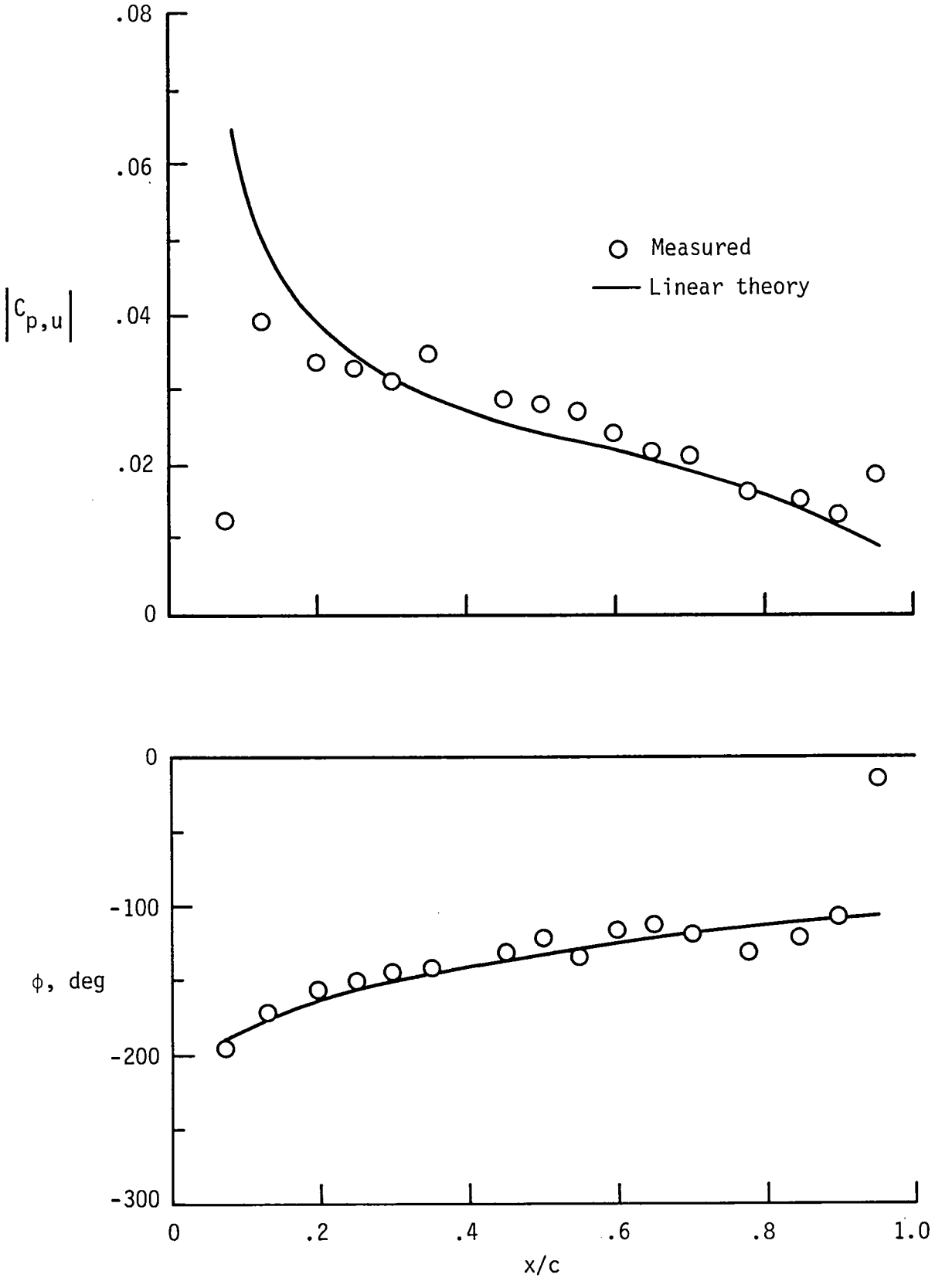

(c) $f = 16$ Hz.

Figure 25. Concluded.

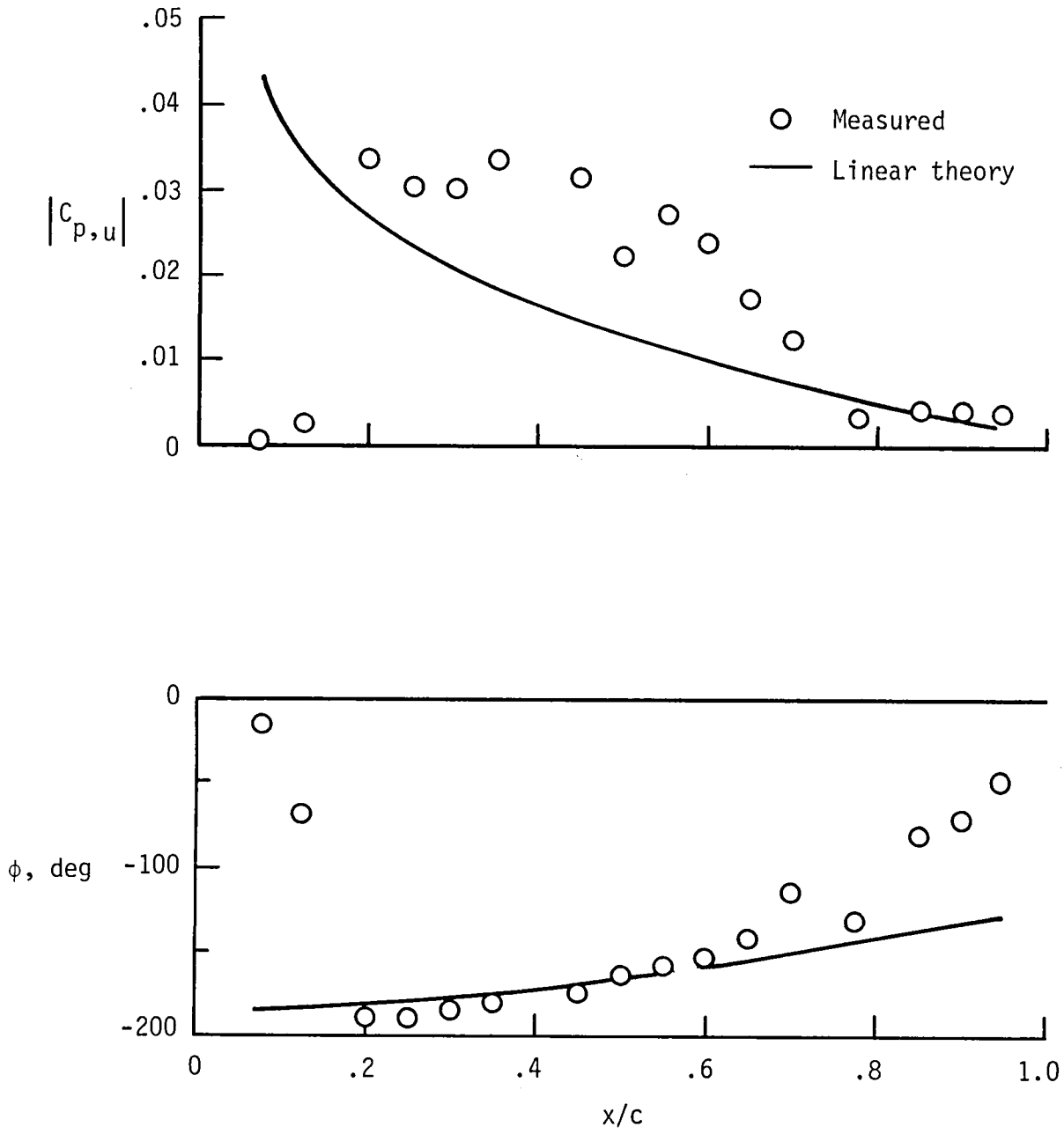

Figure 26. Comparison of unsteady experimental pressure and phase angle with linear-theory results on chord D for wing pitch oscillation at $M = 0.885$, $\bar{\alpha} = 0.05°$, and $\alpha = 0.48°$, and $f = 8$ Hz.

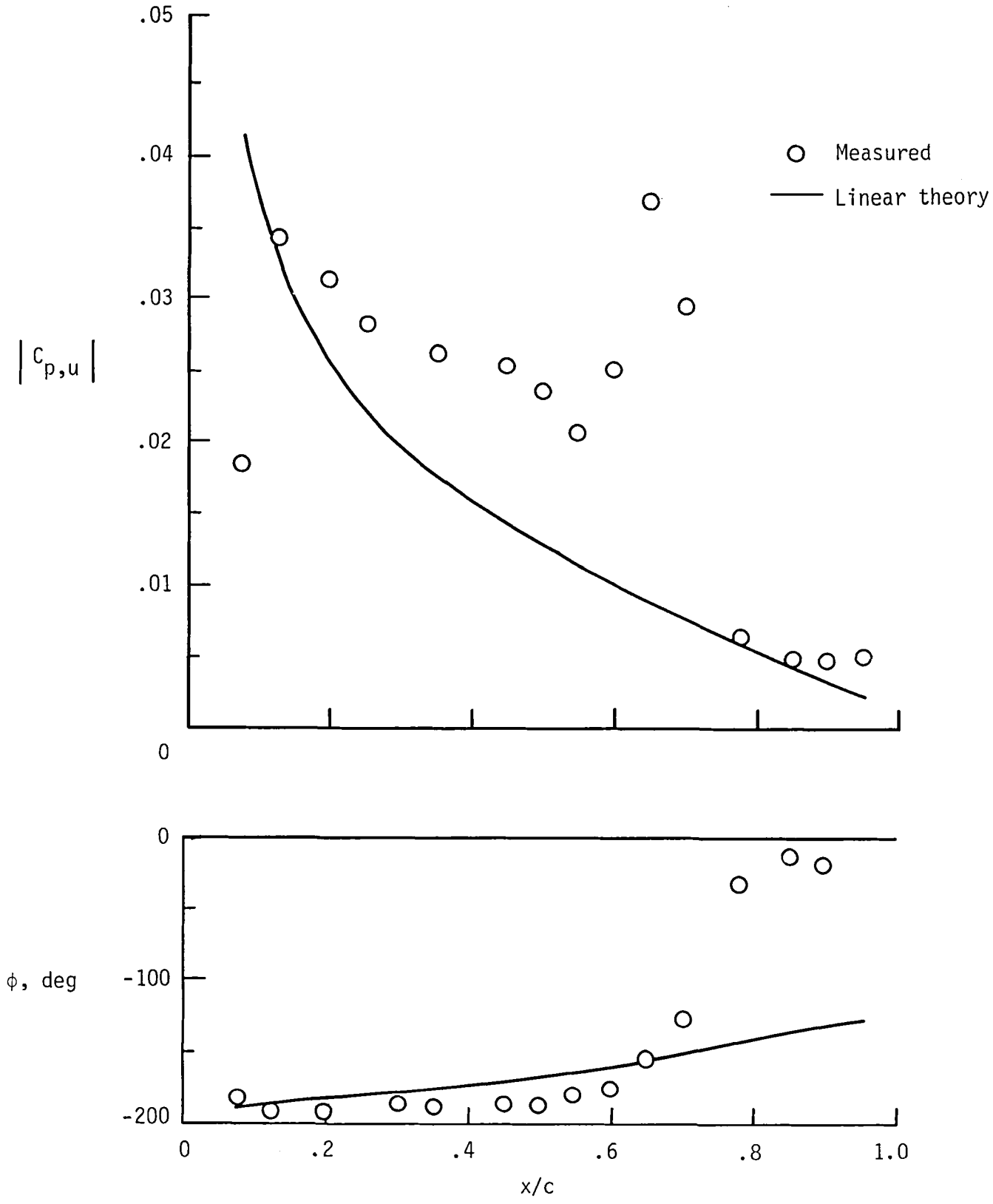

(a) $f = 8$ Hz.

Figure 27. Comparison of unsteady experimental pressure and phase angle with linear-theory results on chord D for wing pitch oscillations at $M = 0.90$, $\bar{\alpha} = 0°$, and $\alpha = 0.46°$.

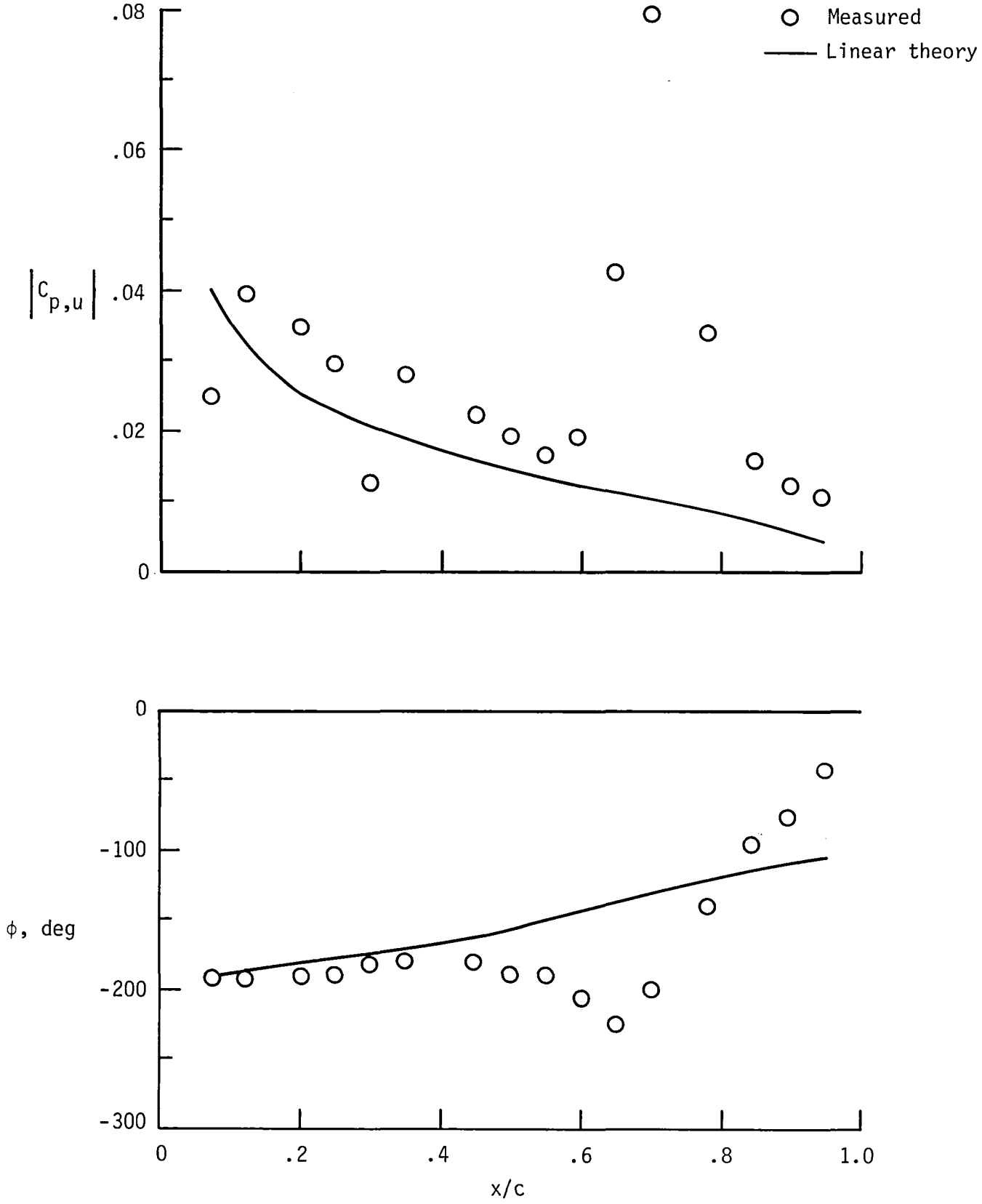

(b) $f = 16$ Hz.

Figure 27. Concluded.

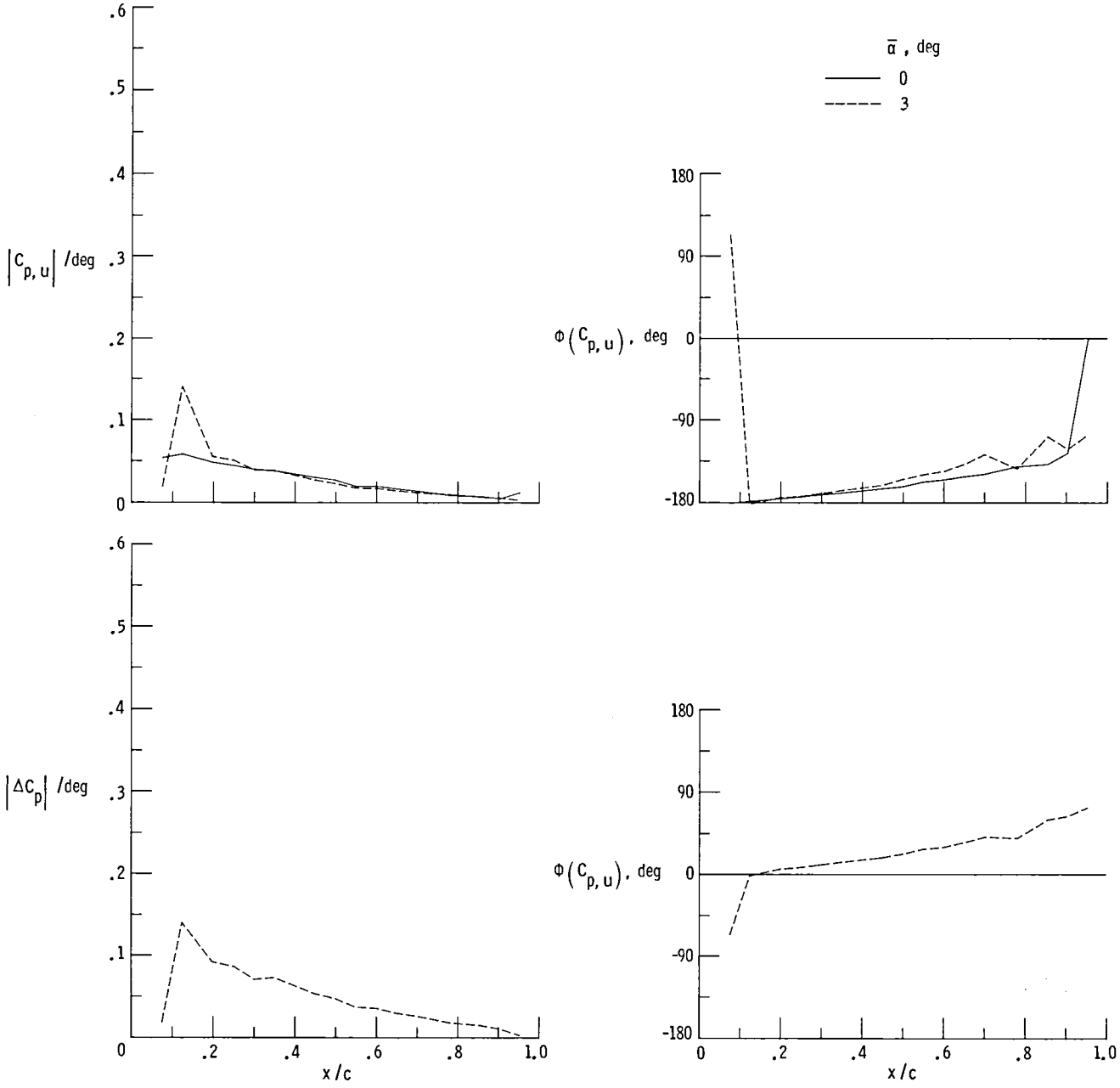

(a) $\bar{\alpha} = 0°$ and $3°$; $f = 4$ Hz.

Figure 28. Unsteady pressure distributions and phase angle on chord D for wing pitch oscillation at $M = 0.40$ and $\alpha = 0.46°$.

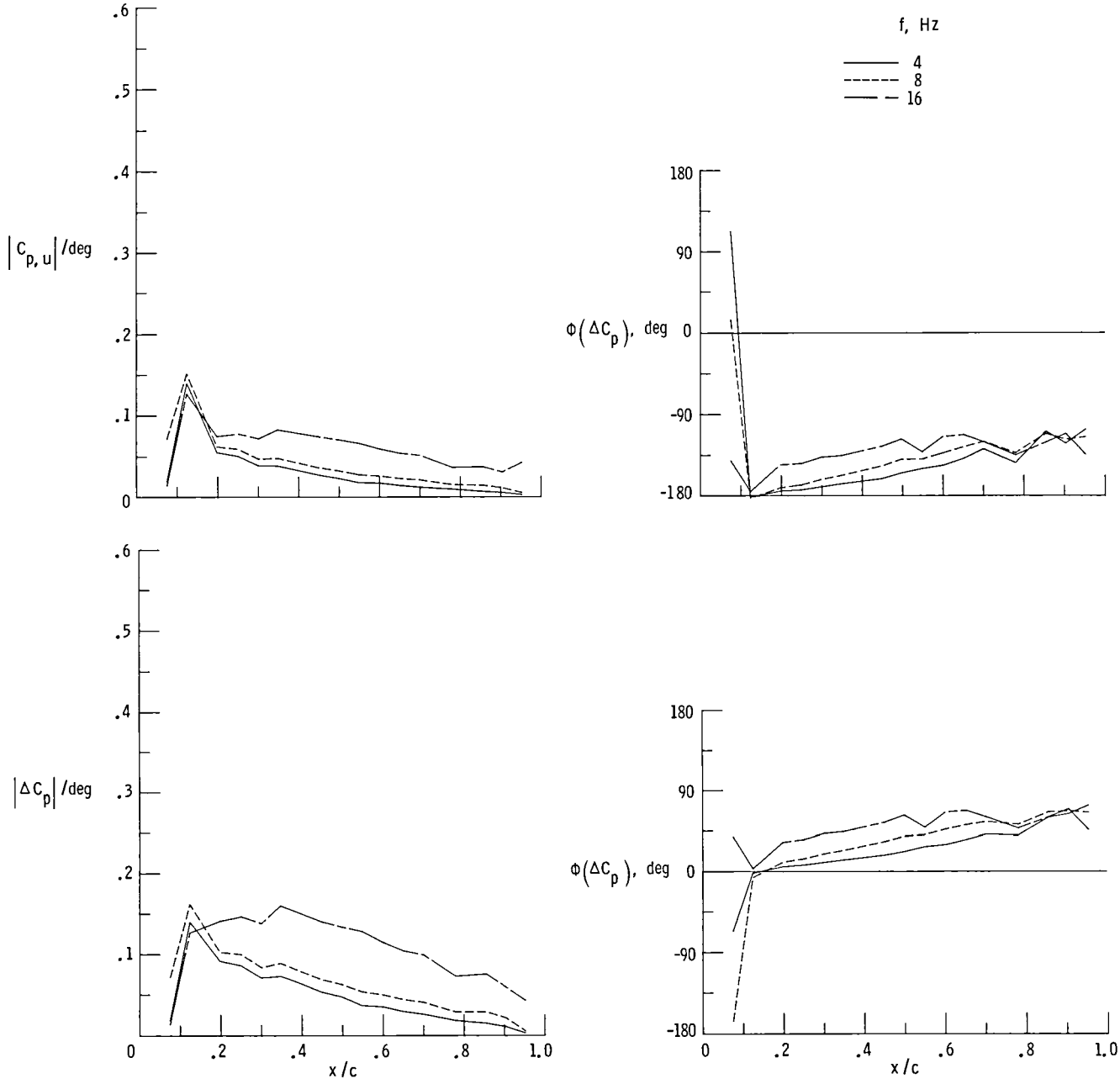

(b) $\bar{\alpha} = 3°$; $f = 4$, 8, and 16 Hz.

Figure 28. Concluded.

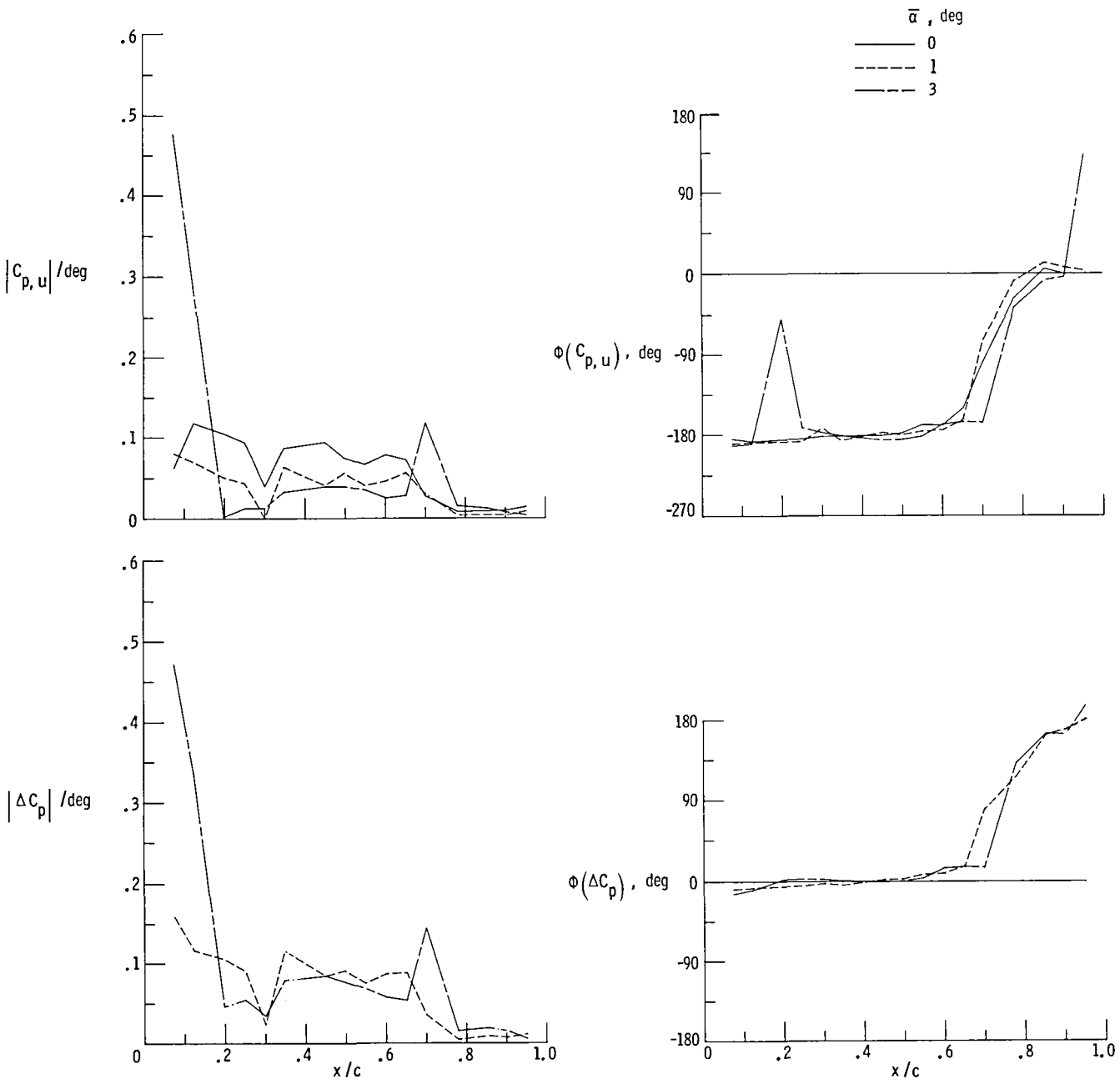

(a) $f = 4$ Hz.

Figure 29. Unsteady pressure distributions and phase angle on chord D for wing pitch oscillation at three values of $\bar{\alpha}$ for $M = 0.90$ and $\alpha = 0.46°$.

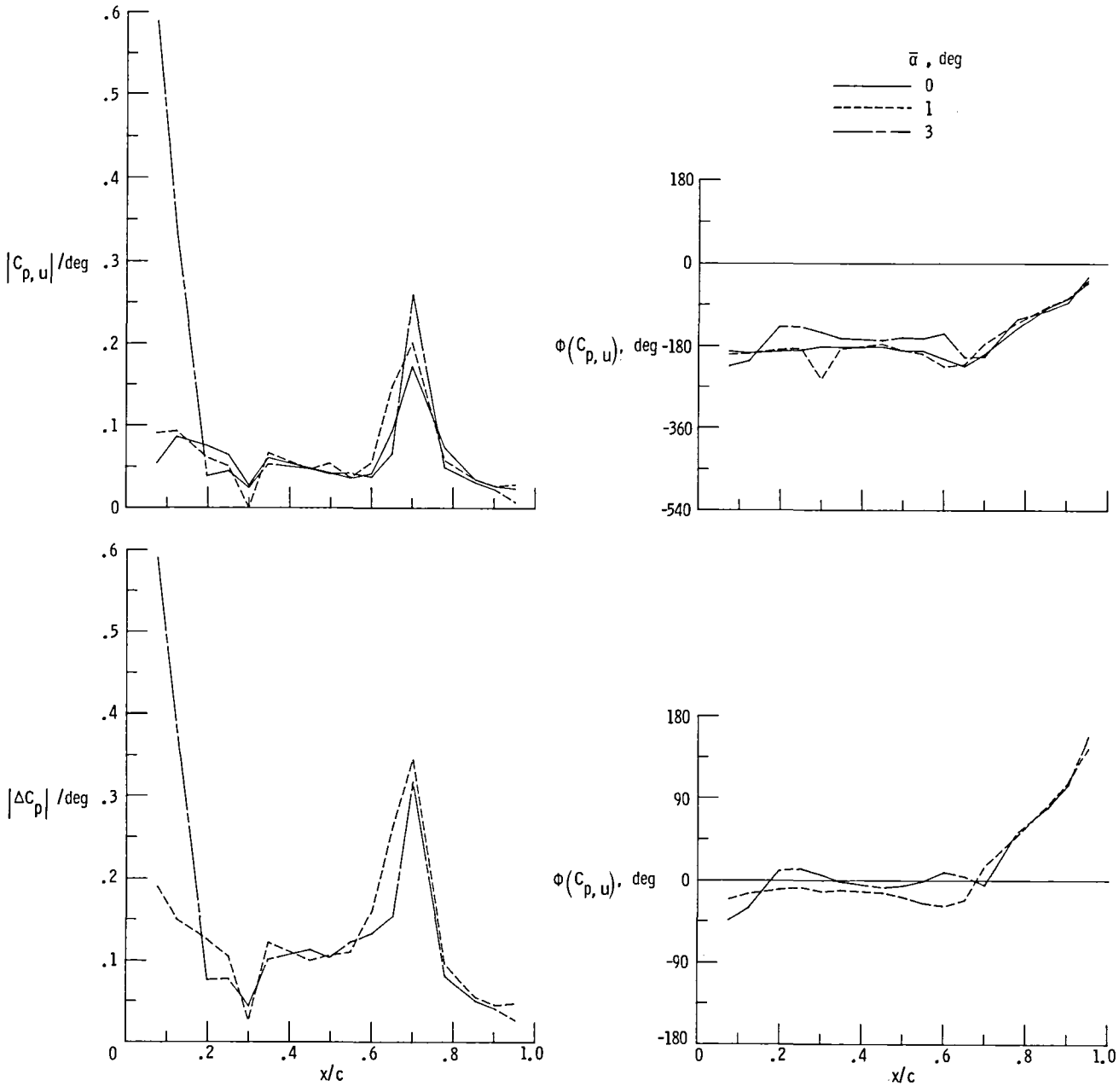

(b) $f = 16$ Hz.

Figure 29. Concluded.

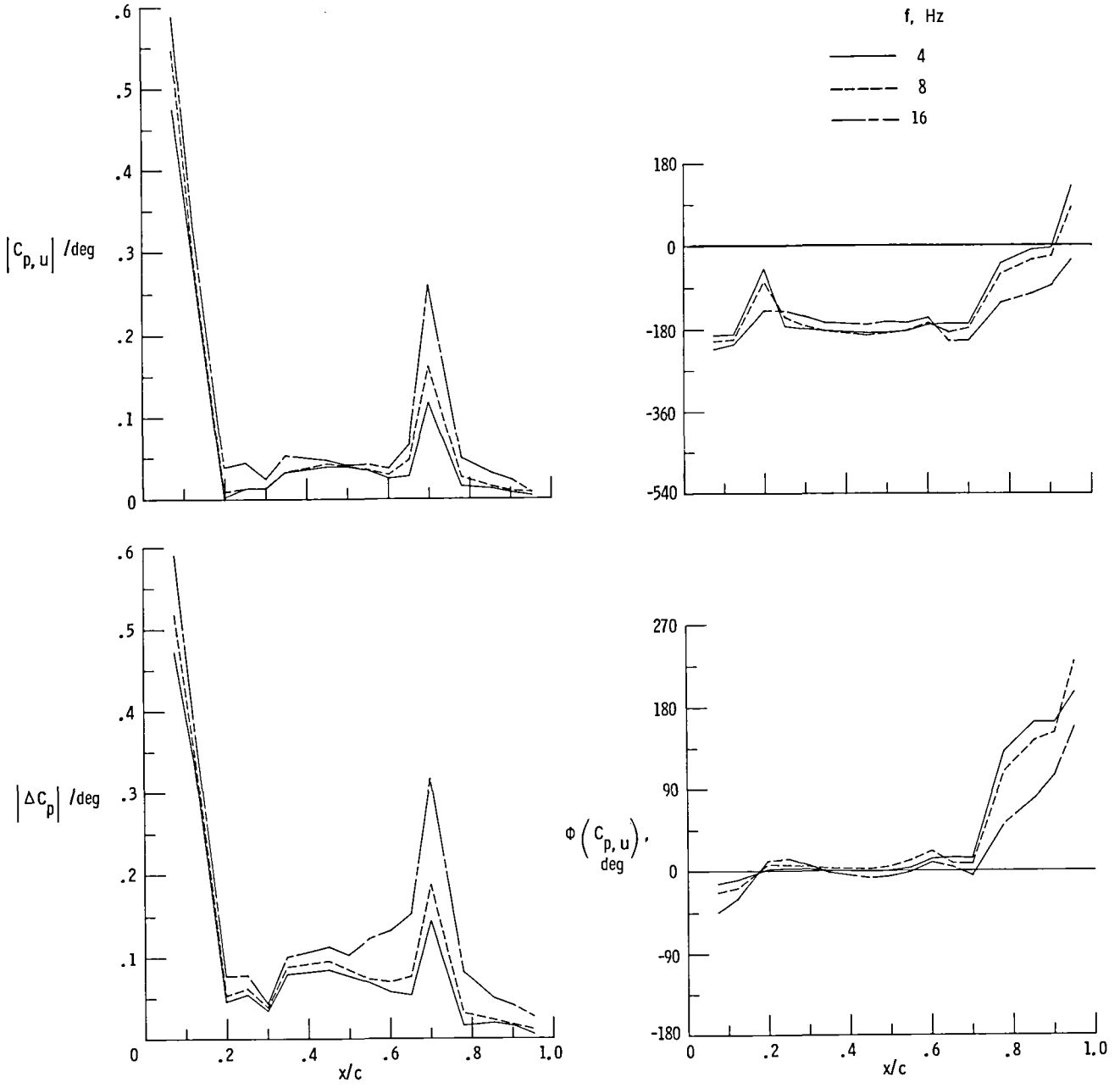

Figure 30. Unsteady pressure distributions and phase angle on chord D for wing pitch oscillation at $f = 4$, 8, and 16 Hz at $M = 0.90$, $\bar{\alpha} = 3°$, and $\alpha = 0.46°$.

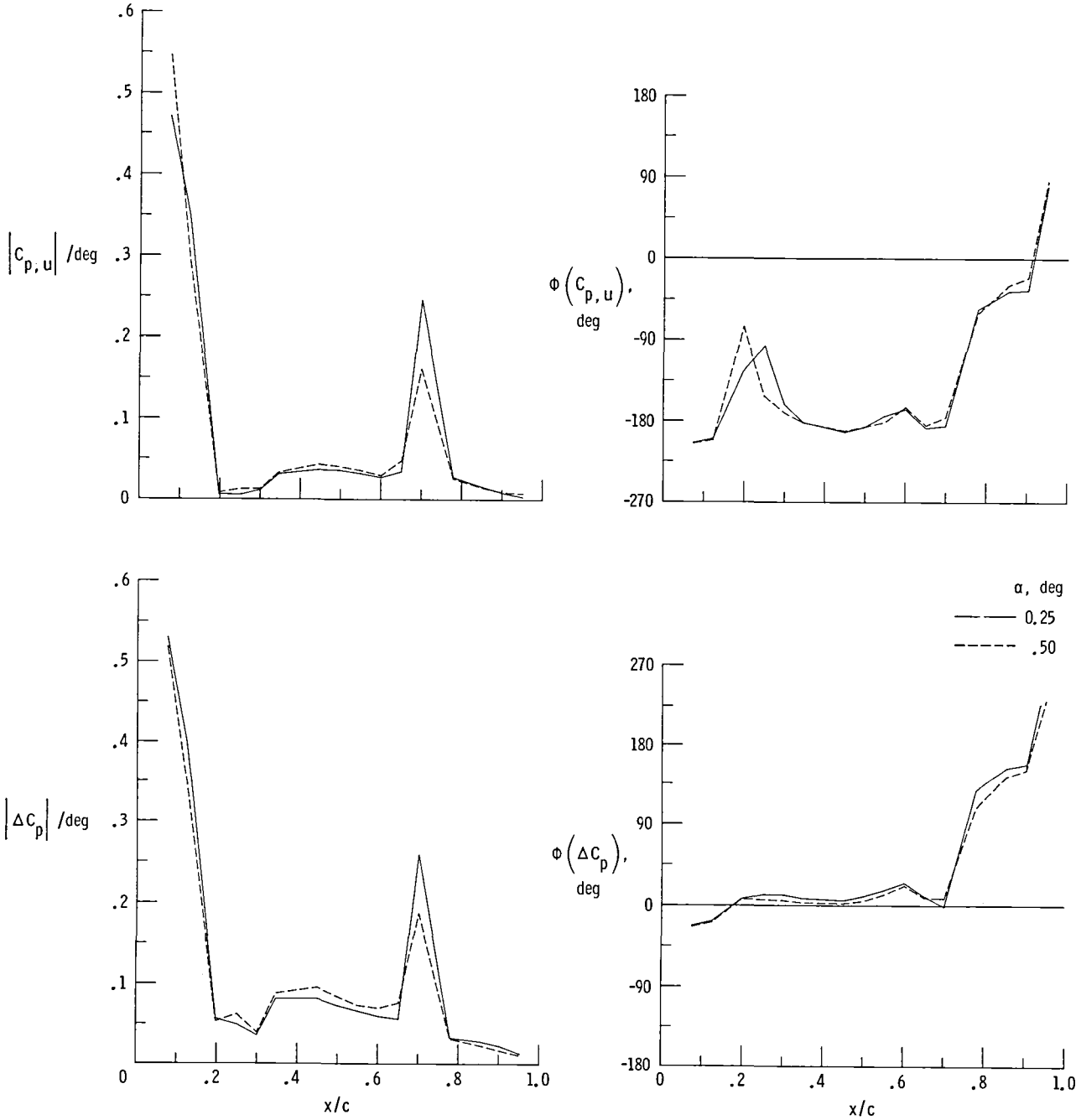

Figure 31. Unsteady pressure distributions and phase angle on chord D for wing pitch oscillation at $\alpha = 0.25°$ and $0.50°$, $M = 0.90$, $\bar{\alpha} = 3°$, and $f = 8$ Hz.

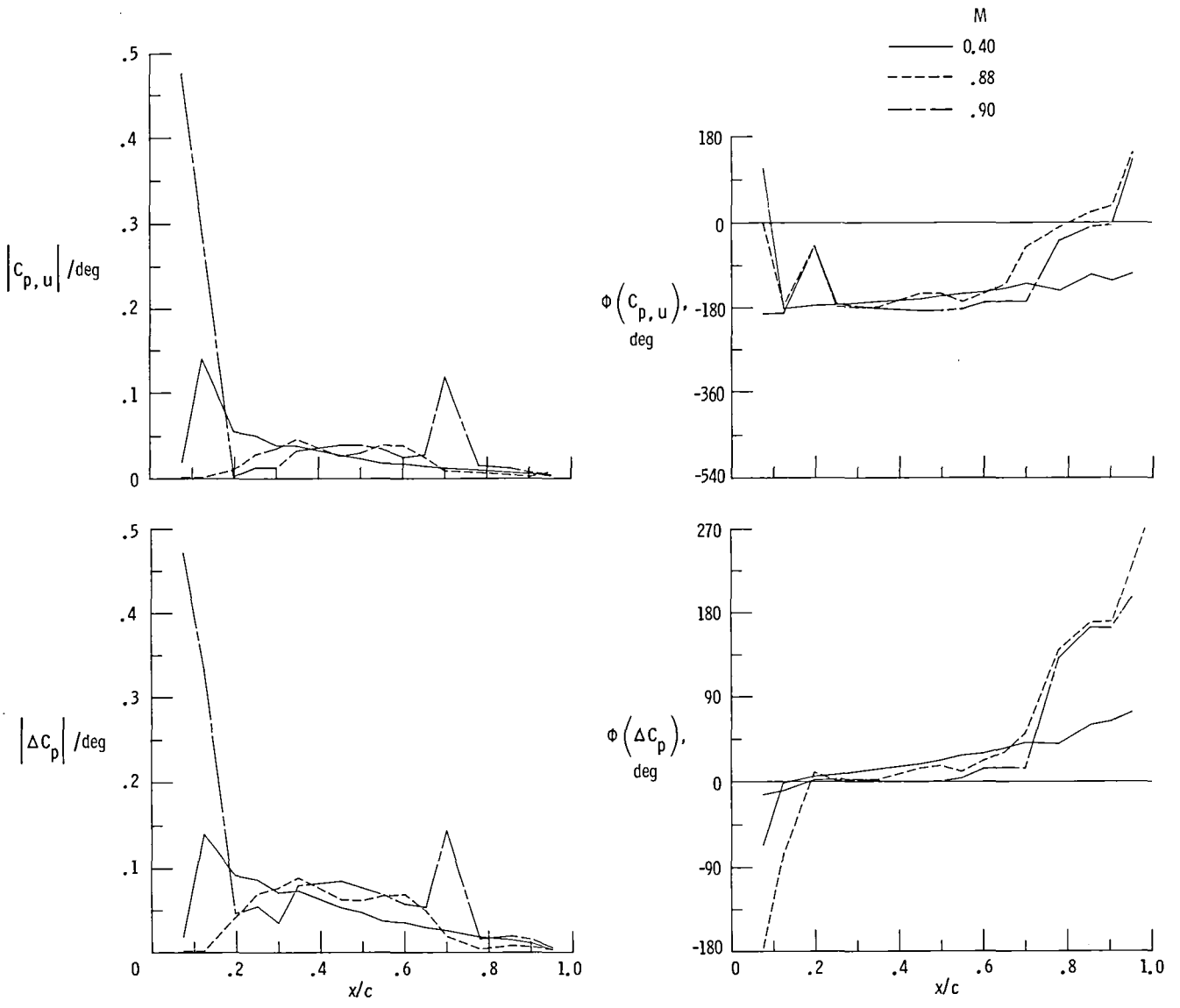

(a) $\alpha = 0.46°$; $f = 4$ Hz.

Figure 32. Unsteady pressure distributions and phase angle on chord D for wing pitch oscillation at $\bar{\alpha} = 3°$.

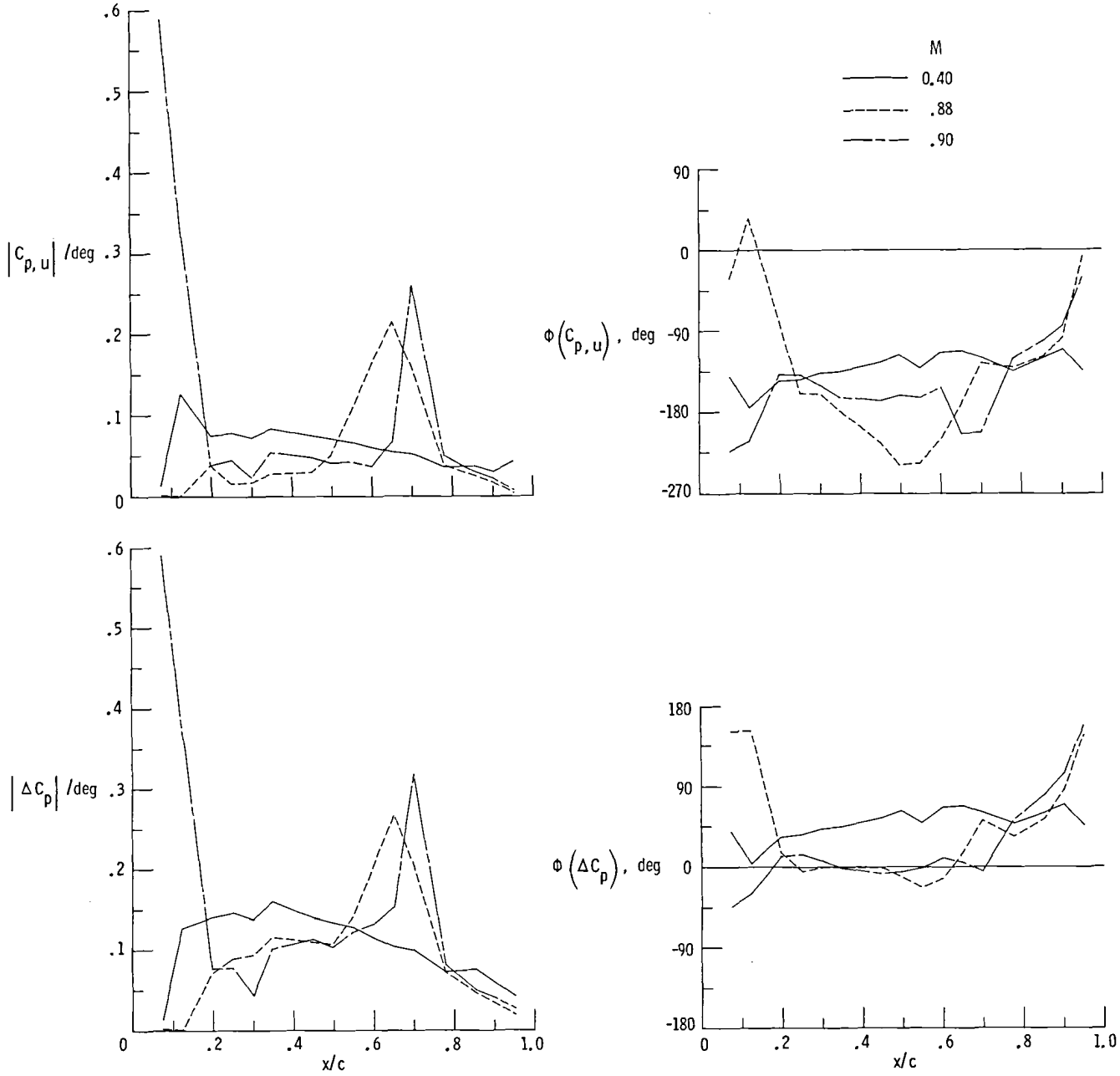

(b) $\alpha = 0.50°$; $f = 16$ Hz.

Figure 32. Concluded.

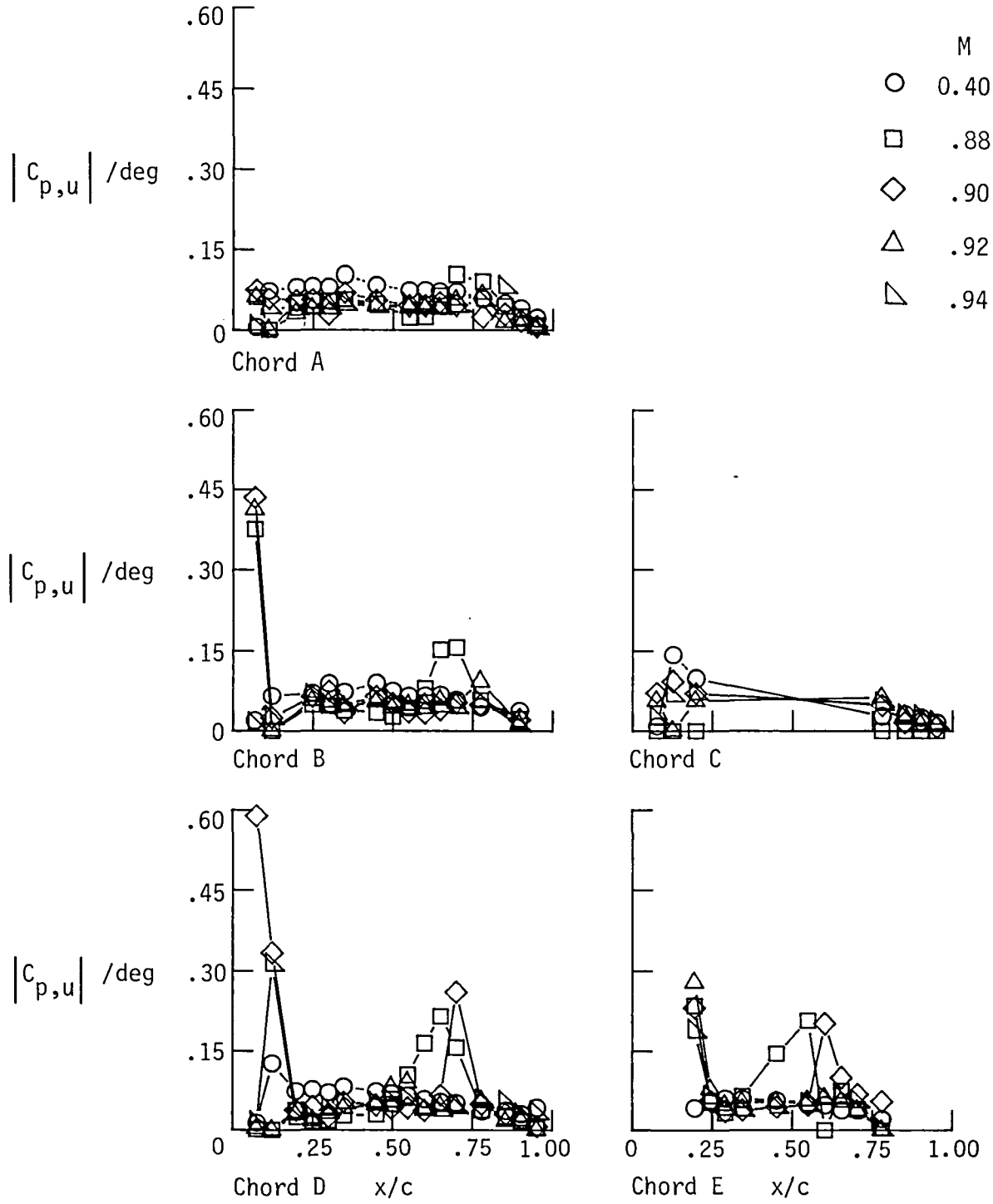

(a) $|C_{p,u}|$/deg.

Figure 33. Unsteady pressure distributions and phase angle on five chords for wing pitch oscillation at $\bar{\alpha} = 3°$, $\alpha = 0.50°$, and $f = 16$ Hz.

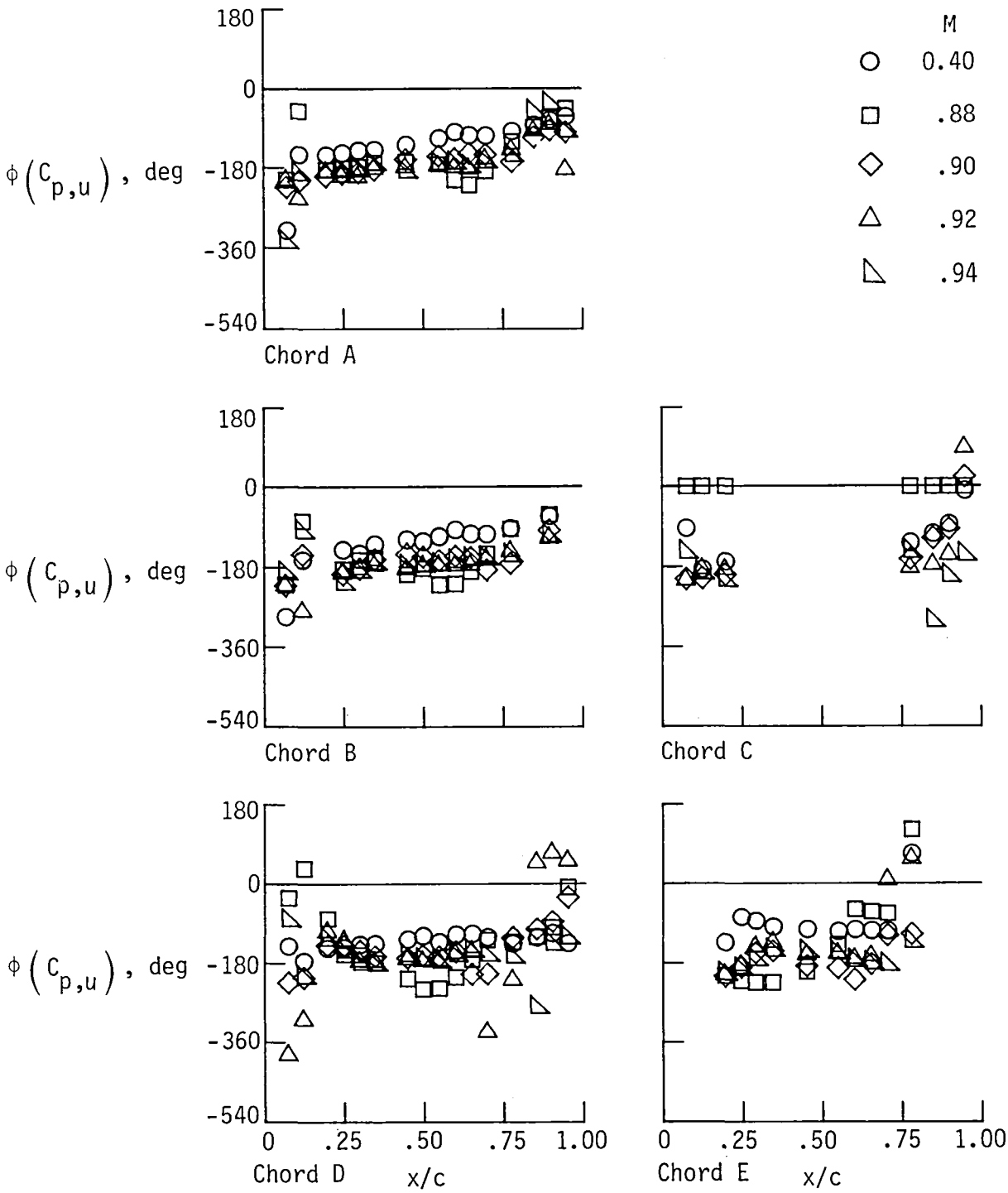

(b) $\phi(C_{p,u})$.

Figure 33. Continued.

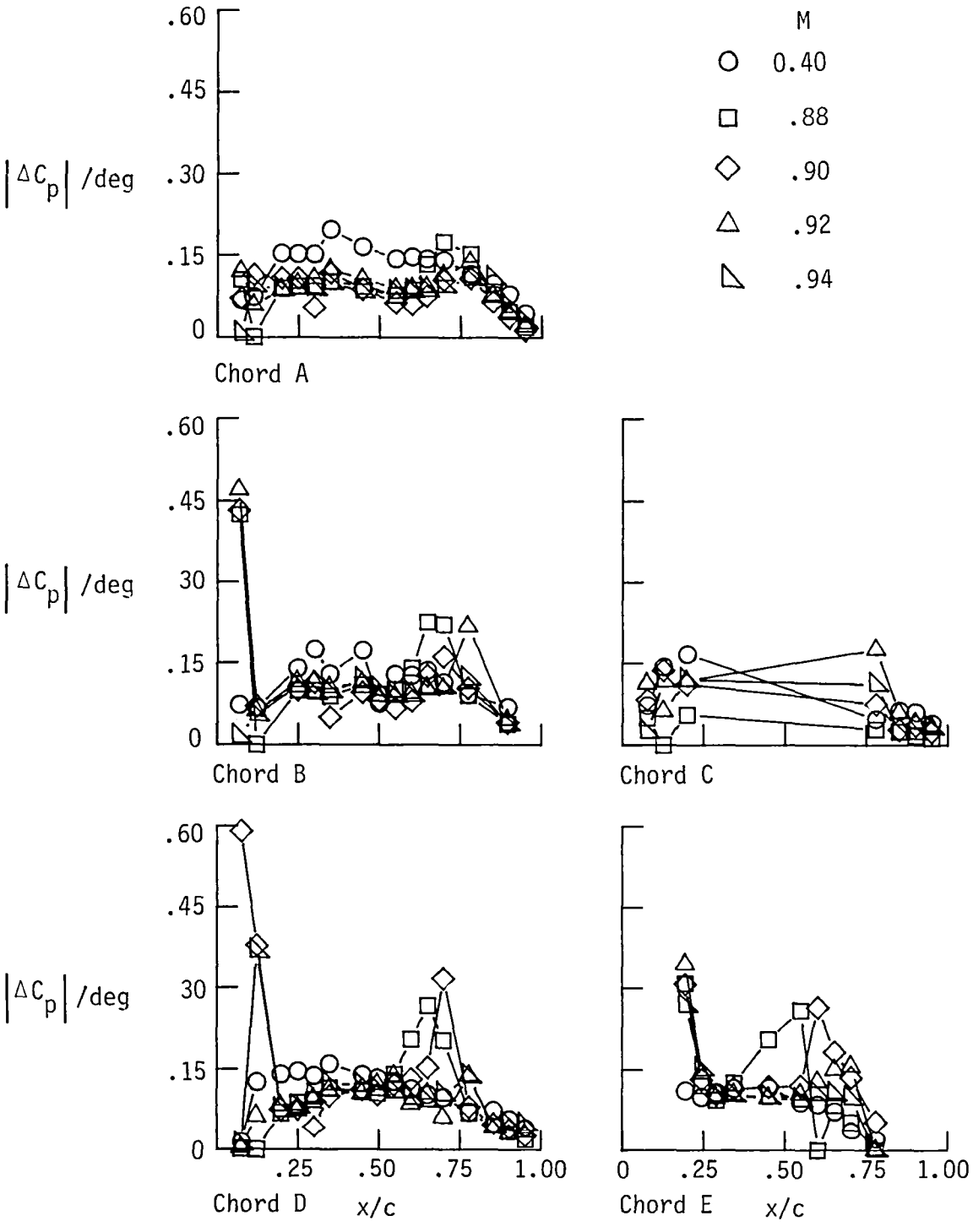

(c) $|\Delta C_p|$/deg.

Figure 33. Continued.

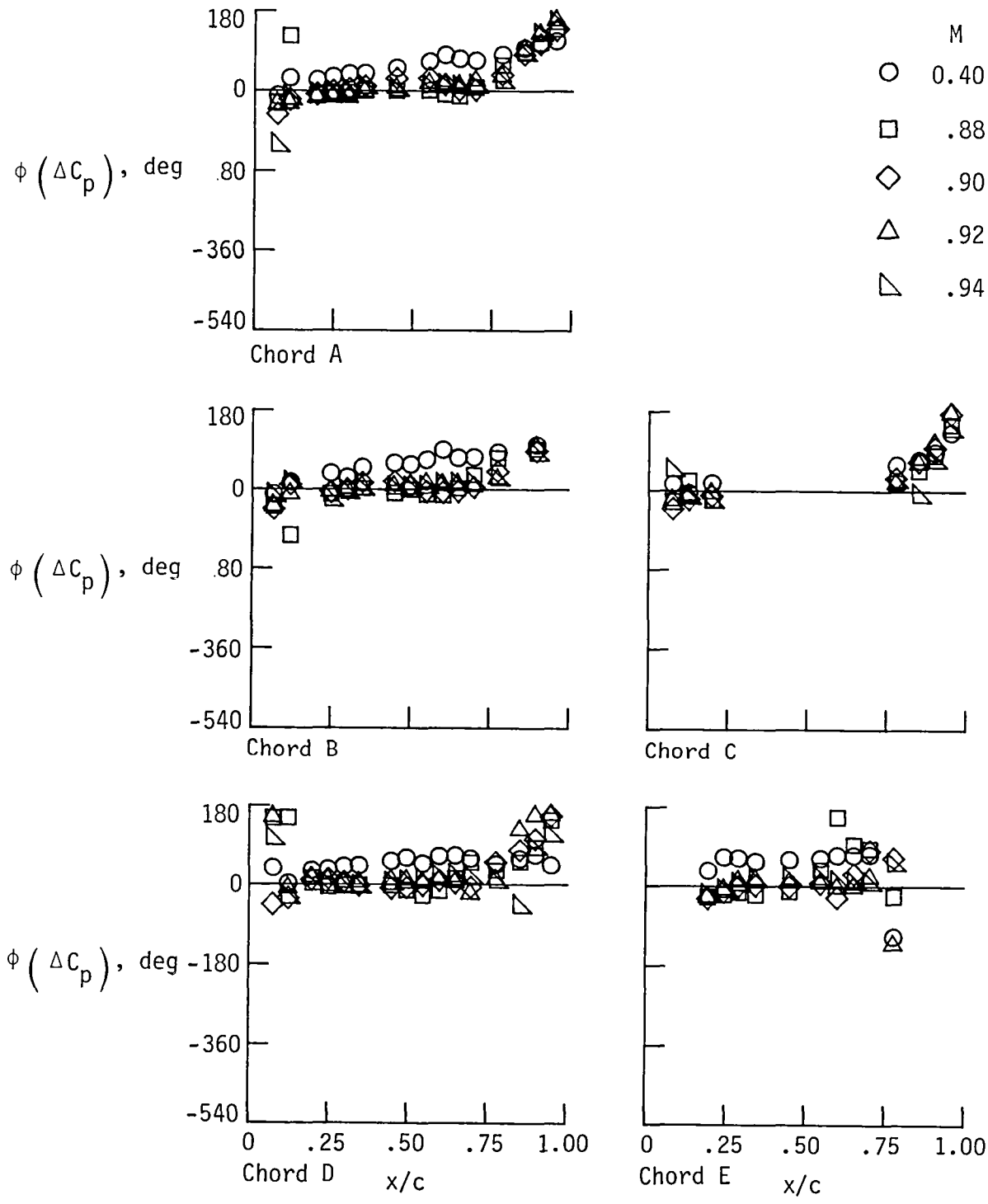

(d) $\phi(\Delta C_p)$.

Figure 33. Concluded.

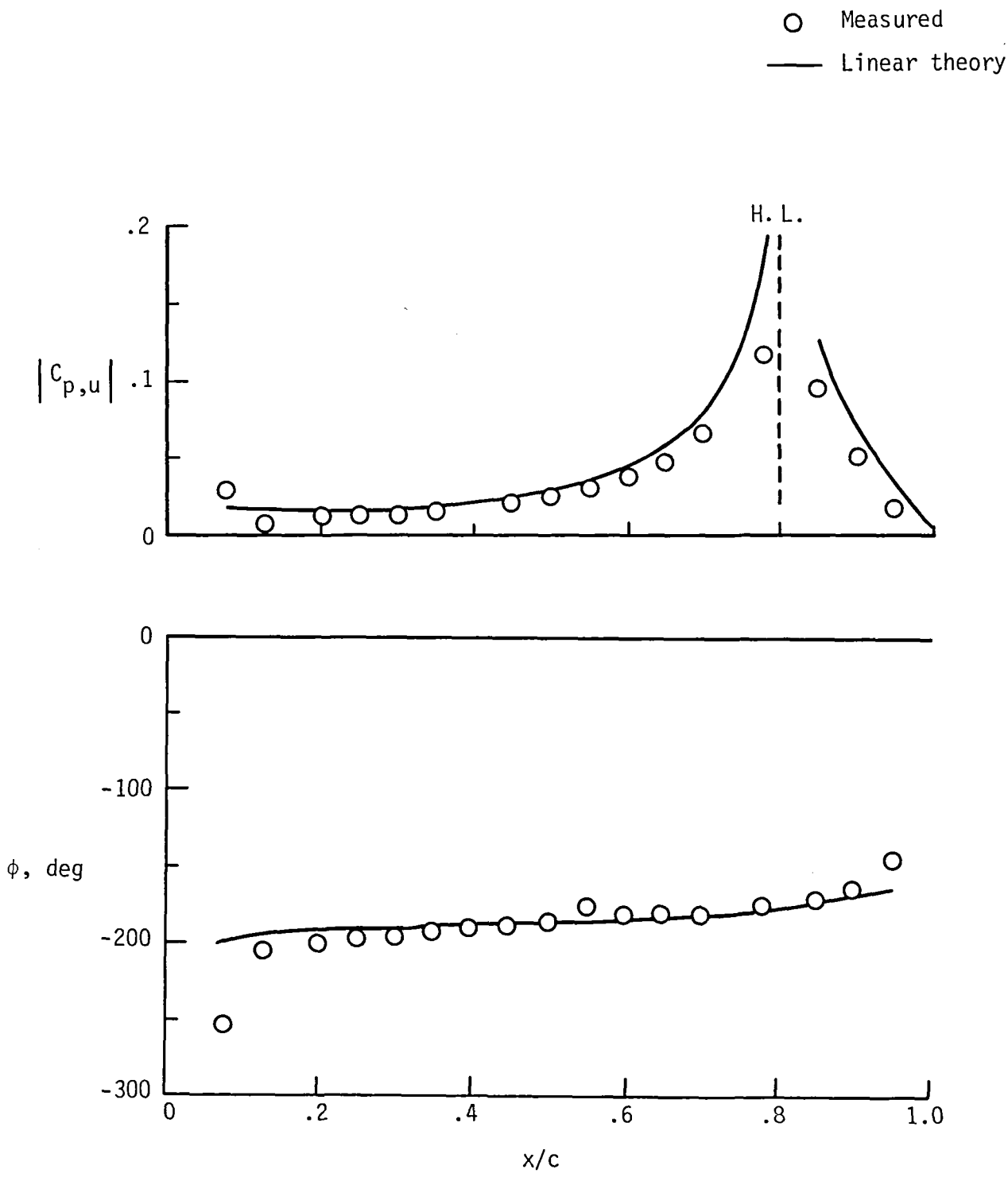

(a) $f = 8$ Hz; $\delta = 5.86°$.

Figure 34. Comparison of unsteady experimental pressures and phase angle on chord D with linear theory for control-surface oscillation at $M = 0.40$ and $\bar{\alpha} = 0.05°$.

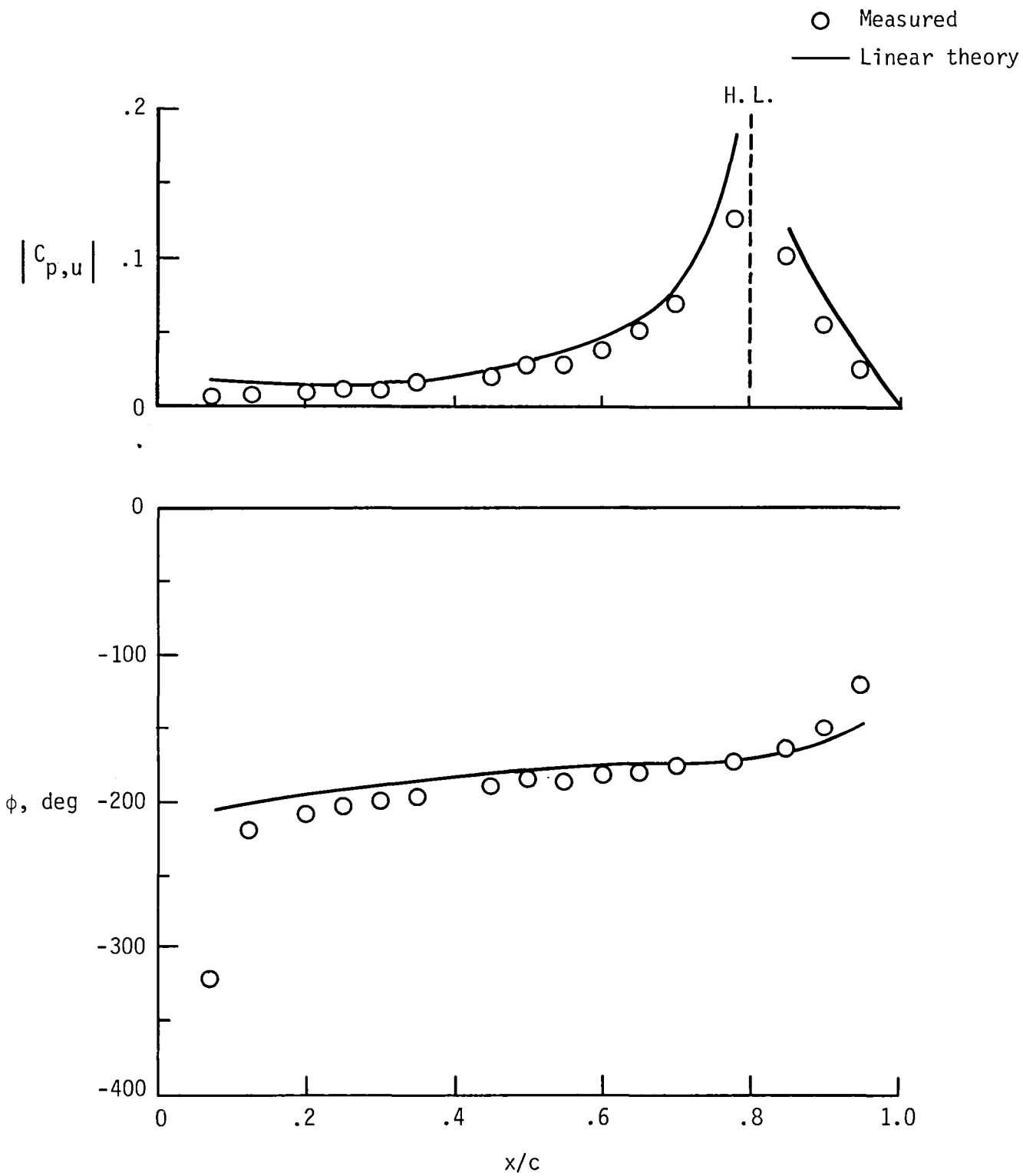

(b) $f = 16$ Hz; $\delta = 5.77°$.

Figure 34. Concluded.

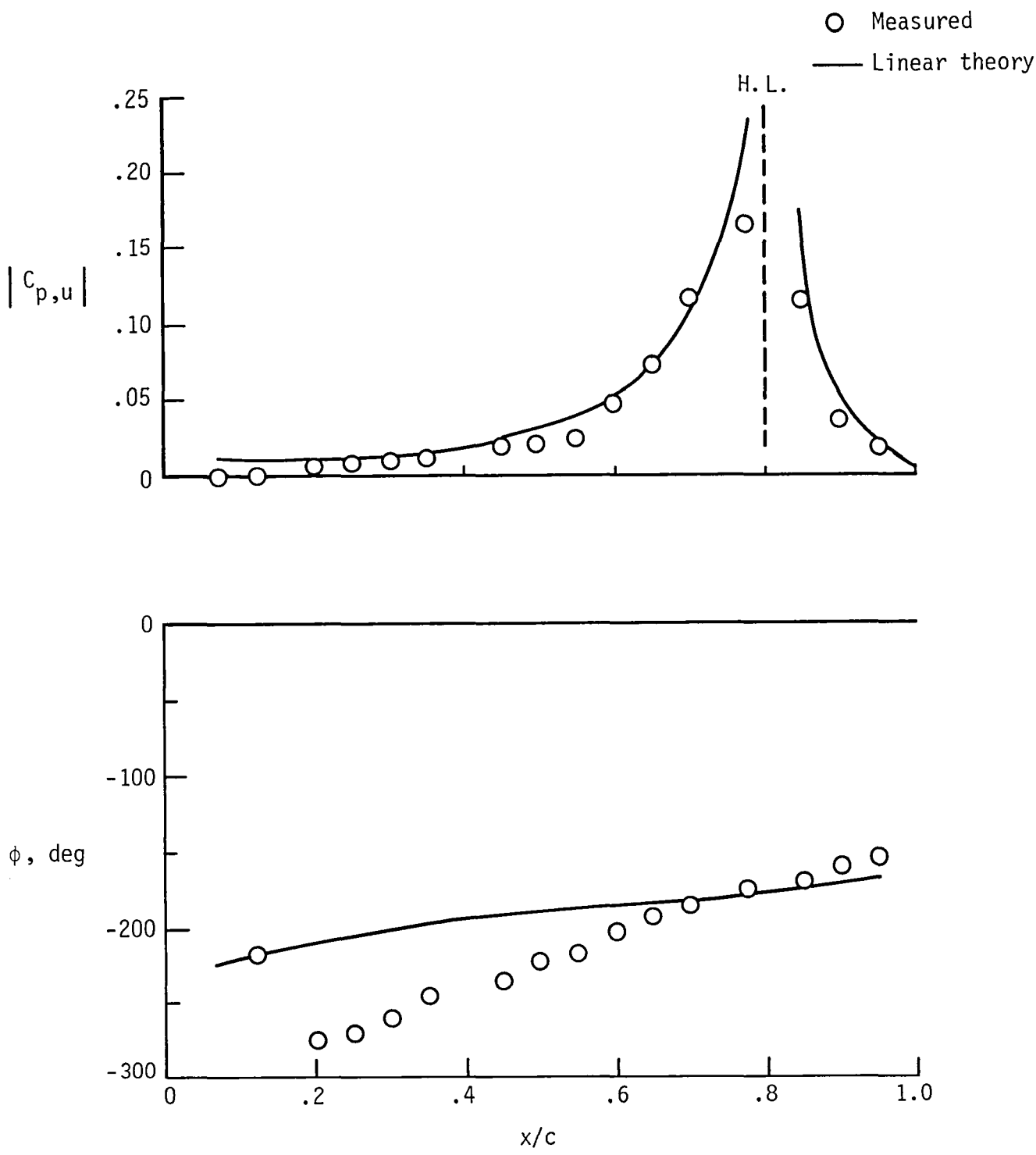

Figure 35. Comparison of unsteady experimental pressure and phase angle on chord D with linear theory for control-surface oscillation at $M = 0.879$, $\bar{\alpha} = 0.05°$, $\delta = 5.89°$, and $f = 8$ Hz.

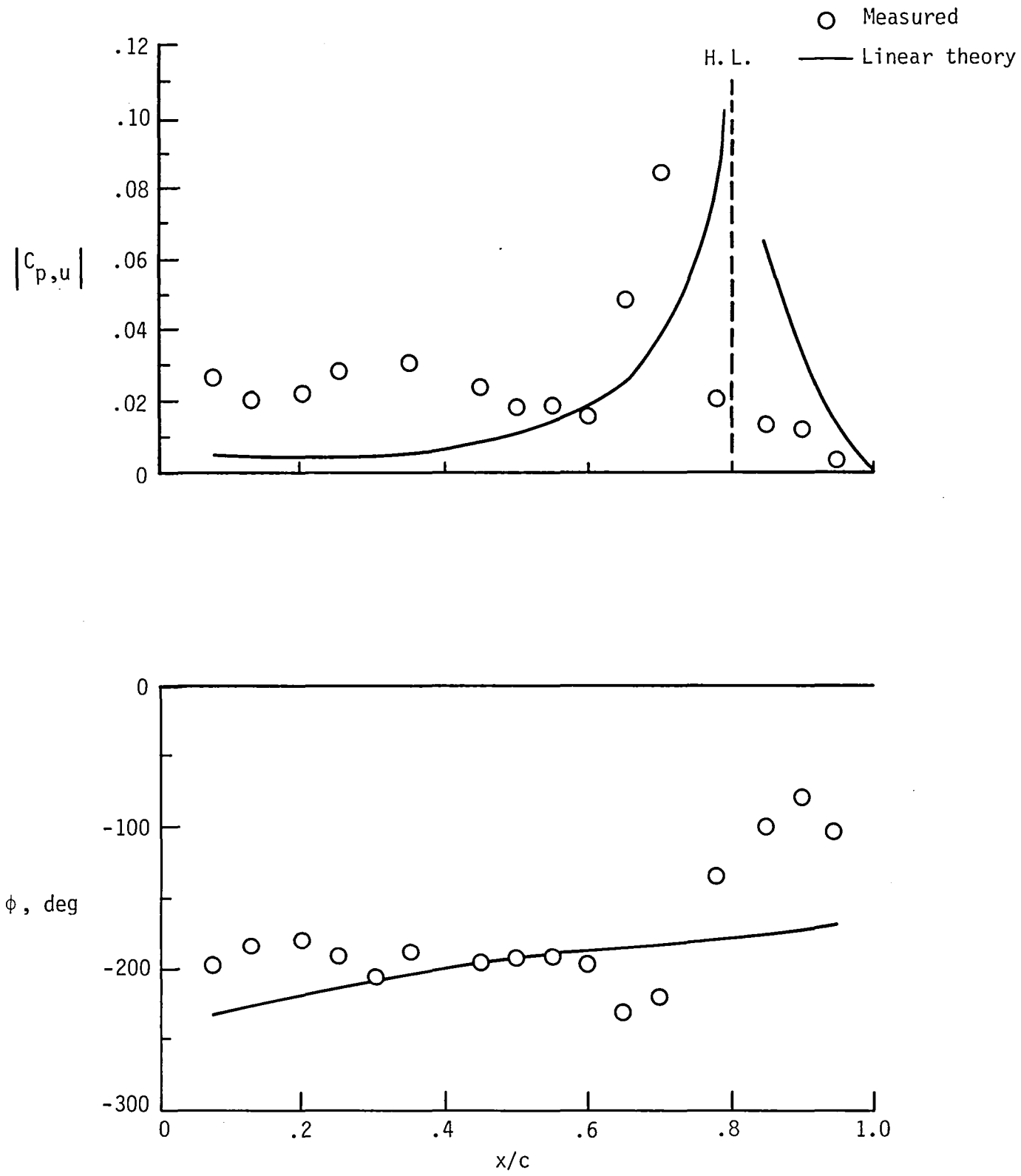

(a) $\delta = 1.98°$.

Figure 36. Comparison of unsteady experimental pressure and phase angle on chord D with linear theory for control-surface oscillation at $M = 0.899$, $\bar{\alpha} = 0.05°$, and $f = 8$ Hz.

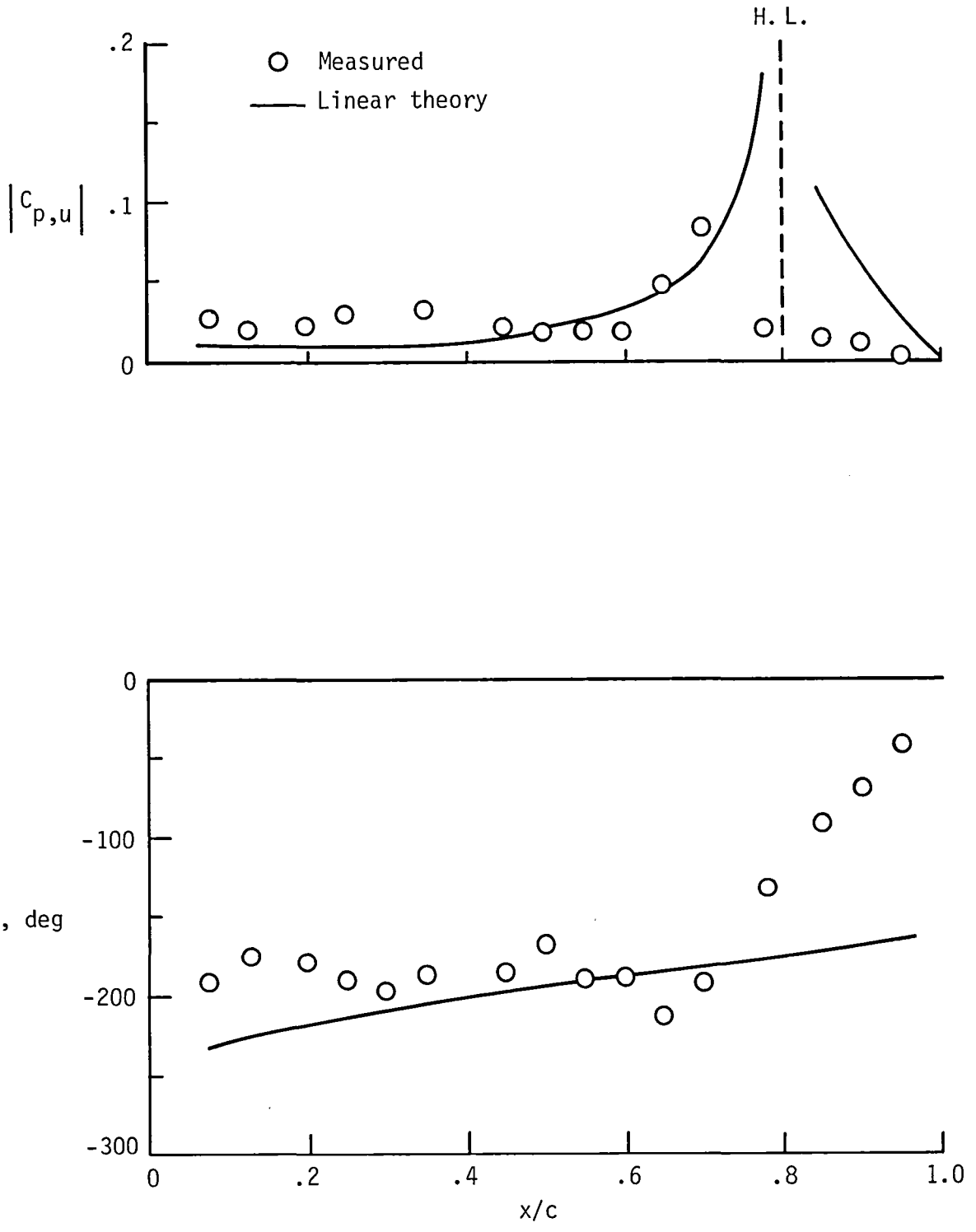

(b) $\delta = 3.48°$.

Figure 36. Continued.

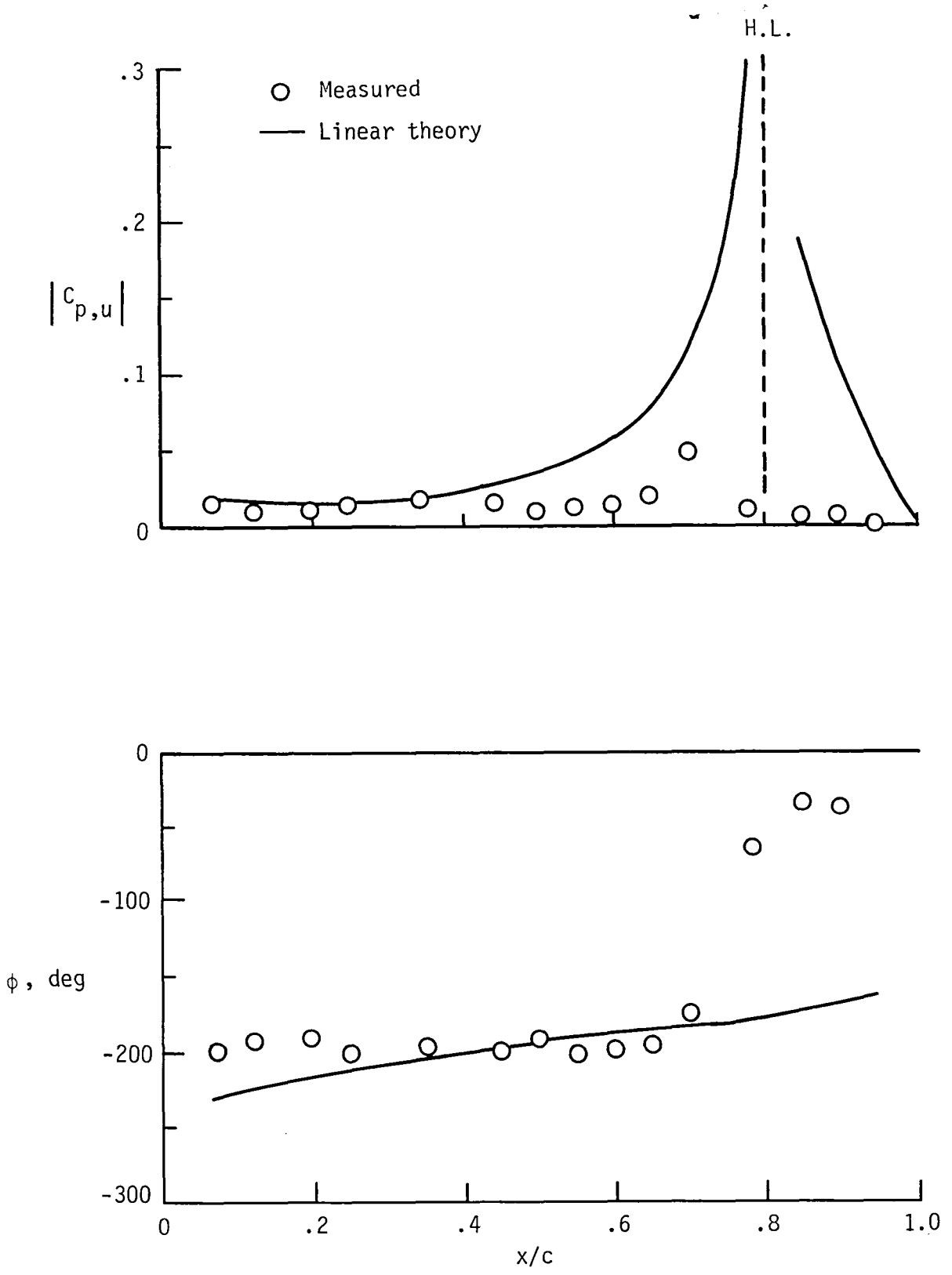

(c) $\delta = 5.90°$.

Figure 36. Concluded.

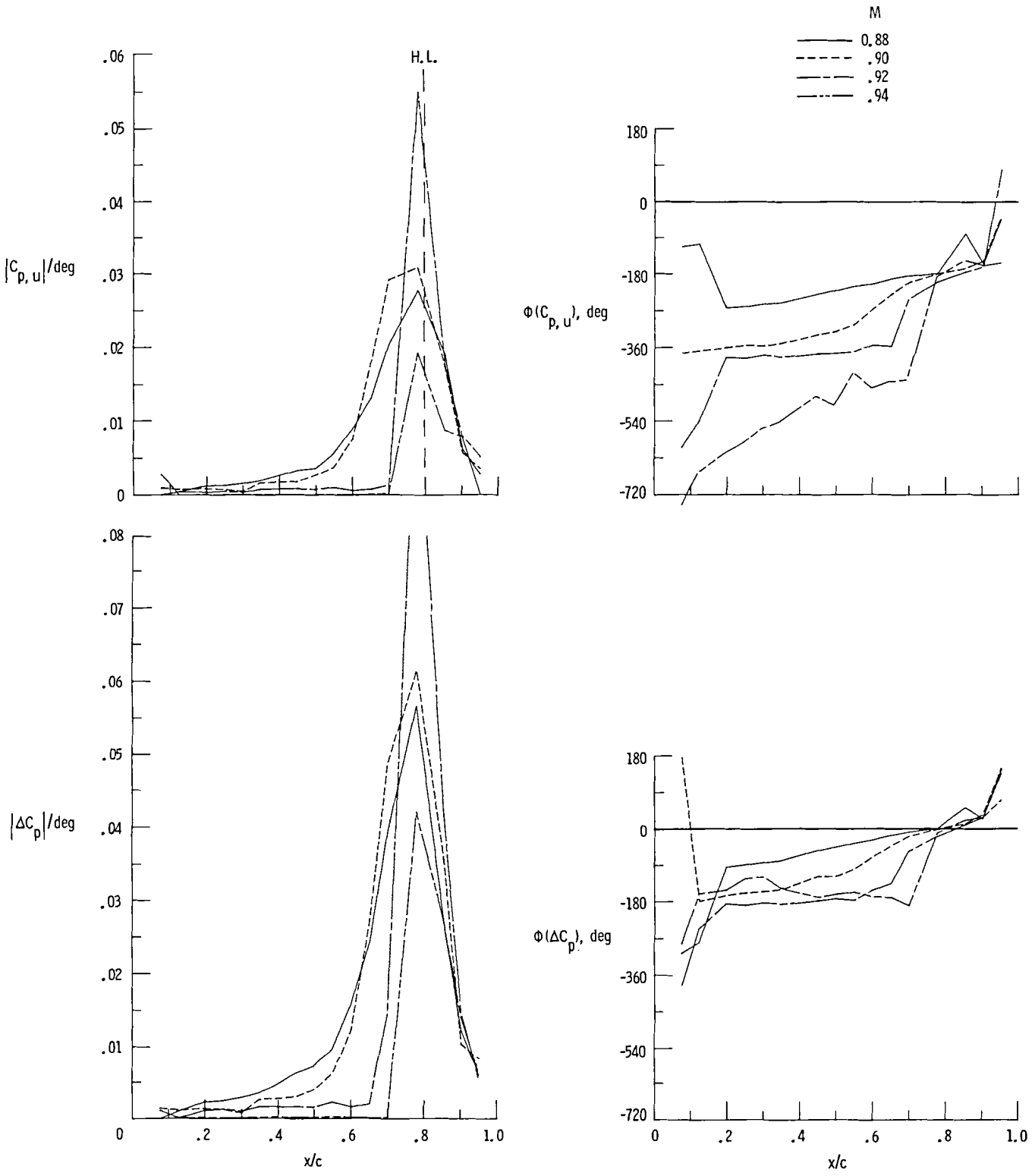

(a) $f = 8$ Hz.

Figure 37. Unsteady pressure distributions and phase angle on chord D at $\bar{\alpha} = 1°$ and $\delta = 6°$ for variable Mach number.

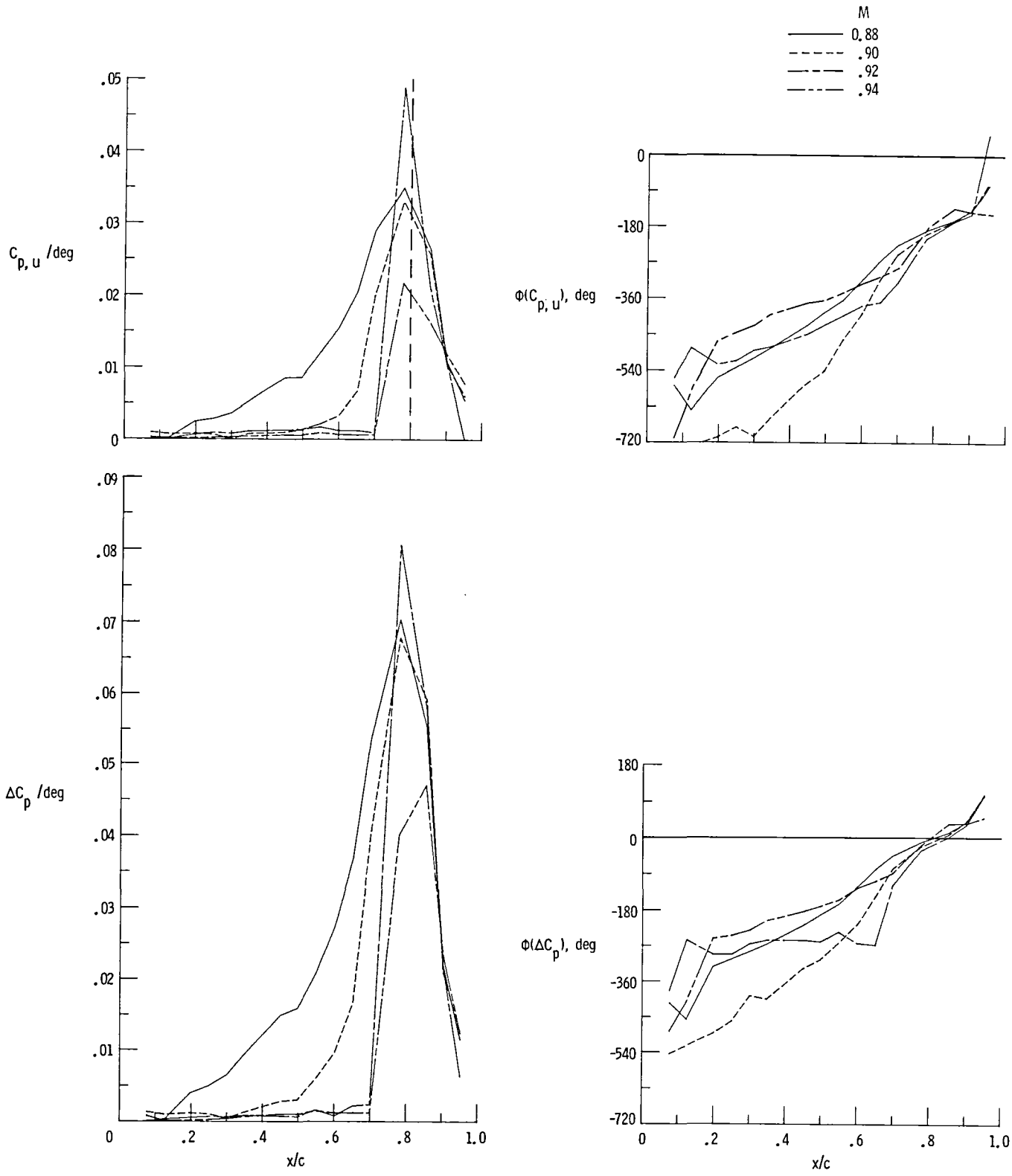

(b) $f = 22$ Hz.

Figure 37. Concluded.

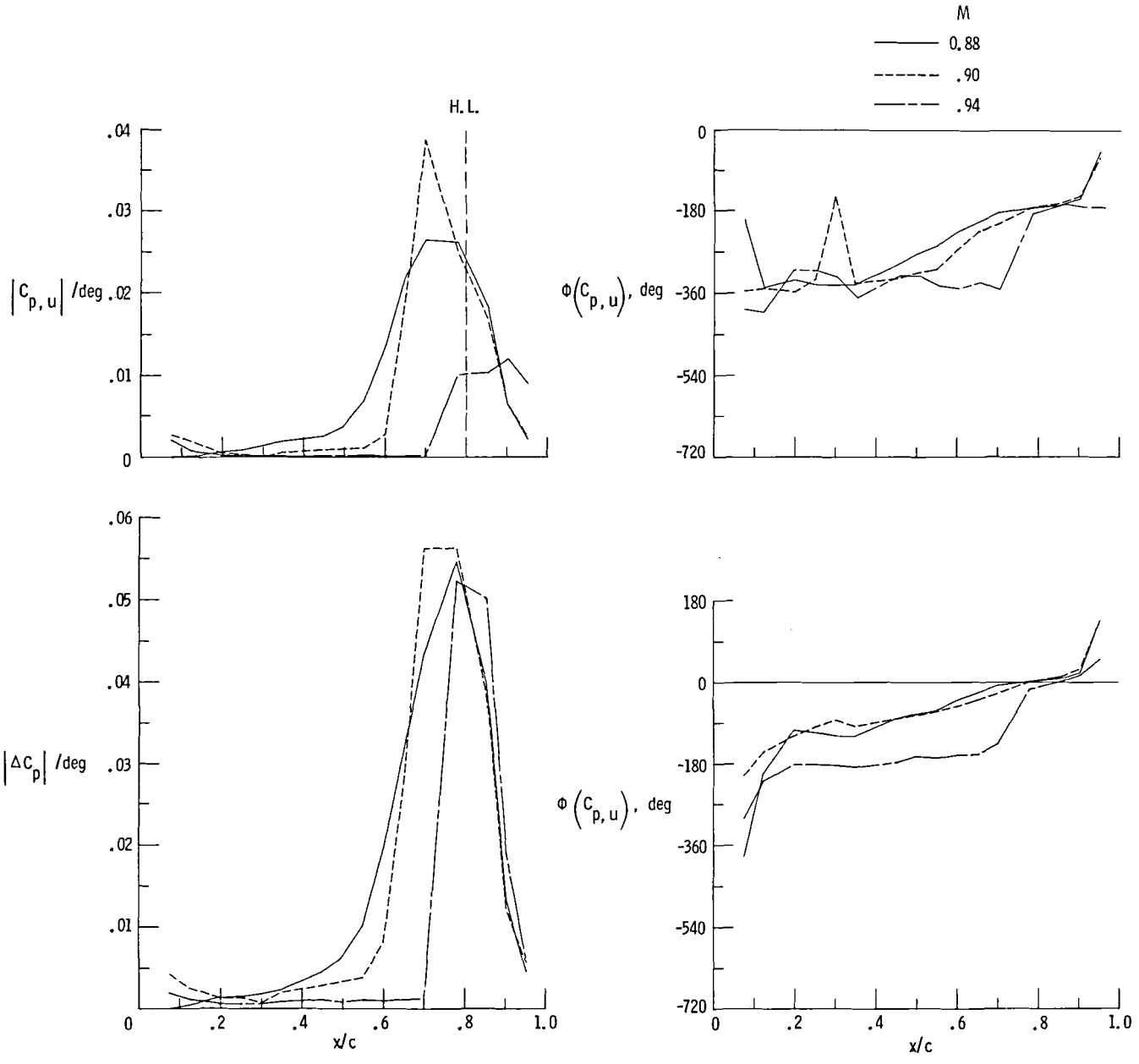

Figure 38. Unsteady pressure distributions and phase angle on chord D at $\bar{\alpha} = 3°$, $\delta = 6°$, and $f = 8$ Hz.

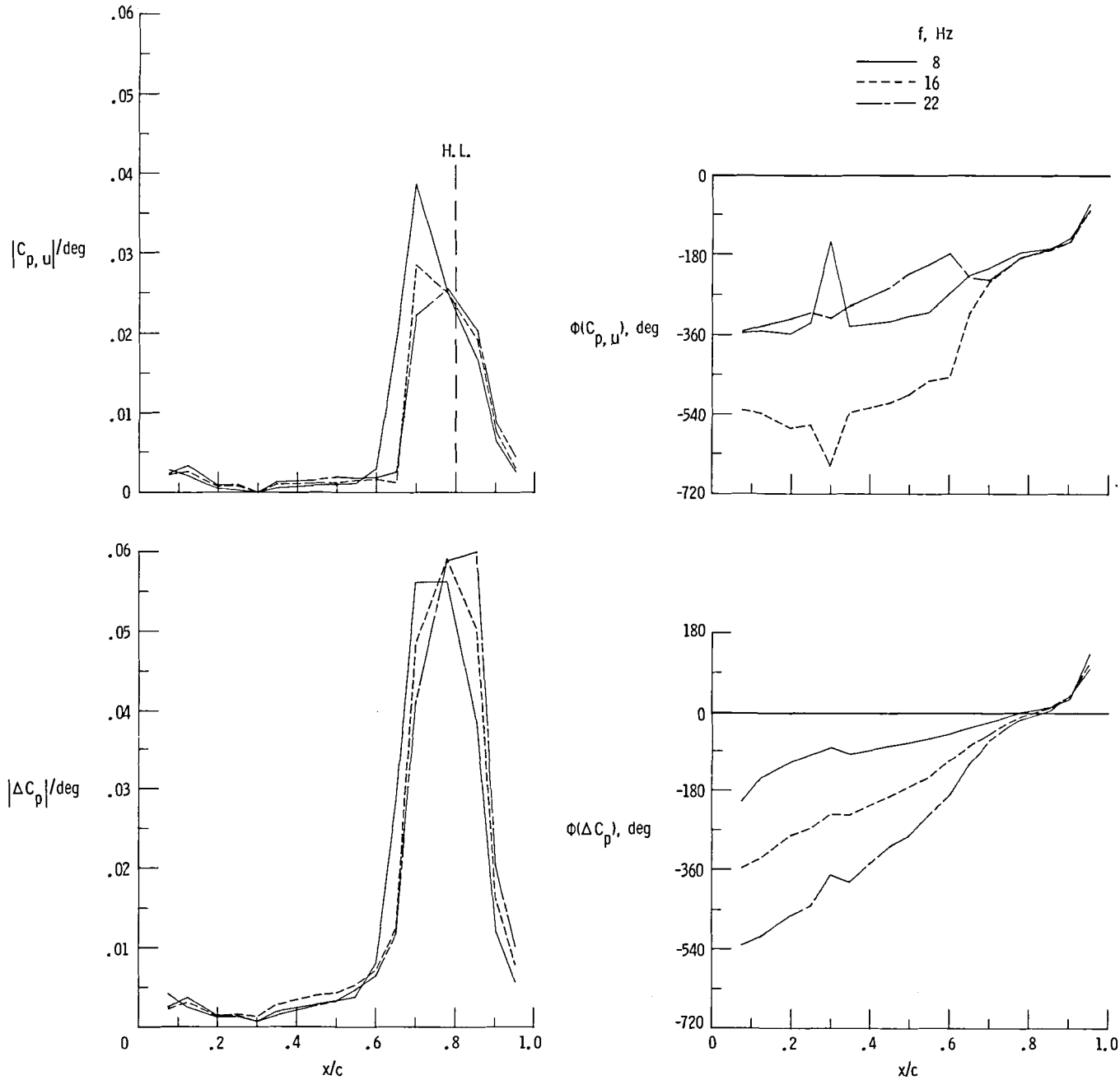

(a) $M = 0.90$.

Figure 39. Unsteady pressure distributions and phase angle on chord D for control-surface oscillation at $\bar{\alpha} = 3°$ and $\delta = 6°$ for variable frequency.

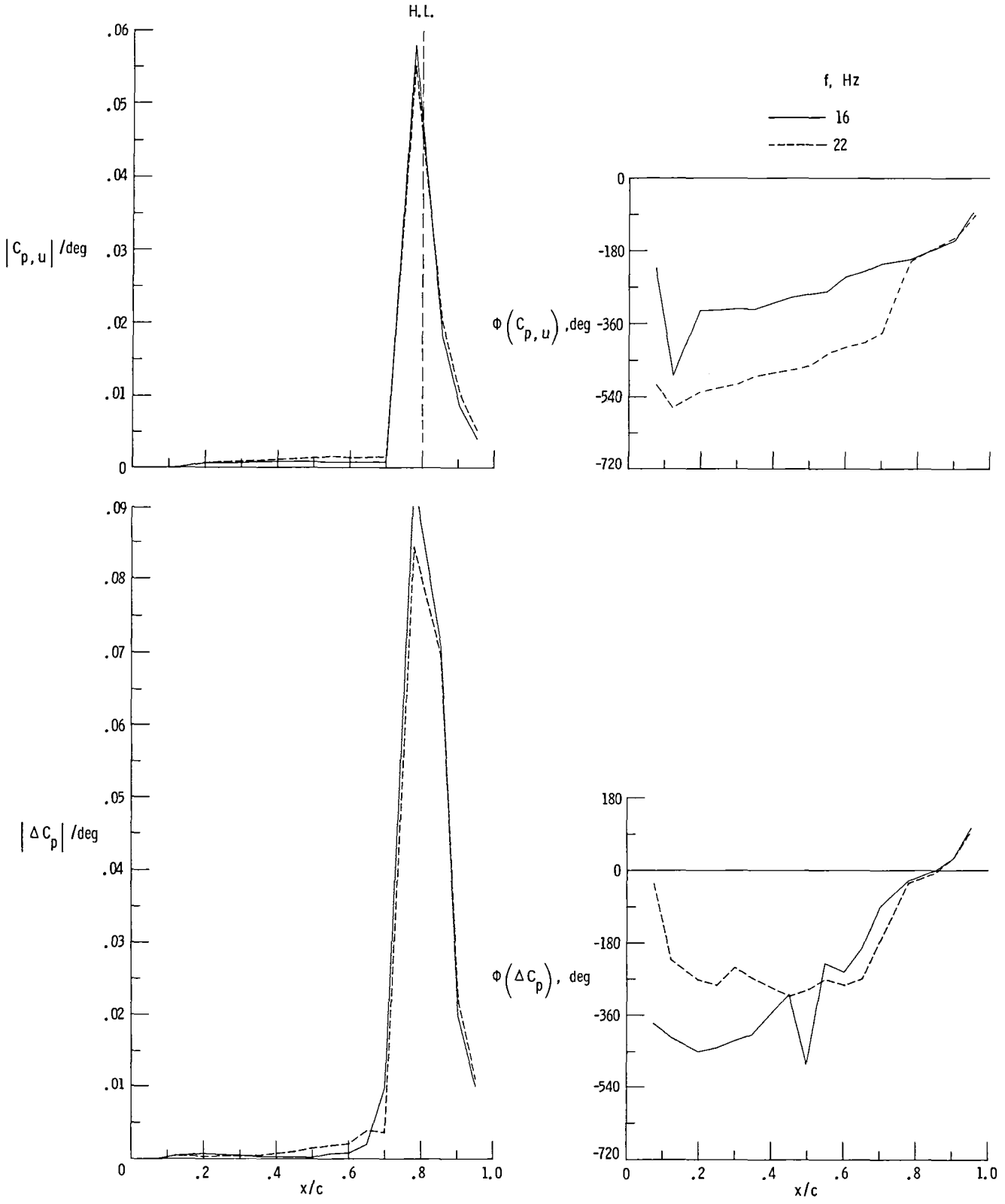

(b) $M = 0.92$.

Figure 39. Continued.

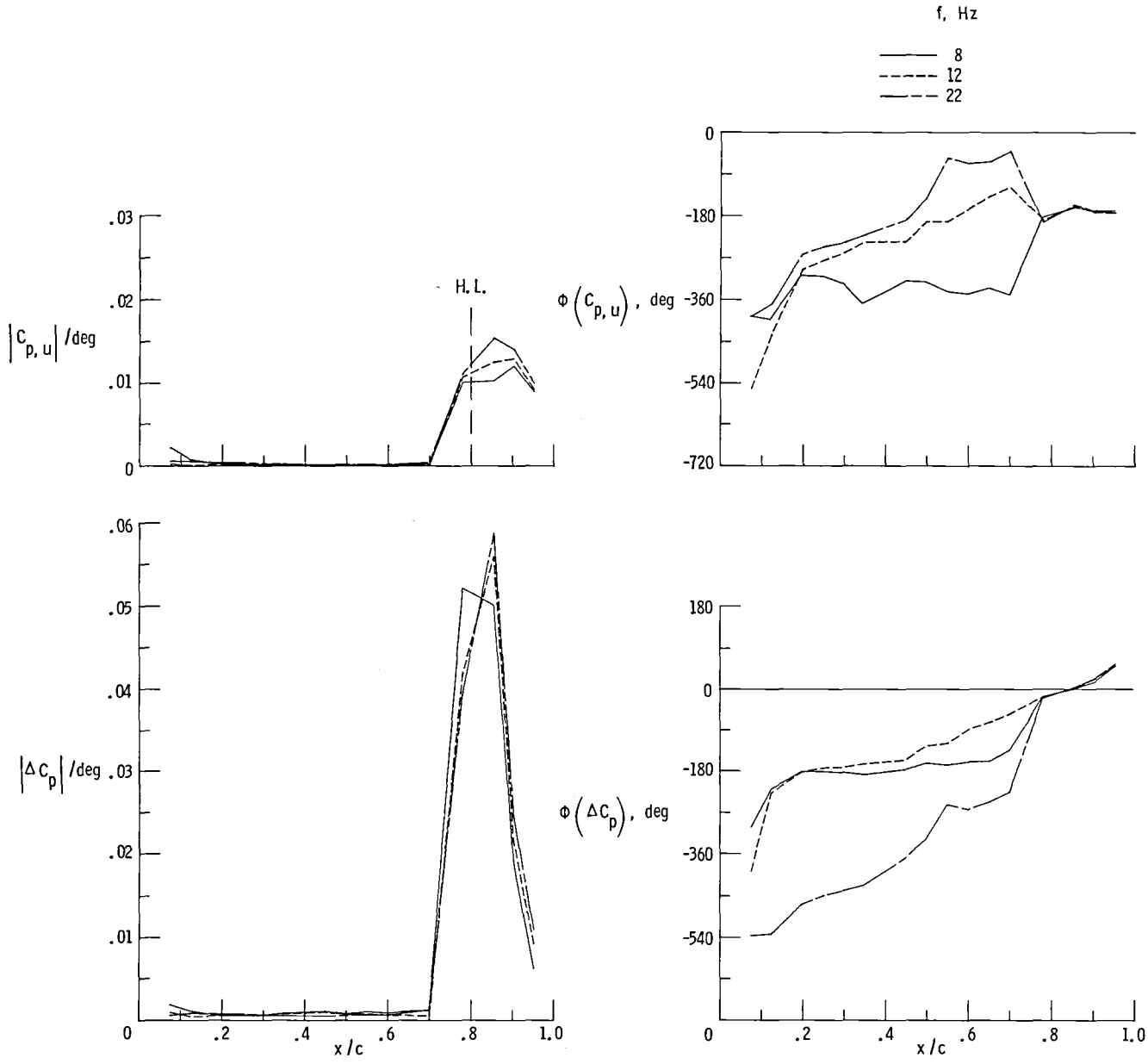

(c) $M = 0.94$.

Figure 39. Concluded.

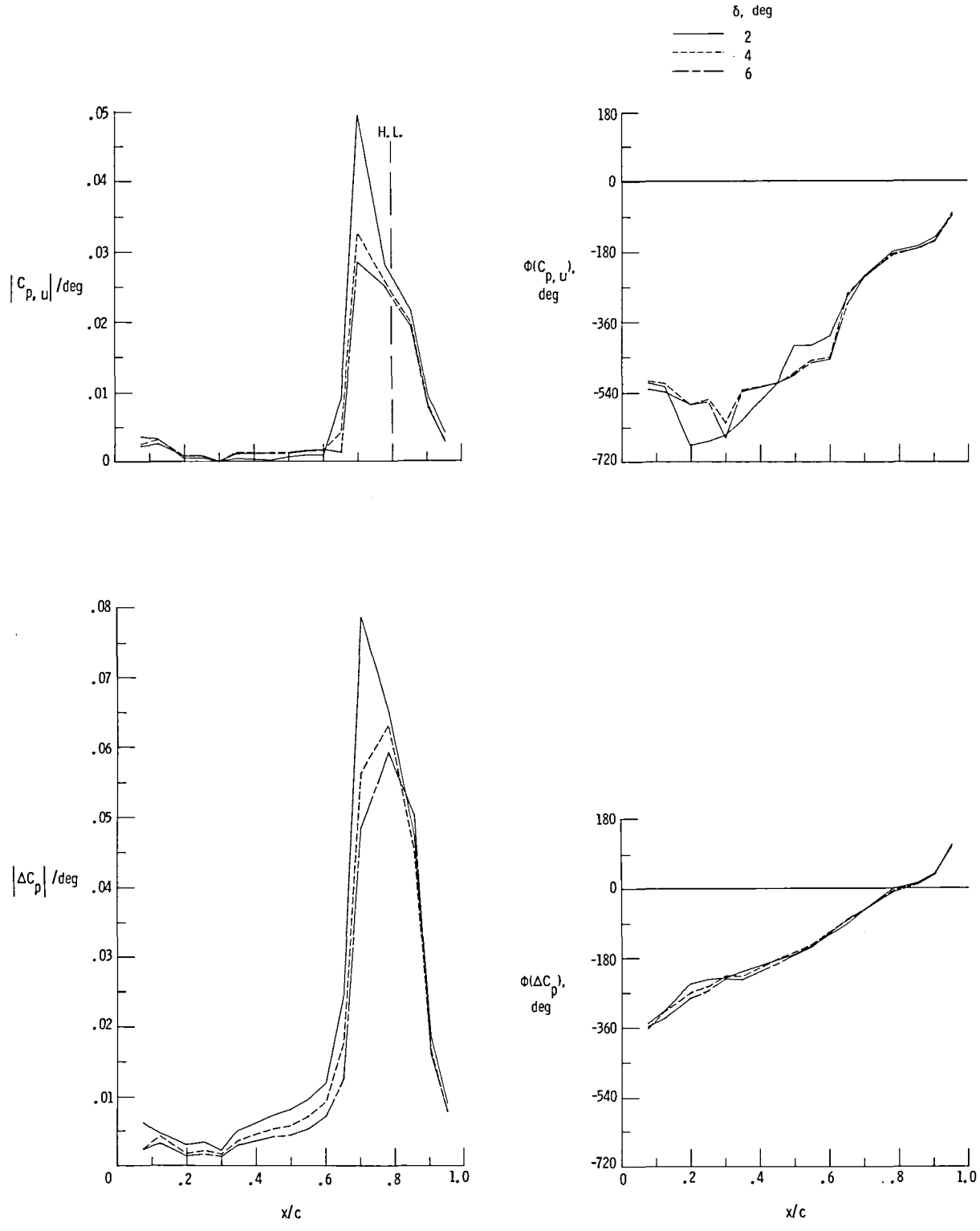

(a) $M = 0.90$.

Figure 40. Unsteady pressure distributions and phase angle on chord D at $\bar{\alpha} = 3°$ and $f = 16$ Hz for control-surface oscillation at $\delta = 2°$, 4°, and 6°.

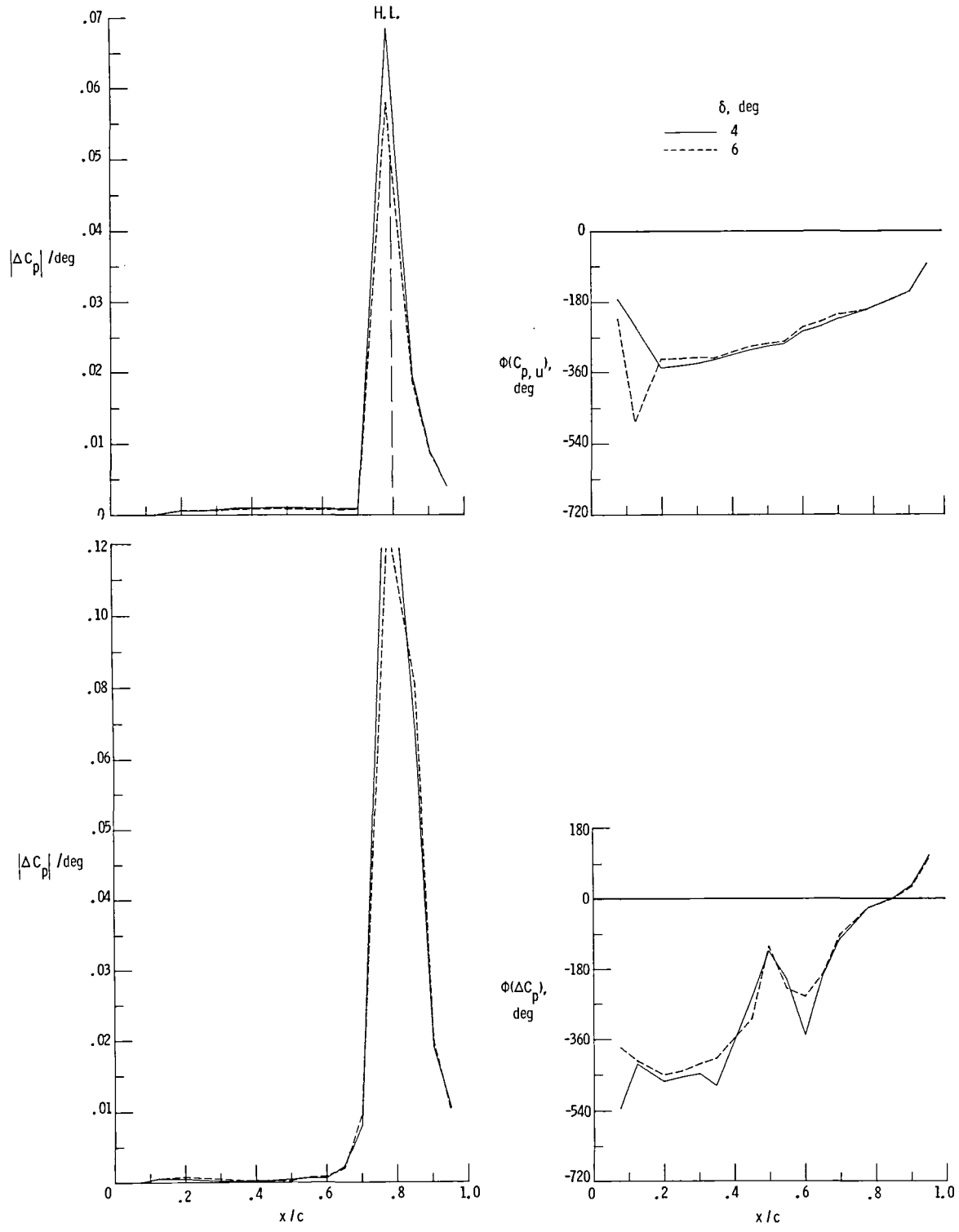

(b) $M = 0.92$.

Figure 40. Continued.

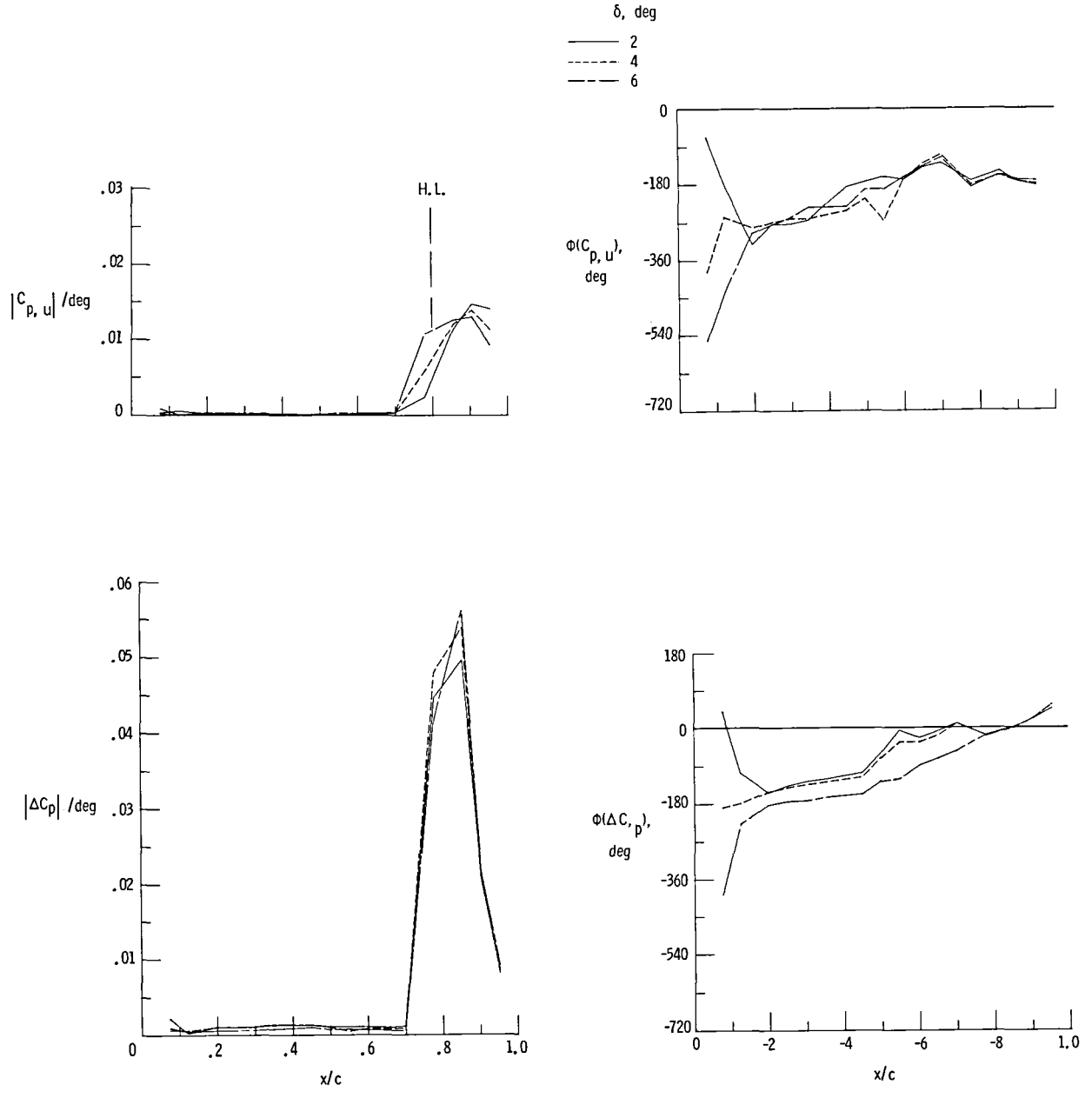

(c) $M = 0.94$.

Figure 40. Concluded.

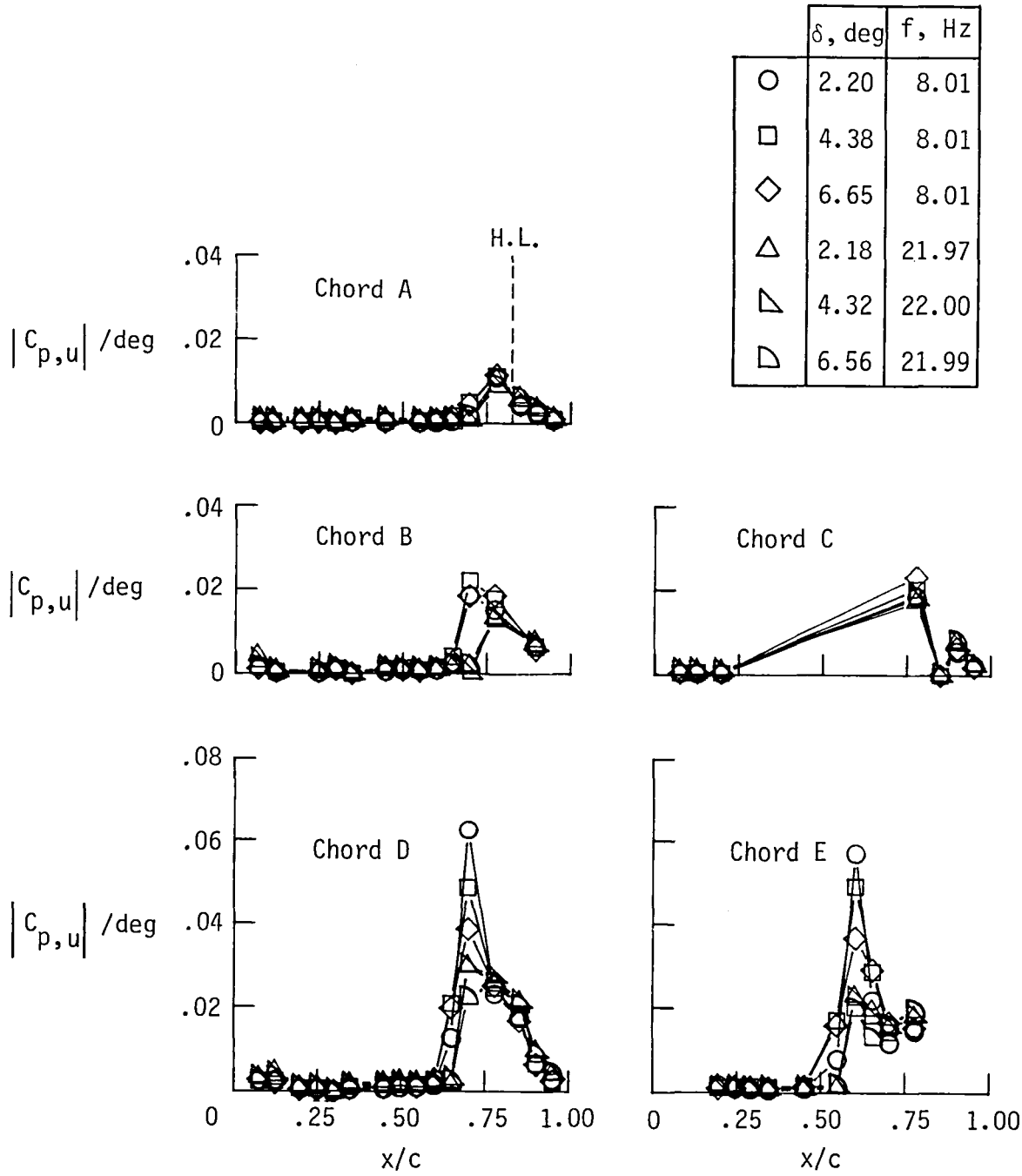

(a) $|C_{p,u}|$/deg.

Figure 41. Unsteady pressure distributions and phase angle on five chords at $\bar{\alpha} = 3°$ for variable frequency and amplitude at $M = 0.90$.

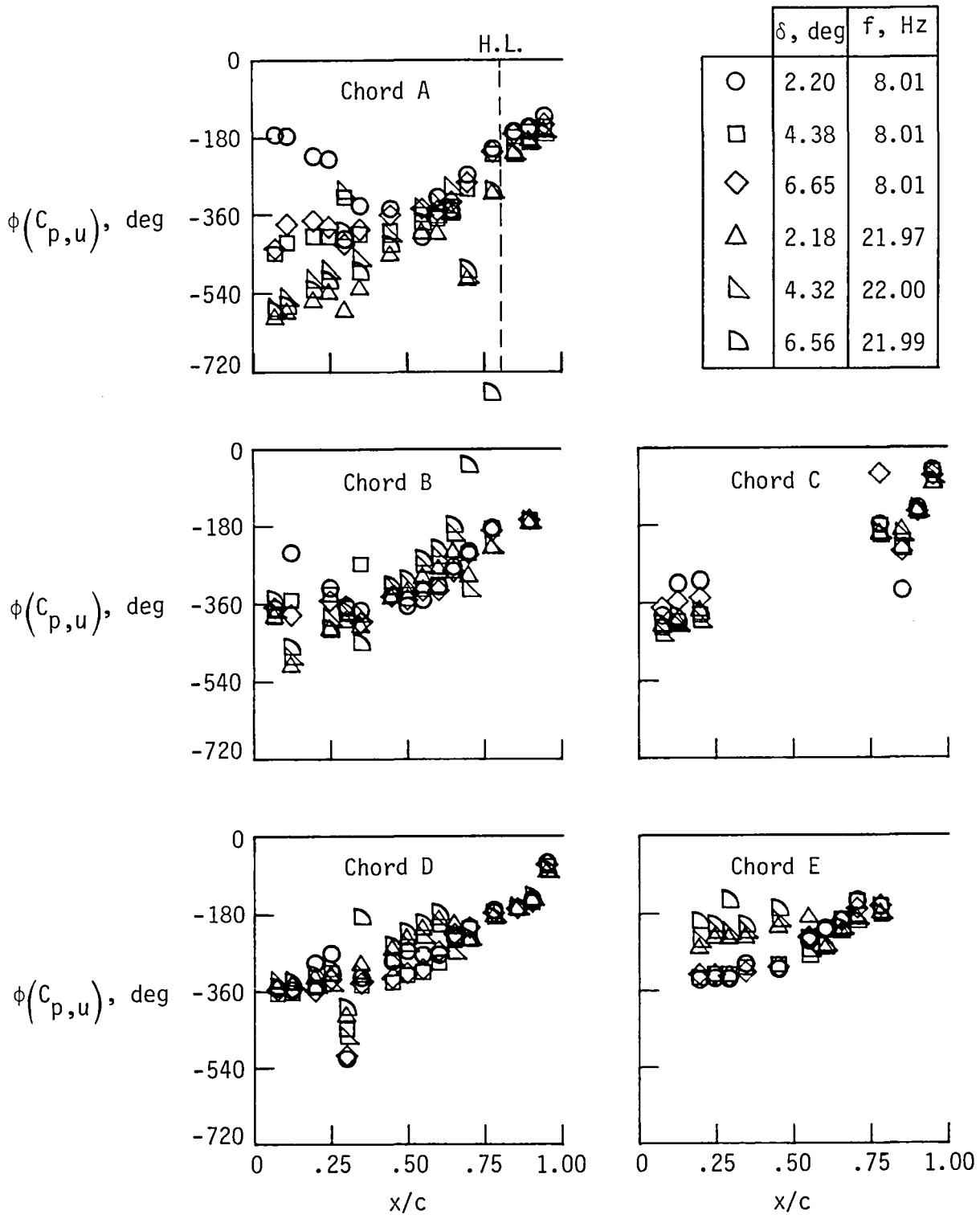

(b) $\phi(C_{p,u})$.

Figure 41. Continued.

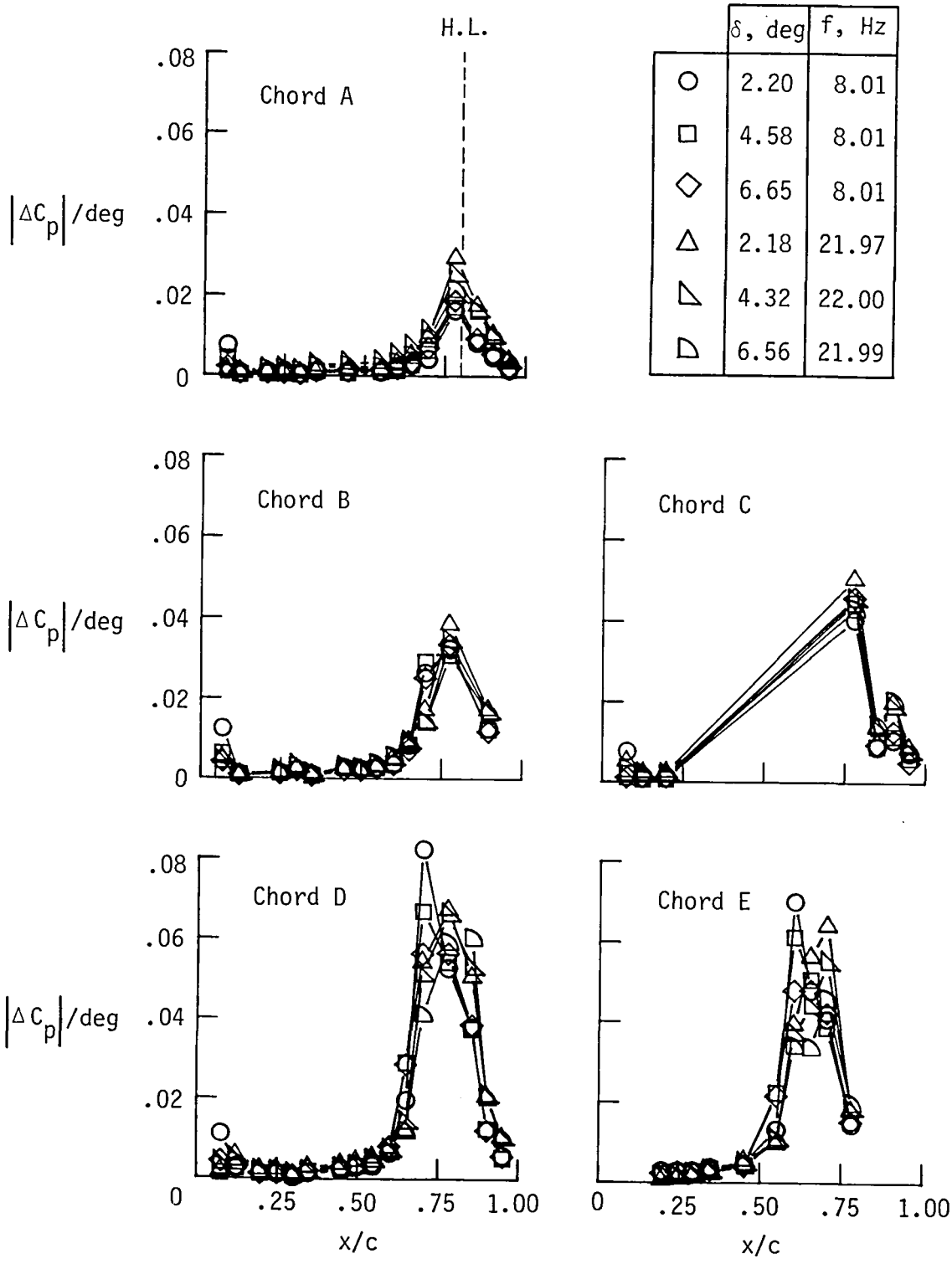

(c) $|\Delta C_p|$/deg.

Figure 41. Continued.

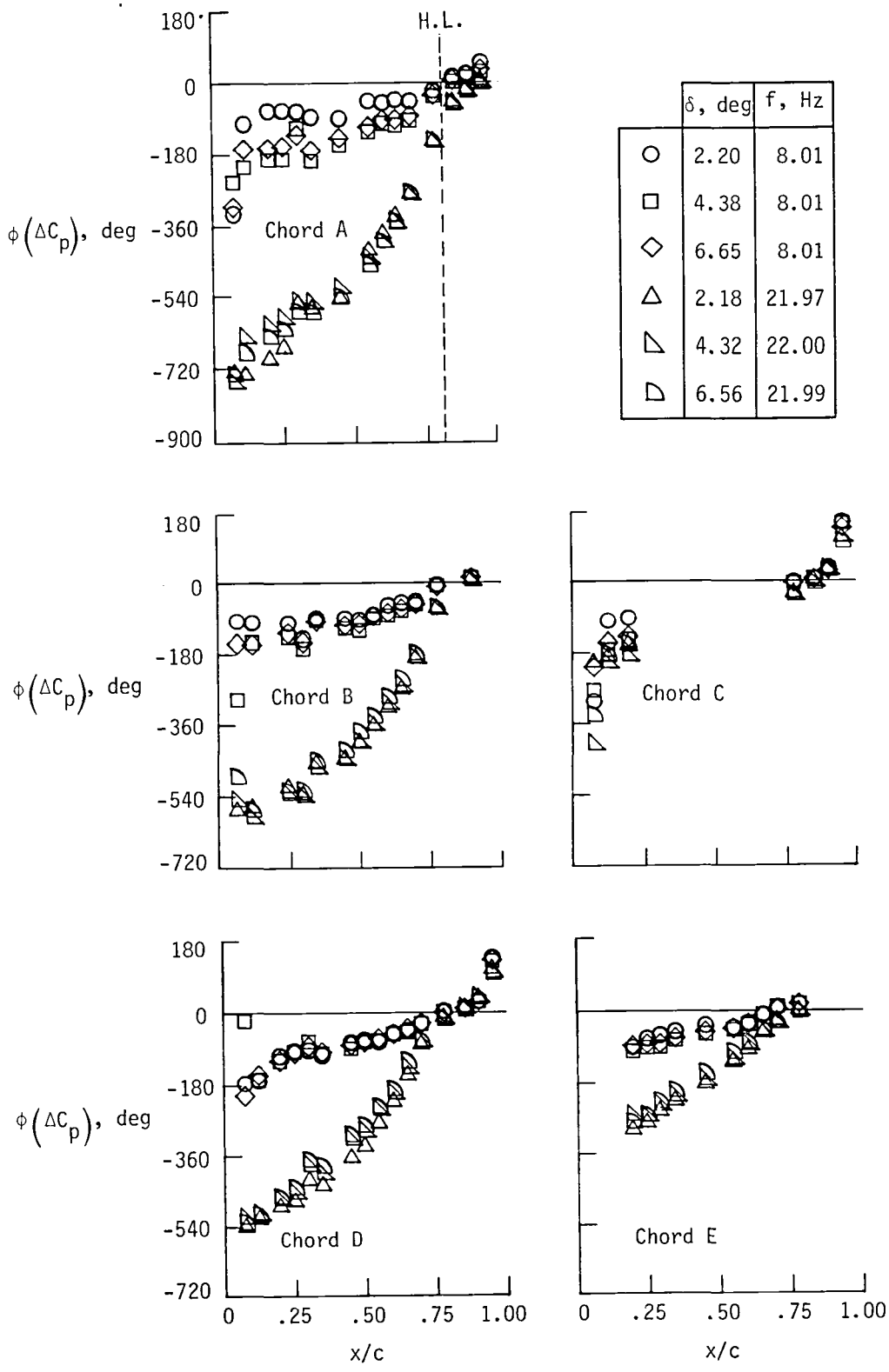

(d) $\phi(\Delta C_p)$.

Figure 41. Concluded.

Standard Bibliographic Page

1. Report No.	2. Government Accession No.	3. Recipient's Catalog No.
NASA TP-2594		

4. Title and Subtitle	5. Report Date
Steady and Unsteady Transonic Pressure Measurements on a Clipped Delta Wing for Pitching and Control-Surface Oscillations	October 1986
	6. Performing Organization Code: 505-33-43-09
7. Author(s): Robert W. Hess, F. W. Cazier, Jr., and Eleanor C. Wynne	8. Performing Organization Report No.: L-16082
9. Performing Organization Name and Address: NASA Langley Research Center, Hampton, VA 23665-5225	10. Work Unit No.
	11. Contract or Grant No.
12. Sponsoring Agency Name and Address: National Aeronautics and Space Administration, Washington, DC 20546-0001	13. Type of Report and Period Covered: Technical Paper
	14. Sponsoring Agency Code

15. Supplementary Notes

Appendix by E. Carson Yates, Jr., NASA Langley Research Center, Hampton, Virginia.

16. Abstract

Steady and unsteady pressures were measured on a clipped delta wing with a 6-percent circular-arc airfoil section and a leading-edge sweep angle of 50.40°. The model was oscillated in pitch and had an oscillating trailing-edge control surface. Measurements were concentrated over a Mach number range from 0.88 to 0.94; less extensive measurements were made at Mach numbers of 0.40, 0.96, and 1.12. The Reynolds number based on mean chord was approximately 10×10^6. The interaction of wing or control-surface deflection with the formation of shock waves and with a leading-edge vortex generated complex pressure distributions that were sensitive to frequency and to small changes in Mach number at transonic speeds.

17. Key Words (Suggested by Authors(s))	18. Distribution Statement
Unsteady pressures Steady pressures Transonic Clipped delta wing	~~LIMITED DISTRIBUTION~~ Until October 1988 Subject Category 02

19. Security Classif.(of this report)	20. Security Classif.(of this page)	21. No. of Pages	22. Price
Unclassified	Unclassified	116	

For sale by the National Technical Information Service, Springfield, Virginia 22161

NASA-Langley, 1986